Proceedings of the First OCCAM-Fields-MITACS Biomedical Problem Solving Workshop

The Fields Institute for Research in Mathematical Science

Toronto, Ontario

June 22–26, 2009

Editor:

Gregory M. Lewis
(University of Ontario Institute of Technology)

Contents

Preface by the Director of the Centre of Mathematical Medicine, Fields Institute

The resounding success of the first Fields-MITACS Industrial Problems Workshop in 2006 (FMIPW), paved the way for the OCCAM-Fields-MITACS Biomedical Problem Solving Workshop that took place June 22-26, 2009. This was the first Mathematics-in-Medicine Study Group (MMSG) meeting to be held on Canadian soil, and it's unmitigated success ensures that it will, no doubt, become a regular feature at Fields and in Canada, in future years.

MMSGs are workshops intended to foster interaction between mathematicians and biomedical researchers. These were pioneered in the UK, with a now over 10 year distinguished history. Biomedical researchers/scientists/clinicians from experimental laboratories/hospitals/universities/companies are invited to present problems of current interest; these problems may come from a very wide range of subject areas, the only prerequisite is that these problems should be amenable to mathematical modelling and anlaysis (in a broad sense). MMSGs have served to establish strong links between clinicians, experimentalists and mathematicians, and to engage a new generation of mathematicians and experimentalists in this exciting interdisciplinary field. The stated objectives of the workshop (in the tradition of Industrial Study Groups) were fourfold : (1) to introduce mathematicians/modellers to the rich source of problems arising in one of the "last frontiers" for mathematics, the biomedical sciences, (2) to effectively aid clinicians and biomedical researchers to exploit and incorporate current mathematical/computational tools, (3) to engage and train a new generation of mathematicians in the interdisciplinary field of mathematical medicine/biology, and finally (4) to provide a natural opportunity and ambience, conducive to fostering and encouraging long term interdisciplinary collaborations.

Quite clearly, the meeting succeeded admirably on all counts. For those who have never had the good fortune or opportunity to participate in a Study Group meeting of this nature, this Proceedings volume will give a polished but sanitized account of what actually transpired over the course of five exhilarating days in June 2009. Although the core of the ideas and models presented in this volume, were culled during these five intense days of discussions and dialogue, nothing can capture the energy and enthusiasm that engulfed the Medical Sciences Building at the University of Toronto, during this short but invigorating period of time. Roughly half of the seventy five attendees were experienced Study Group participants, of which a significant number were seasoned veterans from the UK. Incredibly, although no-one is constrained to work on any particular problem, in "steady state" each of the problems had roughly a sixth of the total number of participants, all enthusiastically working towards a clearer formulation or resolution of their particular problem. In retrospect, much of the smooth functioning of the workshop, should probably be attributed to the deftness and experience with which Huaxiong Huang, Sean Bohun, Nilima Nigam and Chris Breward (amongst others), shepherded the appropriate expertise to where it was most required. Lunches and coffee/tea breaks are provided on site, and many groups (engrossed in their problems) worked late into the nights, well past the daily briefings that took place at 5:30pm each day. The six problems presented, spanned a very broad spectrum of questions

of biomedical interest : The first problem on "Constitutive Models for Tumour Classification" presented by Corina Drapaca (Penn State) posed the question of how to distinguish between normal and abnormal tissue (in particular, how to differentiate between benign and malignant tumours) by developing an appropriate constitutive theory. The second problem, presented by Miles Johnston (Sunnybrook & Womens Hospital Research Institute) focussed on possible molecular mechanisms underlying the pathogenesis of hydrocephalus and the possibility of incorporating these in a mathematical model to predict ventricular distension resulting from hydrocephalus. Problem three, presented by Svetlana Komarova (McGill) posed the question of the identification of mediators of mechanotransduction between bone cells. Bone mass and architecture are apparently regulated by mechanical forces leading to increase in bone mass in response to excessive loading, or decrease in bone mass in the absence of physical activity (or loading). The objective here was to develop a theoretical framework which could explain the means by which mechanical stimulation is communicated among bone cells. The fourth problem, presented by D. Bassett and J. Barralet (Strathcona Anatomy & Dentistry, McGill) was concerned with the formation of calcium carbonate crystals in a gas diffusion process, where various characteristics of the crystals suggest an underlying process regulating crystallization. Problem five was presented by Sushrat Waikar (Brigham & Women's Hospital, Boston) and addressed a question associated with haemodialysis. Although the process is well understood, what was unclear was the overall effect on net blood sodium concentration levels post treatment. The focus for this problem was on the development of a fundamental model to address this issue. The sixth and final problem, presented by Mustafa Al-Zoughool (Ottawa) and Susie El Saadany (Public Health Agency, Canada) addressed a particular public health concern. Variant Creutzfeldt Jakob Disease (vCJD) or "mad cow" disease is characterized by long incubation periods, spongiform changes and astrogliosis. The focus here was on the development of appropriate mathematical models for estimating the risk of vCJD transmission.

This volume is a detailed record of the progress made on these problems during the five critical days of the meeting, followed up and embellished over subsequent months by various group members. However, it cannot unfortunately capture the frenetic, energised and enthusiastic spirit that pervaded the meeting. Participants grabbed quick meals and worked late into the nights (fuelled by coffee and tea) to present and demonstrate the significant progress that had been made over the week, almost uniformly on all six problems. In wandering through the various groups and group discussions, I was struck by the probing, fearless questions and different perspectives brought to bear on each of the problems - it certainly brought home the old Chinese adage "He who asks a question may be a fool for a minute, he who does not, remains a fool forever"! This volume is by no means the final story - it represents the first steps taken in addressing questions that are of significant public and/or research interest, but to borrow Lao Tzu's words "A journey of a thousand miles begins with a single step". The meeting and the collaborations established, will hopefully develop into a longer and even more productive journey. What seems transparently clear from the meeting, is that this type of endeavour is not a straightforward path with the journey clearly mapped out. It combines both scientific method as well as more creative and artistic traits, and a successful exponent or practitioner must also use analogy in addressing such a variety of often seemingly disparate problems. How does one effectively train a

new generation of researchers to embrace and flourish in this type of "problem solving" interdisciplinary research environment - this is probably the million dollar question! - a first step is certainly to participate in one of these Math-in-Medicine Study Groups. As many seem to have discovered to their ultimate benefit, once bitten there is no escape!

Siv Sivaloganathan

Director, Centre of Mathematical Medicine, Fields Institute

Acknowledgements

It is due to the hard work of many people that the First OCCAM-Fields-MITACS Biomedical Problem Solving Workshop was a success. An important part of a workshop such as this is the writing of the reports. It is here that the tangible evidence of the productivity of the week can be seen. These reports represent a great effort. Therefore, we would like to thank those individuals who took the responsibility to ensure that the ideas generated at the workshop would be available for all in the form of these Proceedings, and in particular for doing so very quickly and effectively.

It is also a tremendous amount of work to collect the problems and organize the workshop itself. We would like to thank the organizers

- C. Breward (Oxford),
- C.S. Bohun (UOIT),
- H. Huang (York),
- N. Nigam (Simon Fraser),
- D. Schwendeman (RPI),
- S. Sivaloganathan (Waterloo),
- B.S. Tilley (Olin College of Engineering),
- J.F. Williams (Simon Fraser)

for putting together this successful event.

The organizational details would not have been possible without the help of the Fields Institute staff. In particular, the organizers would like to thank Alison Conway, Natalie Dytyniak, Judith Munn, Philip Spencer and Luke Chang.

Of course, without the problems the workshop could not have taken place. We would like to thank the problem presenters for contributing such interesting problems:

- Dr. Corina Drapaca (Penn State),
- Dr. Miles Johnston (Sunnybrook Health Sciences Centre),
- Svetlana V. Komarova (McGill),
- David C. Bassett and Jake E. Barralet (Faculty of Dentistry, McGill University),
- Sushrut S. Waikar, MD, MPH, (Brigham and Womens Hospital),
- Dr. Mustafa Al-Zoughool and Dr. Tamer Oraby (McLaughlin Center for Population Health Risk Assessment, University of Ottawa), and Dr. Susie El Saadany (Public Healthy Agency of Canada).

Not least of all, the problems could not have been solved without the tremendous effort put forth by the academic participants. We thank them heartily for the generosity of their time and mental capacity.

I would also like to thank the Centro de Modelamiento Matemático (CMM), Universidad de Chile, Santiago, Chile, for their hospitality while compiling these proceedings.

Greg Lewis (UOIT)

Editor

Constitutive Models for Tumour Classification

Problem Presenter: Corina S. Drapaca (Pennsylvania State University)

Contributors: D. Aruliah (UOIT), R.D. Donaldson (Simon Fraser University), C.S. Drapaca (Pennsylvania State University), G. Lewis (UOIT), A. Sanchez (University of Waterloo), V. Takeva-Volkov (UOIT)

Report prepared by: D. Aruliah, R.D. Donaldson, C.S. Drapaca[1] and A. Sanchez

Abstract. The aim of this paper is to formulate new mathematical models that will be able to differentiate not only between normal and abnormal tissues, but, more importantly, between benign and malignant tumours. We present preliminary results of a tri-phasic model and numerical simulations of the effect of cellular adhesion forces on the mechanical properties of biological tissues.

1 Introduction

Diagnostic radiology is an exciting and rapidly expanding multi-disciplinary field of clinical medicine which links medicine to science and engineering. It enables noninvasive imaging and investigation of structure and function of the human body, and a unique insight into disease processes *in vivo*. One such imaging technique, called Magnetic Resonance Elastography (MRE), is used to measure the elasticity of biological tissues subject to mechanical stress [8, 9]. The resulting strains are measured using magnetic resonance imaging and the related elastic modulus is computed from models of tissue mechanics. The elastic modulus contains important information about the pathology of the imaged tissues. Thus, MRE can help in tumour detection, determination of characteristics of disease, and in assessment of rehabilitation.

It was noticed experimentally that most biological tissues have incompressible viscoelastic features: they have a certain amount of rigidity that is characteristic of solid bodies, but, at the same time, they flow and dissipate energy by frictional losses as viscous fluids do [3, 4]. The incompressibility assumption for soft tissues is based on the fact that most tissues are made primarily of water. In addition, since the displacements in MRE are very small (on the order of microns), a linear constitutive law is usually assumed. However, despite the richness of the data set, the variety of processing techniques and the simplifications made

---

[1] csd12@psu.edu
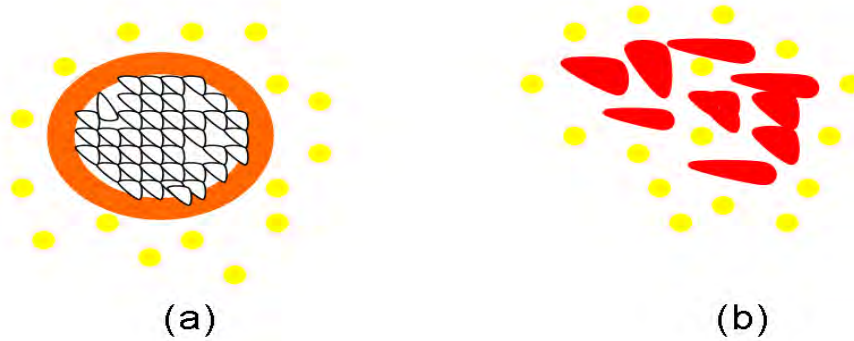
Figure 1.1 (a) Benign tumour: the fibrous connective tissue capsule (orange) separates the inside benign cells (black boundaries) from the outside normal cells (yellow). (b) Malignant tumour: the irregularly-shaped cancer cells (red boundaries) are anisotropic and non-localized.

in the biomechanical model, it remains a challenge to extract accurate results at high resolution in complex, heterogeneous tissues from the intrinsically noisy data. Therefore, any improvement in the MRE data processing with the help of biomechanics and computational methods will be of significant importance to modern medicine.

The aim of this paper is to formulate new mathematical models that will be able to differentiate not only between normal and abnormal tissues, but, more importantly, between benign (not cancerous) and malignant (cancerous) tumours. As it can be seen in Figure 1.1, benign tumours are localized, self-contained (encapsulated), with smooth boundaries, and tend to be more isotropic. On the other hand, malignant tumours are not localized, not self-contained, have irregular boundaries, and are anisotropic. Recent advancements in molecular biology [2] show that the cell-cell and cell-extracellular matrix adhesion forces play an important role in the localization of the tumours, with malignant tumours having a much poorer adhesion to the surroundings than benign tumours. It is important to notice that the cell-cell adhesions are rearranged dynamically during tissue development and tumour metastasis but the few existing mathematical models of the cell-cell adhesions are all static models. The modeling of the adhesion forces in normal tissues and tumours is still an open problem in mathematical biology.

In order for the MRE method to correctly classify the tumours of a given tissue as benign or malignant, the mathematical models of these two classes of tumours need to incorporate the differences between them. In the present paper we focus on mathematical models that incorporate information about microstructure and cellular adhesion forces. We pursued the following three approaches: (i) the simulation of the time-harmonic linear elastic models to examine coarse scale effects and adhesion properties, (ii) the investigation of a tri-phasic model, with the intent of upscaling this model to determine effects of electro-mechanical coupling between cells, and (iii) the upscaling of a simple cell model as a framework for studying interface conditions at malignant cells. The model used in simulation (i) is inspired by the dynamic MRE method where shear periodic forces are applied on the tissue [7].

2 Preliminary qualitative experiments

As a first step in developing a constitutive model that distinguishes benign and malignant cells, we consider a simple model of elastic waves propagating through inhomogeneous media. We start with a simple scalar PDE model (2.1) of transverse periodic waves propagating through an inhomogeneous, almost incompressible, linearly elastic tissue:

$$\frac{\partial^2 u}{\partial t^2} - \text{div}\left(\mu(x,y)\nabla u\right) = 0, \qquad (x,y) \in \left(-\frac{1}{2}, \frac{1}{2}\right)^2, \qquad (2.1\text{a})$$

$$u\left(x, -\frac{1}{2}\right) = \cos(\omega t), \qquad x \in \left[-\frac{1}{2}, \frac{1}{2}\right], \qquad (2.1\text{b})$$

$$\frac{\partial u}{\partial t} + \sqrt{\mu}\frac{\partial u}{\partial n} = 0, \qquad x = \pm\frac{1}{2}, \ y = \frac{1}{2}. \qquad (2.1\text{c})$$

The quantity u is the transverse displacement due to propagation of elastic waves and the quantity $\mu(x,y)$ is one of the Lamé coefficients, and n is the outward unit normal. Based on the fact that longitudinal waves propagate at much higher speeds than shear waves through biological tissues, we neglected any longitudinal effects. The boundary condition (2.1b) is the periodic force acting on the top of the domain that causes the transverse waves. The boundary condition (2.1c) is an absorbing (Sommerfeld) boundary condition to prevent reflection of waves. We generate simple finite-difference solutions of this wave equation to help us distinguish useful modelling criteria. We experiment with a simple geometry (a large tumour as in Figure 2.3) and a more complicated one (a cluster of smaller tumour cells as in Figure 2.4).

We assume that the motion within the tissue is time-periodic with a frequency equal to that of the forcing oscillations, ω. This allows the system (2.1) to be transformed into the frequency domain:

$$\omega^2 U + \text{div}\left(\mu\nabla U\right) = 0, \qquad (x,y) \in \left(-\frac{1}{2}, \frac{1}{2}\right) \times \left(-\frac{1}{2}, \frac{1}{2}\right), \qquad (2.2\text{a})$$

$$U = 1, \qquad y = -\frac{1}{2}, \qquad (2.2\text{b})$$

$$\sqrt{\mu}\frac{\partial U}{\partial n} + \imath\omega U = 0, \qquad x = \pm\frac{1}{2}, \ y = \frac{1}{2}, \qquad (2.2\text{c})$$

where U is the Fourier transformed displacement field at frequency ω.

The Sommerfeld condition (2.2c) introduces artifacts along the edges when waves are not traveling perpendicularly to the boundary. To combat this, the simulations were performed on a larger domain and then trimmed to remove the artifact. This effect is shown in Figure 2.1. Since most of the artifact is removed by trimming in this extreme case when waves are traveling parallel to the boundary, it is expected that this procedure will perform adequately when inclusions are introduced that deflect the travelling waves.

The system (2.2) was discretized on a rectangular grid, and converted into the following matrix problem:

$$L\widehat{U} = R, \qquad (2.3)$$

where $\widehat{U}$ is a vectorized version of the displacement field, and L is a sparse matrix representing the discrete version of the left-hand operator with right-hand terms R from System (2.2). This was solved in MATLAB using the backslash operator, which implements a
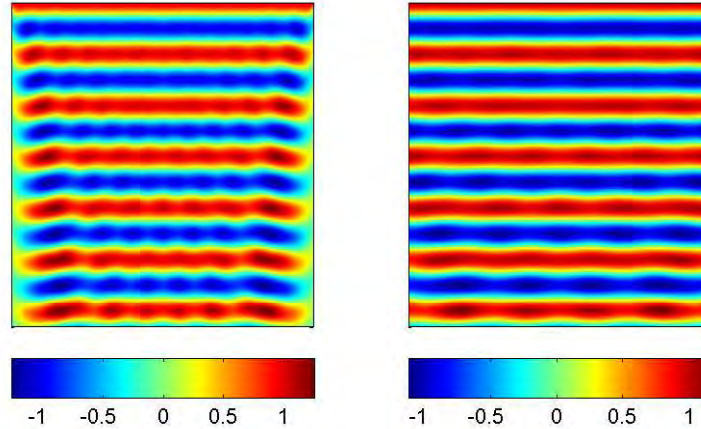
Figure 2.1 Left: Expanded domain with Sommerfeld conditions applied on the left, right and bottom sides. Right: trimmed domain to remove artifacts caused by the Sommerfeld conditions.

Table 2.1 Simulation Parameters

Grid Size	500×500 points
ω	100 Hz
$\mu_{\text{background}}$	250
$\mu_{\text{inclusion}}$	750

modified Sparse Cholesky Factorization method. The real component of the solution then represents the displacement field at time $t = 0$.

The lengths of the domain were scaled to be a unit square. The background stiffness of the material was then scaled to admit six full wavelengths, which corresponds to experiments performed on agar-agar gels in the MRE Lab at Mayo Clinic. The shear modulus for tumourous regions was set to three times that of the background to agree with the agar-agar experiments. Simulation parameters are summarized in Table 2.1.

Recall that benign tumours tend to adhere well to the surrounding normal tissue as compared to malignant tumours. Thus, for the full-adhesion simulations of benign tumours, we assume that there is a smooth, continuous transition between the background and tumour tissues. While the waves in Figure 2.3 change their wavelengths when passing through the stiffer tumourous regions (for reference see Figure 2.2 for the case without an inclusion), the waves in Figure 2.4 penetrate between the cluster of smaller tumours without a significant change of wavelengths. That is, there is a higher chance that the latter case will avoid detection when using the MRE technique.
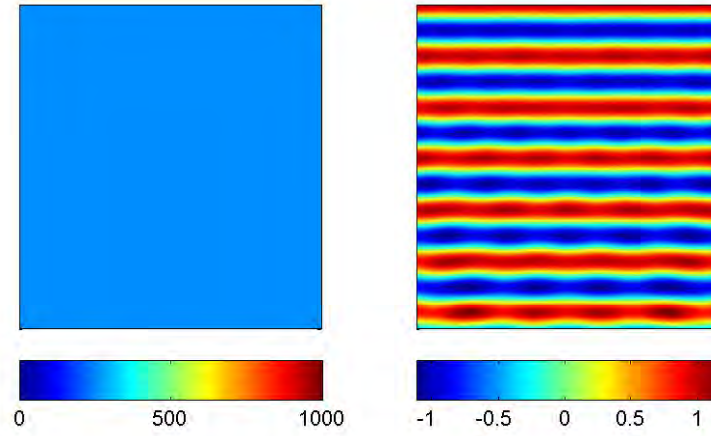
**Figure 2.2** Propagation of elastic waves with no inclusions.
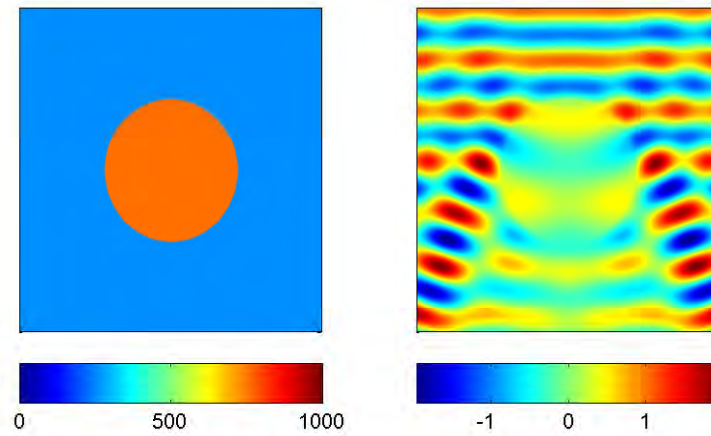
Figure 2.3 Propagation of elastic waves through a large tumour with perfect adhesion.
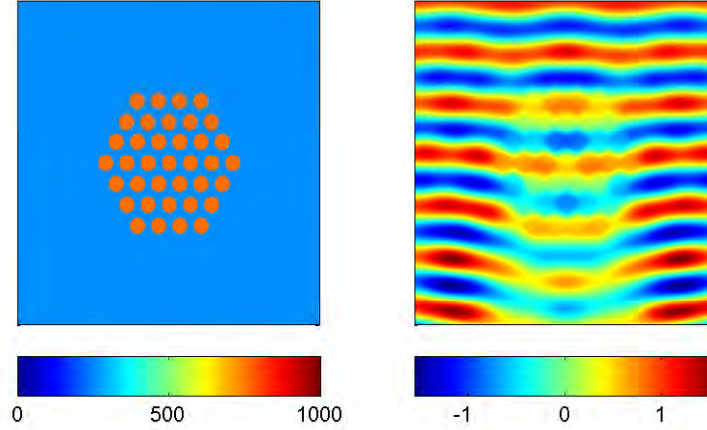
Figure 2.4 Propagation of elastic waves through a diffuse tumour with perfect adhesion.

To simulate a no adhesion property for malignant tumours, we impose a zero Neumann condition on the tumour-background tissue interface. To reduce complexity, normal derivatives along the interface were estimated using a first-order finite difference scheme. Because of this zero Neumann condition, the tumour regions are not affected by motions in the background material as seen in Figures 2.5 and 2.6.

In order to account for adhesive effects more realistically, we propose the following improved interface conditions to model cellular adhesions:

$$\mu \left[\frac{\partial U}{\partial n} \right]_{-}^{+} = \alpha [U]_{-}^{+}, \tag{2.4}$$

$$\mu \left[\frac{\partial U}{\partial \tau} \right]_{-}^{+} = 0, \tag{2.5}$$

where '+' indicates values in the background region, '−' indicates the tumour region, n is the normal direction at the interface from background to tumour, τ is the tangential direction, and α is an experimental jump parameter. Interface derivatives were estimated using first-order finite differencing. With this jump condition, points along the interface between background and tumour tissue must be repeated in $\widehat{U}$ in order to admit the two values U_{+} and U_{-} at each interface point. Results are presented in Figure 2.7.

These preliminary experiments support the conjecture that adhesion effects can be observed in the measured displacement field and hence motivate a deeper exploration of multiscaling models that incorporate them.
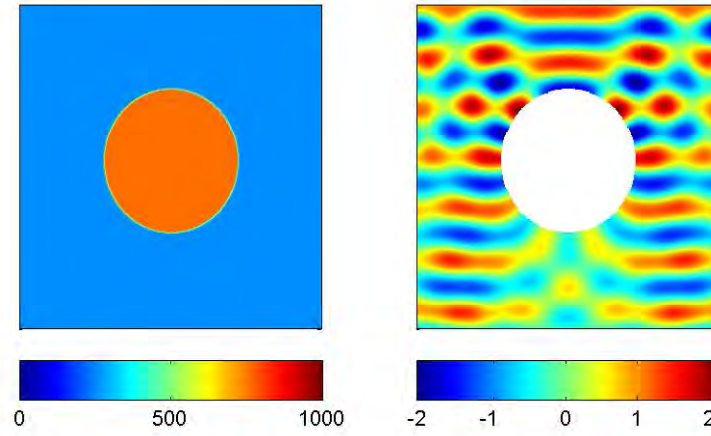
Figure 2.5 Propagation of elastic waves through a large tumour with no adhesion.
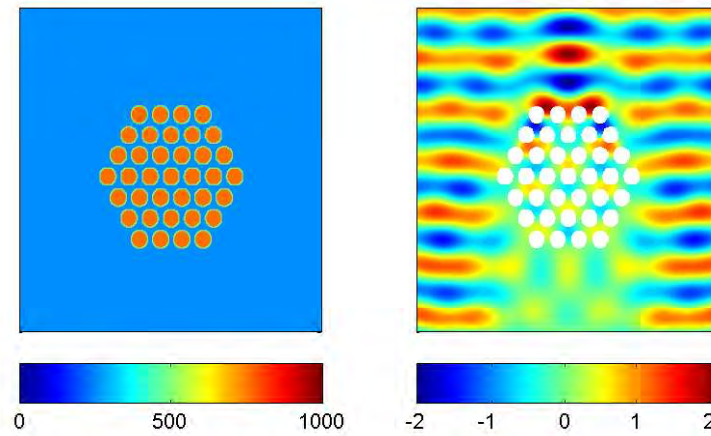

Figure 2.6 Propagation of elastic waves through a diffuse tumour with no adhesion.
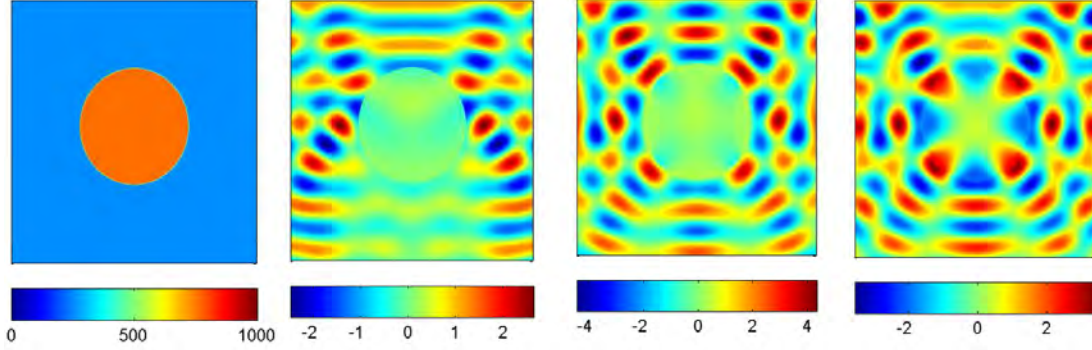
Figure 2.7 From left to right: $\alpha = 0$ (second image), $\alpha = 10^6$ (third image), and continuous boundary $U_- = U_+$ ($\alpha = \infty$) (forth image)

.

3 A tri-phasic model

Inspired by [12], we assume that a biological tissue is a mixture of an intrinsically incompressible, isotropic, porous-permeable-charged linear elastic solid phase containing the extracellular matrix and the (linear viscoelastic) solid cells, an intrinsically incompressible, isotropic, Newtonian viscous fluid phase containing the interstitial fluid, and an ion phase with, for now, two monovalent ion species: anion (-) and cation (+). The solid phase and the ion phase are electrically charged, while the fluid phase and the tissue as a whole are electrically neutral.

The constitutive equations are [5, 12]:

$$\sigma = -pI + \lambda_s eI + 2\mu_s\epsilon, \tag{3.1}$$
$$\mu^w = \mu_0^w + [p - RT(c^+ + c^-)\Phi + B_w e]/\rho^w, \tag{3.2}$$
$$\mu^+ = \mu_0^+ + (RT/M_+)\ln(\gamma_+ c^+) + F_c\psi/M_+, \tag{3.3}$$
$$\mu^- = \mu_0^- + (RT/M_-)\ln(\gamma_- c^-) - F_c\psi/M_-, \tag{3.4}$$

where the first equation is Hooke's law for the linear elastic phase, and the last equations are the constitutive equations for the fluid phase and the ion phase. We have denoted by p the fluid pressure, σ the stress tensor in the elastic solid, ϵ the strain tensor in the elastic solid with $e = \text{tr}(\epsilon)$ λ_s, μ_s the Lamé coefficients which depend on solid volume fraction and ion concentrations c^+, c^-, R is the universal gas constant, T is the absolute temperature, B_w is a coupling coefficient, μ^w is the chemical potential of the fluid phase, μ_0^w is the reference chemical potential of the fluid, Φ is the osmotic coefficient, ρ^w is the true mass density of the fluid, ψ is the electric potential, γ_+, γ_- are the activity potential coefficients, μ^+, μ^- are the electro-chemical potentials of the ion species with μ_0^+, μ_0^- the corresponding reference electro-chemical potentials, M_+, M_- are the molar weights of the ionic species, and F_c is the Faraday constant.

The governing equations are:

$$\operatorname{div} \sigma = \rho^s \frac{\partial \mathbf{v}^s}{\partial t}, \tag{3.5}$$

$$\operatorname{div} \mathbf{v}^s + \operatorname{div} \mathbf{J}^w = 0, \tag{3.6}$$

$$\frac{\partial (\phi^w c^+)}{\partial t} + \operatorname{div} \mathbf{J}^+ + \operatorname{div}\left(\phi^w c^+ \mathbf{v}^s\right) = 0, \tag{3.7}$$

$$\frac{\partial (\phi^w c^-)}{\partial t} + \operatorname{div} \mathbf{J}^- + \operatorname{div}\left(\phi^w c^- \mathbf{v}^s\right) = 0, \tag{3.8}$$

where ϕ^w is the porosity of the tissue and the water and ion fluxes relative to the solid phase are given by:

$$\mathbf{J}^w = \phi^w(\mathbf{v}^w - \mathbf{v}^s), \tag{3.9}$$

$$\mathbf{J}^+ = \phi^w c^+(\mathbf{v}^+ - \mathbf{v}^s), \tag{3.10}$$

$$\mathbf{J}^- = \phi^w c^-(\mathbf{v}^- - \mathbf{v}^s), \tag{3.11}$$

with $\mathbf{v}^s, \mathbf{v}^w, \mathbf{v}^+, \mathbf{v}^-$ the velocities of the corresponding phases. The governing equations need to be solved for the solid displacement and the water and ion fluxes. The boundary conditions are continuity of these unknown quantities across the boundaries between phases. It is important to notice that the continuity equations of the ions will need to be changed such that they model abnormal diffusion processes happening in a tissue when tumours appear and start to grow. We will address these modeling issues in our future work.

We assume further that a biological tissue is locally homogeneous at the macroscopic scale and its microstructure is made of periodic pores. Each electroneutral pore is saturated with the same amount of each of the three phases. The upscaling homogenization must be done in both spatial and temporal scales, since mechano-chemical processes at the micro-scale are faster than those at the macro-scale. For simplicity, we can take the Laplace transform of the governing equations and do only the homogenization in space for the Laplace transformed quantities. We introduce the small parameter $\alpha = x/X << 1$ with x the pore length scale, and X the macroscopic scale length, and assume that

$$f(x, X; \alpha) = f_0(x, X) + \alpha f_1(x, X) + \alpha^2 f_2(x, X) + \dots,$$

where f is any of the Laplace transforms of $\mathbf{u}^s, \mathbf{J}^w, \mathbf{J}^+, \mathbf{J}^-$. Then the corresponding α^n-order boundary value problems, $n = 0, 1, 2, \dots$ will have to be solved. We plan to report on the solutions to these problems in our further publications.

4 Up-scaling a malignant tumour model

We assume that malignant tumours are characterised by their cells' dispersion, lack of adhesion, and higher stiffness relative to surrounding normal tissue. As such, we develop an elastomeric model for malignant tumours based on a two-scale homogenization, where our aim is to present the macro-scale effect rendered by elastomeric interactions of individual tumour cells with normal tissue at the micro-scale.

Figure 4.1 gives a schematic of the classical two-scale homogenization approach. We assume some small length scale ϵ, in our case representing the size of a single malignant tumour cell. Assuming a small-scale pattern, we solve a so-called cell- or *unit*-problem at this scale, and use the solution to the unit-problem to present a PDE model with average parameters, effective at scales much larger than ϵ. From the perspective of resolving malignant
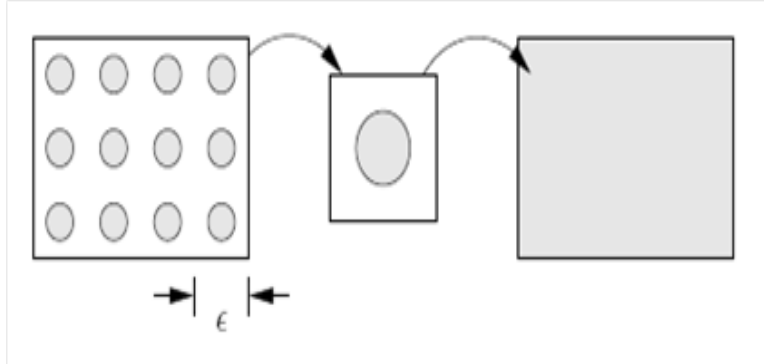
Figure 4.1 Schematic of up-scaling the dispersed malignant tumour model. From the periodic microscopic model at the left, we solve a pair of unit-problems [centre], and discover elastomeric parameters describing the average behaviour of the tissue at the large scale [right].

tumours, our expectation is that the parameters in the PDE up-scaled from this malignant cell model will differ greatly from those parameters representing a benign tumour.

Although we outline the development below, further details on two-scale homogenization for divergence-free systems can be found in several texts, see for example [6, 1].

4.1 Two-scale expansion. We examine a two-dimensional malignant cell model, whereupon the malignant cell is a circle in the centre of an ϵ-sized square, the remainder of the square representing healthy cells, see Figure 4.2. Our model is a PDE describing linear elastomerics in the time-harmonic case:

$$\begin{cases} \mathrm{div}(\mu \nabla u) + \omega^2 \rho u = 0, & x \in \Omega, \\ \left[\mu \dfrac{\partial u}{\partial n} \right]_-^+ = 0, & x \in \Lambda, \\ [u]_-^+ = 0, & x \in \Lambda, \end{cases} \tag{4.1}$$

In our setting, we recall that only the second of the Lamé parameters, μ, (also the shear modulus) appears, owing to the remarkable difference between shear and compression wave speeds, and our subsequent detection only of shear waves in tissue. Parameters ω and ρ are the driving frequency and tissue density, respectively, and the solution $u : \Omega \to \mathbb{C}$ is understood to be the complex amplitude of the time-harmonic wave over the domain Ω, representing the excited tissue. At Λ, the interface between the malignant cell and its healthy surroundings, we assign two boundary conditions. These conditions represent the strength of the attachment of the malignant cell to other tissue, understood in reality to be quite poor. The notation $[\cdot]_-^+$ represents the jump in the argument from one side of Λ to the other. The boundary conditions in (4.1) represent a cell that is well-attached to its
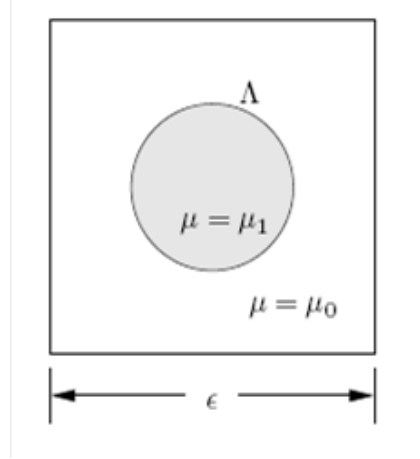
Figure 4.2 Unit cell geometry for up-scaling stiffness. The up-scaled stiffness parameter μ^* depends on the elastomeric stiffness parameter μ within and without of the malignant cell, as well as on the boundary conditions at the cell interface.

surroundings. In contrast, setting

$$\mu\frac{\partial u}{\partial n} = 0, \quad x \in \Lambda^+, \tag{4.2}$$

where Λ^+ represents the face of the boundary incident on the healthy cells, represents a malignant cell completely unadhered to the surrounding tissue. We examine these two extremes here, and suggest alternative boundary conditions which compromise between these two extremes at the end of this section. In any case, the up-scaled stiffness parameter μ^*, the effective stiffness at scales much larger than ϵ, will depend on the stiffness within and without of the malignant cell circle, as well as on the boundary conditions at the cell interface.

The up-scaling begins by assuming a two-scale solution,

$$u_\epsilon(x) = u(x, x/\epsilon) = u(x, y) \sim u_0 + \epsilon u_1 + \epsilon^2 u_2 + \dots, \tag{4.3}$$

where u_ϵ is periodic in y, based on the observation that the shear modulus $\mu = \mu(x/\epsilon) = \mu(y)$. We refer to our ϵ-domain as $\mathcal{Y}$, which has unit area, and over which we have periodic boundary conditions. Applying this expansion to our model (4.1), we have

$$\epsilon^{-2}\left[\mathrm{div}_y(\mu\nabla_y u_0)\right] \tag{4.4}$$

$$+ \epsilon^{-1}\left[\mathrm{div}_y(\mu(\nabla_x u_0 + \nabla_y u_1)) + \mathrm{div}_x(\mu\nabla_y u_0)\right] \tag{4.5}$$

$$+ \epsilon^0\left[\mathrm{div}_x(\mu(\nabla_x u_0 + \nabla_y u_1)) + \mathrm{div}_y(\mu(\nabla_x u_1 + \nabla_y u_2)) + \rho\omega^2 u_0\right] \tag{4.6}$$

$$+ \mathcal{O}(\epsilon) = 0. \tag{4.7}$$

The $\mathcal{O}(\epsilon^{-2})$-term, combined with the periodic boundary conditions, gives $u_0 = u_0(x)$. Since $\nabla_y u_0 = 0$, the $\mathcal{O}(\epsilon^{-1})$ equation is

$$-\operatorname{div}_y(\mu\nabla_y u_1) = \operatorname{div}_y(\mu\nabla_x u_0(x)). \tag{4.8}$$

That is, the adjustment u_1 depends linearly on $u_0(x)$, and we can write

$$u_1(x,y) = \sum_{i=1}^{2} w_i \partial_{x_i} u_0, \tag{4.9}$$

where

$$-\operatorname{div}_y(\mu\nabla_y w_i) = \operatorname{div}_y(\mu\mathbf{e}_i) \tag{4.10}$$

together with boundary conditions on Λ form the *unit*-problem for the homogenization. $\mathbf{e}_i$ are unit basis vectors.

In the $\mathcal{O}(1)$-term in (4.7), we apply the $\mathcal{Y}$-periodicity of the solution, observing that

$$\int_{\mathcal{Y}} \operatorname{div}_y(\mu(\nabla_x u_1 + \nabla_y u_2)) = \int_{\partial\mathcal{Y}} \mu(\nabla_x u_1 + \nabla_y u_2)^T \widehat{n} = 0. \tag{4.11}$$

Thus, substituting $\nabla_x u_0(x) = \sum_{i=1}^{2} \mathbf{e}_i \partial_{x_i} u_0$, the linear dependence of u_1 on $\nabla_x u_0$ gives the $\mathcal{O}(1)$ equation

$$\operatorname{div}_x\left[\sum_{i=1}^{2}\left(\int_{\mathcal{Y}} \mu(\mathbf{e}_i + \nabla_y w_i)\right)\partial_{x_i} u_0\right] + \rho\omega^2 u_0 = 0. \tag{4.12}$$

Finally, observing that as a weak solution to the unit-problem, the w_i satisfy

$$\int_{\mathcal{Y}} (\mathbf{e}_i + \nabla_y w_i)^T \mu\nabla_y w_j = 0, \tag{4.13}$$

we can rewrite (4.12) as

$$\operatorname{div}(\mu^*\nabla u_0) + \rho\omega^2 u_0 = 0, \tag{4.14}$$

where

$$\mu_{ij}^* = \int_{\mathcal{Y}} (\mathbf{e}_i + \nabla_y w_i)^T \mu(\mathbf{e}_j + \nabla_y w_j) \tag{4.15}$$

is the *up-scaled shear modulus*. The up-scaled modulus is clearly symmetric, and it is possible to show that provided $\mu(y) > 0$, then the operator resulting from μ^* is uniformly elliptic. Although it is common practise to normalize this integral by the volume of the unit cell, we have chosen $\operatorname{Vol}(\mathcal{Y}) = 1$ in this case.

Note that in general, even if μ is a scalar at the scale of the unit-problem, representing an isotropic shear modulus, expression (4.15) shows that it may not be scalar when up-scaled. In our setting, however, we have chosen the inclusion in our unit-problem to be circular. This avoids setting any preferred direction in our problem, and hence we expect our up-scaled shear modulus to be isotropic.

We have ignored any contribution of the Helmholtz term to the up-scaling calculation. It could happen, however, that for specific frequencies, $\omega \sim C/\epsilon$ for some constant C. In this setting, we would have to consider the effect of resonance at the scale of the unit problem, where the unit problem becomes an eigenvalue problem

$$-\operatorname{div}(\mu\nabla\phi) + (\rho\omega^2 - \lambda)\phi = 0. \tag{4.16}$$

See the lecture notes [10] for further details. Indeed, there is current research [13] in this area with respect to cancer treatments, where shear waves are tuned to resonate with and burst apart malignant cells. We do not pursue this case further here.
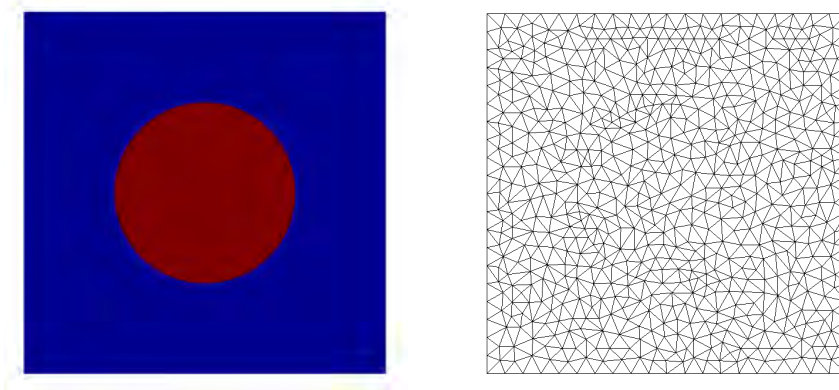
Figure 4.3 Numerical domain for the unit-problems. We discretize the unit-problem containing a tumour cell as a circular inclusion [left] using triangular finite elements [right].

4.2 Numerical results. We next examine two specific cases where we numerically solve unit-problems to up-scale the elastomeric effects of dispersed cells. In the first case, we solve

$$
\begin{cases}
-\operatorname{div}(\mu \nabla w_i) = \operatorname{div}(\mu \mathbf{e}_i), & x \in \mathcal{Y}, \\[2mm]
\left[\mu \dfrac{\partial u}{\partial n}\right]_-^+ = 0, & x \in \Lambda, \\[2mm]
[u]_-^+ = 0, & x \in \Lambda, \\[1mm]
w_i \text{ are } \mathcal{Y}\text{-periodic.}
\end{cases}
\tag{4.17}
$$

This unit-problem represents the case where the malignant cell is well-adhered to the surrounding tissue. We are aware that this case represents the opposite of our understanding of the biology, and we provide it for comparison with the following, more realistic model.

The second case we consider is

$$
\begin{cases}
-\operatorname{div}(\mu \nabla w_i) = \operatorname{div}(\mu \mathbf{e}_i), & x \in \mathcal{Y}, \\[2mm]
\mu \dfrac{\partial u}{\partial n} = 0, & x \in \Lambda^+, \\[1mm]
w_i \text{ are } \mathcal{Y}\text{-periodic.}
\end{cases}
\tag{4.18}
$$

This represents a tumour cell completely unadhered to its surroundings. Although an extreme representation, it is straightforward to implement, and will suggest the effect boundary conditions present at the micro-scale can have on the up-scaled shear modulus.

In both cases, we choose $\mu = \mu_0 = 1$ in the healthy tissue, and $\mu = \mu_1 = 3$ in the malignant cell. A ratio of $\mu_0 : \mu_1 = 1 : 3$ is consistent with laboratory measurements of the shear modulus of healthy and cancerous tissue. Figure 4.3 shows the unit cell, discretized using triangular finite elements. We use Jonathan Shewchuk's Triangle program [11] to produce the triangulation.
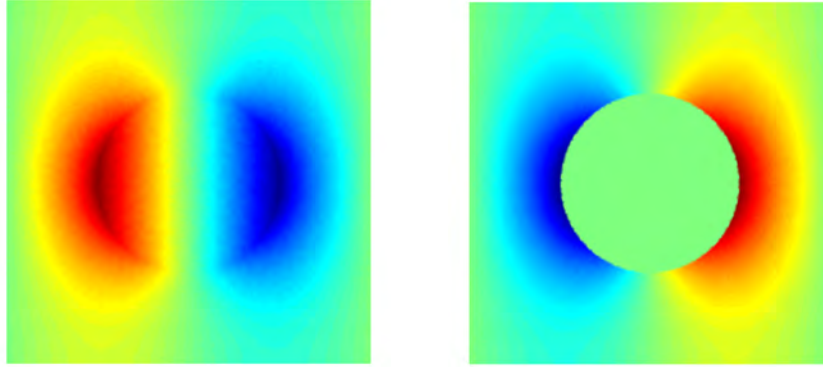
Figure 4.4 Well-adhered [left] and poorly-adhered [right] model unit-problems contrasted. Note that no information reaches the interior of the model cell in the case where the cell is poorly-adhered to its surroundings. Only the solutions to the x-direction unit-problem are shown: the y-direction solutions are simply these solutions rotated 90-degrees.

Table 4.1 Results of two contrasting unit problems. The shear modulus of the well-adhered cell is nearly double that of the case where the model cell is poorly-adhered to its surroundings.

Well-adhered problem (4.17)	$\mu^* = 1.22$
Poorly-adhered problem (4.18)	$\mu^* = 0.672$

Figure 4.4 contrasts the unit-problems for the well-adhered and poorly-adhered cases. (We show only the x-direction problems in each case. The y-direction problems are identical, only rotated 90-degrees.) The difference in the two problems is striking, showing the lack of flow of any information to the interior of the model cell in the case where the cell is poorly-adhered. This surely has an effect on the up-scaled shear modulus, as we see in the final results.

Table 4.1 summarizes our results, computing the integrals in (4.15) from the solutions in Figure 4.4. As anticipated by our choice of circular inclusion in the unit-problem, the up-scaled shear modulus is isotropic and we report only the diagonal values of (4.15). In summary, the case where the cell is poorly-adhered has a shear modulus half that of the well-adhered case. This indicates that the adherence of the malignant cells to the surrounding healthy cells can distinguish them from other cells, despite the small-scale dispersion of the malignant cells.

4.3 Further work. Following the homogenization framework, we propose several extensions to this up-scaling. The two most important modifications to the above model are to the boundary conditions at the malignant-normal cell interface, Λ, above, and to the choice of the shape of Λ.

Boundary conditions: We propose modeling the interface between normal and malignant cells according to the schematic of Figure 4.5. The schematic shows the cross-linking structures present between all cells, but in fewer number and stiffness between malignant cells and their surroundings. This reduced number of cross-links is precisely what reduces the adhesion between infected and normal cells, and affects a spring constant relating the normal stresses to the displacements of the cells, just as for one-dimensional Hooke's springs.
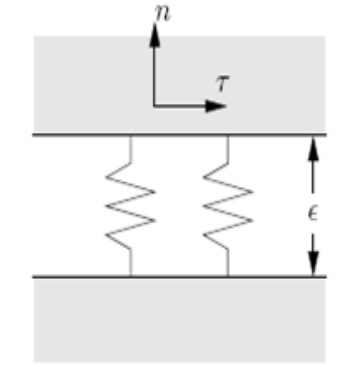
Figure 4.5 Model of the interface between normal and malignant cells. The density and strength of the cross-links, represented as wiggly lines, determines an effective spring constant relating normal stresses on each surface. Not shown is the visco-elastic effect of the fluid between the surfaces.

Furthermore, not shown in the schematic, the thin layer of pseudo-fluid between infected and normal cells gives a visco-elastic relationship between the two surfaces, such that the tangential stresses on the two surfaces are related to the relative strain rate of the surfaces. Combining the normal, n, and tangential τ, stress effects, we suggest the boundary conditions

$$\left[\mu\frac{\partial u}{\partial n}\right]_{-}^{+} = -\alpha\,[u]_{-}^{+}, \tag{4.19}$$

$$\left[\mu\frac{\partial u}{\partial \tau}\right]_{-}^{+} = -i\omega\beta\,[u]_{-}^{+}. \tag{4.20}$$

Note the imaginary number $i = \sqrt{-1}$ in the tangential condition, corresponding to a time-derivative for representing the strain rate.

The separation distance between cells, ϵ in Figure 4.5, is assumed sufficiently small that the constants α, β effectively summarize the adhesive properties of the malignant cell. Although the adhesion constants depend on properties of the normal-malignant interface we change the strain rate experimentally by tuning the driving frequency ω. Such tuning may allow us to take advantage of the particular adhesion coefficients in order to better detect malignant cells in the up-scaled shear stress.

Owing to the additional data structure required to represent this solution (two values for u are required on each mesh vertex on Λ) implementing this condition, and understanding its contribution to the up-scaled constitutive law, will have to remain future work for the time being.

Random cell orientation: Although the choice of a spherical malignant cell is realistic insofar as it predicts no anisotropy in the up-scaled constitutive law, malignant cells are more likely to be football-shaped, such as that depicted in Figure 4.6, with orientation or
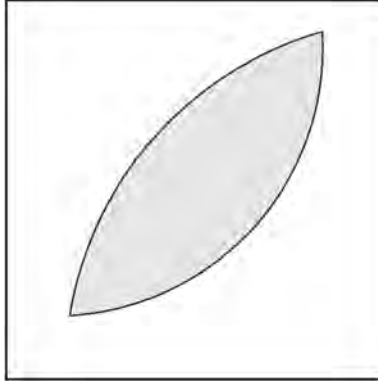
Figure 4.6 A more realistic malignant cell model shape. To avoid anisotropy in the up-scaled constitutive law, the orientation or other features of the cell geometry will have to be chosen in a random manner.

other features of the cell geometry being random. Such stochastic homogenization, where the aim is to compute the statistics of the constitutive law from the statistics of, in our case, the cell geometry, has been studied, and appears, for example, in lecture notes [10]. However, this is beyond the scope of our present investigation, and further study is required to see the effects of up-scaling a randomized unit problem.

5 Conclusion

The aim of this paper was to formulate new mathematical models that will be able to differentiate not only between normal and abnormal tissues, but, more importantly, between benign and malignant tumours. We pursued the following three approaches: (i) the simulation of the time-harmonic linear elastic models to examine coarse scale effects and adhesion properties, (ii) the investigation of a tri-phasic model, with the intent of upscaling this model to determine effects of electro-mechanical coupling between cells, and (iii) the upscaling of a simple cell model as a framework for studying interface conditions at malignant cells. Each of these approaches has opened exciting new directions of research that we plan to study in the future.

References

[1] G. Allaire, *Shape optimization by the homogenization method*, Springer-Verlag, 2002.

[2] A. Besser, U.S. Schwarz, *Coupling biochemistry and mechanics in cell adhesion: a model for inhomogeneous stress fiber contraction*, New J. Phys. **9** (2007), 1-27.

[3] F. A. Duck, *Physical Properties of Tissues- A Comprehensive Reference Book*, 6th edition, Sheffield, UK: Academic, 1990.

[4] Y.C. Fung, *Biomechanics - Mechanical Properties of Living Tissues*, 2nd edition, Springer, New York, 1993.

[5] W.Y. Gu, W.M. Lai and V.C. Mow, *A mixture theory for charged-hydrated soft tissues containing multi-electrolytes: passive transport and swelling behaviors*, J. Biomech. Engrg. **120** (1998), 169-180.

[6] U. Hornung, *Homogenization and porous media*, Springer-Verlag, 1997.

[7] A. Manduca, T.E. Oliphant, M.A. Dresner, J.L. Mahowald, S.A. Kruse, E. Amromin, J.P. Felmlee, J.F. Greenleaf and R.L. Ehman, *Magnetic resonance elastography: non-invasive mapping of tissue elasticity*, Med. Imag. Anal. **5** (2001), 237-254.

[8] R. Muthupillai, D.J. Lomas, P.J. Rossman, J.F. Greenleaf, A. Manduca and R.L. Ehman, *Magnetic resonance elastography by direct visualization of propagating acoustic strain waves*, Science **269** (1995), 1854-1857.

[9] R. Muthupillai, P.J Rossman, D.J. Lomas, J.F. Greenleaf, S.J. Riederer and R.L. Ehman, *Magnetic resonance imaging of transverse acoustic strain waves*, Magn. Reson. Med. **36** (1996), 266-274.

[10] A. Papanicolaou, *Diffusion in Random Media*, Lecture Notes, `ftp://math.stanford.edu/pub/papers/papanicolaou/make.pdf`, accessed June 2009.

[11] J. Shewchuk, *Triangle: A Two-Dimensional Quality Mesh Generator and Delaunay Triangulator*, Software, `http://www.cs.cmu.edu/ quake/triangle.html`, accessed June 2009.

[12] D.N. Sun, W.Y. Gu, X.E. Guo, W.M. Lai and V.C. Mow, *A mixed finite element formulation of triphasic mechano-electrochemical theory for charged, hydrated biological soft tissues*, Int. J. Numer. Meth. Engng. **45** (1999), 1375-1402.

[13] J. Tuszynski, private communication.

A Mechanism for Ventricular Expansion in Communicating Hydrocephalus

Problem Presenter: Miles Johnston (Sunnybrook Health Sciences Centre)

Contributors: Julia Arciero (University of Pittsburgh), Ronald Begg (University of Waterloo), Katie Ferguson (University of Waterloo), Raluca Jessop (University of Waterloo), Miles Johnston (Sunnybrook Health Sciences Centre), Shailesh Naire (Keele University), Brenda Orser (B.I.O. Letha Information Systems, Inc.), Trevor Sherk (UOIT), Siv Sivaloganathan (University of Waterloo), Kathleen Wilkie (University of Waterloo), Wei Yao (York University)

Report prepared by: Ronald Begg and Kathleen Wilkie[1]

Abstract. This report investigates a new possible molecular mechanism for the pathogenesis of hydrocephalus. New research by Dr. Miles Johnston [4] has found that the injection of anti β_1 integrin antibodies into the ventricle of rats causes a drop in parenchymal pressure and causes the cerebral ventricles to enlarge which is characteristic of hydrocephalus. We investigate intramantle pressure gradients as a possible force to enlarge the ventricles and we propose a new poroelastic model incorporating the effect of the antibodies to determine if they are a possible mechanism for hydrocephalus.

1 Introduction

Hydrocephalus is a condition of the brain characterized by an accumulation of cerebrospinal fluid (CSF) in the brain and the resulting expansion of the cerebral ventricles and compression of the brain parenchyma. The four ventricles of the brain (two lateral, one third and one fourth ventricle) are located in the centre of the brain tissue and CSF flows from the lateral ventricles through the aqueducts to the third and fourth ventricles into the subarachnoid space. CSF also flows through the brain tissue into the subarachnoid space where it circulates with the spinal CSF and is absorbed by the arachnoid villi.

There are two classes of hydrocephalus: the first class, non-communicating hydrocephalus, occurs when there is an obstruction to the normal flow and circulation of CSF causing it to accumulate in the ventricles. Due to the obstruction (such as a tumour) a large

---

[1] kpwilkie@uwaterloo.ca

pressure gradient exists between the ventricles and the subarachnoid space surrounding the brain parenchyma. This large pressure gradient is the cause of the ventricular expansion that occurs in this class of hydrocephalus.

Communicating hydrocephalus, the second class of hydrocephalus, occurs when there is no impediment to the normal flow of CSF from the ventricles, but when there is an imbalance between the production and absorption of CSF. Large pressure gradients cannot exists across the parenchyma in this class and so there is no obvious mechanism to explain the ventricular enlargement that occurs. This lack of a physical mechanism for ventricular expansion in communicating hydrocephalus was the focus of our study group.

1.1 Previous investigations. Linninger *et al.* [3] placed pressure sensors (transducers) in the ventricular CSF, the brain parenchyma, and the CSF of the subarachnoid space and showed that no significant difference was visible between the measured pressures before and after inducing kaolin hydrocephalus in dogs. However, it is possible that small, and perhaps transient, pressure differences do exist between the ventricular CSF and the brain parenchyma or subarachnoid space which were below the sensitivity of the transducers and which could provide a possible mechanism for ventricular enlargement.

In 2002, Peña *et al.* [5] numerically simulated hydrocephalus using a finite element method to solve Biot's equations of consolidation [1], now known as poroelasticity theory. They showed that a drop in parenchymal pressure coupled with a reduced elastic modulus produced the ventricular enlargement characteristic of hydrocephalus. In order to maintain a low pressure region inside the parenchyma, they assumed that CSF was absorbed by the parenchyma, which was represented mathematically by inserting sink terms into Biot's equations. No physical explanation of the reduced elasticity or of the absorption process was given.

Recent experiments by Wiig *et al.* [8] showed that the dissociation of $\alpha_1\beta_1$ integrins in the skin results in a significant reduction in the local interstitial fluid pressure. Nagra *et al.* [4] showed that this reduction in local pressure also occurs in brain parenchyma which suggests that β_1 integrin dissociation may provide a possible mechanism for the pathogenesis of hydrocephalus.

In Johnston's experiments [4], either antibodies to β_1 integrins or IgG/IgM isotype controls were injected into the lateral ventricle of adult rats. The ventricular or parenchymal pressures (measured 500-600 μm from the anterior horn of the lateral ventricle) were recorded with a servo-null micropipette (2 μm tip) before and after the antibodies or controls were injected in one group of rats. These measurements showed that following the injection of antibodies, the parenchymal pressure decreased relative to the pre-injection value. This drop in parenchymal pressure was not observed when controls were injected.

The remaining rats were sacrificed two weeks post injection and the brains were fixed with 10% formalin before coronal sections were obtained. The rats that received controls presented no ventricular enlargement but the rats that received anti β_1 integrin antibodies presented considerable ventricular enlargement.

Dr. Miles Johnston presented these results to the OCCAM-Fields-Mitacs workshop and proposed the following questions to our study group.

Question 1: Can one predict a ventricle size given a defined pressure gradient between the ventricles and the periventricular area?

Question 2: What is the smallest pressure gradient that would expand the ventricles?

These questions are difficult to answer accurately due to the dependence of tissue deformation on the material properties of brain parenchyma, which are difficult to determine experimentally and which vary in the reported literature. The second question is also difficult to answer since it is not quantitative in nature. Any applied pressure gradient would expand the ventricles by some amount, however small that expansion may be.

This study addresses two objectives that aim to answer or extend the concepts of interest to Dr. Johnston.

Objective I: To determine the percentage of ventricular volume increase that occurs due to an intramantle pressure gradient of $400 - 500$ Pa and investigate the dependence of this increase on the pressure distribution through the brain parenchyma.

Objective II: To formulate a model to investigate the hypothesized macroscopic mechanical effects of anti β_1 integrin antibodies on brain parenchyma to determine if they are sufficient to induce hydrocephalus.

2 Intramantle Pressure Gradients - Objective I

To predict the ventricular volume increase given a prescribed pressure difference between the ventricles and the periventricular area (intramantle gradient), by defining a pressure distribution across the parenchyma, we use previous studies to define governing equations for our specific problem. In previous models of hydrocephalus [7, 2, 6] differential equations are used to describe the radial displacements of brain parenchyma in a simplified geometry, shown in Figure 1. In all three models, the brain is assumed to have a spherical or cylindrical geometry, and displacement and pressure distributions are assumed to be radially symmetric, allowing the differential equation to be solved in one-dimension.

These models are based on Biot's theory of consolidation [1] which describes the behaviour of porous elastic media under loads. The main limitation of Biot's theory is that it is based on linear elasticity, which is only applicable for small strains. To account for large strains, nonlinear elasticity should be used, however this is mathematically much more complicated.

The poroelastic model developed by Levine [2] is implemented to address the first objective in this study. MAPLE and MATLAB are used to solve the equations derived by Levine [2] describing parenchymal displacement in the spherical brain given a defined pressure distribution. The steady pressure profile was also determined according to Levine's theory [2].

2.1 Equations for displacement. Levine's equation for radial displacement is obtained from the quasi-static version of Biot's equations [1] assuming the displacement function u and pressure distribution P are radially symmetric. If we write $u(r)$ for the radial displacement at radius r, the following equation (given by Levine [2]) relates radial displacement and pressure:

$$\frac{\partial^2 u}{\partial r^2} + \frac{2}{r}\frac{\partial u}{\partial r} - \frac{2u}{r^2} = \frac{(1-2\nu)\alpha}{2G(1-\nu)}\frac{\partial P}{\partial r}, \tag{2.1}$$

where G is the shear modulus and ν is the Poisson's ratio of the saturated poroelastic solid. The parameter α, according to Biot [1], represents the ratio of the volume of fluid squeezed out to the volume change of the parenchyma if the parenchyma is compressed while allowing fluid to escape. In the following, the brain tissue is assumed to be incompressible. If the
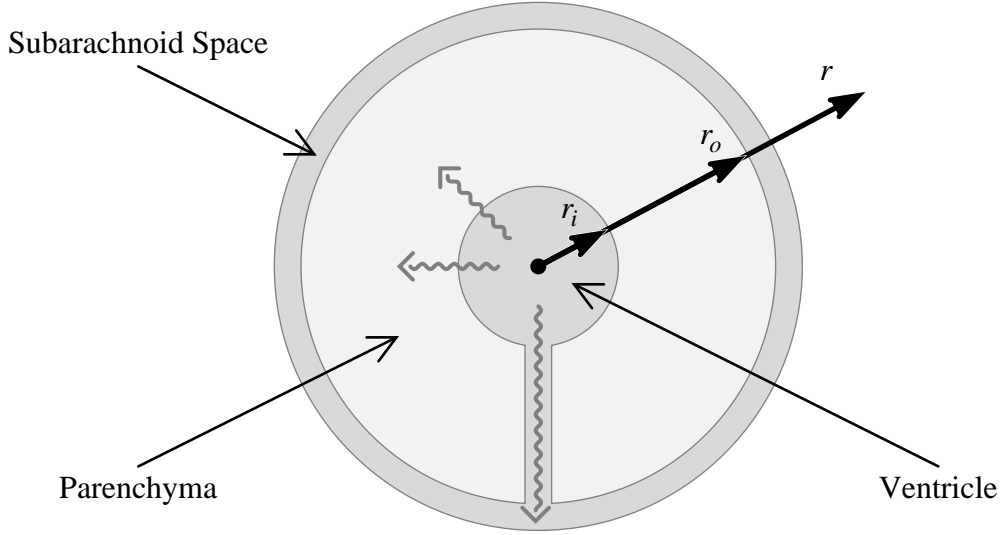
Figure 1: Schematic of the spherical brain. The brain is assumed to be a sphere, with a concentric spherical void in the middle representing the ventricles. CSF may either flow through the parenchyma or out through a channel representing the foramena and aqueduct. For our purposes, we consider the channel to be small enough that it does not affect the displacements near it. This allows for radially symmetric functions and reduces the number of dimensions in the problem.

parenchyma is compressed, the volume loss must be solely due to fluid loss or pore shrinkage. Thus, in the following, we assume that $\alpha = 1$.

Boundary conditions at the inner and outer boundaries of the brain are defined for (2.1). At the inner boundary, located at $r = r_i$, equivalent normal forces must act on the fluid phase and the solid phase. Assuming zero rate of strain within the ventricle this translates, in the radial formulation of Levine[2], as:

$$(\alpha - 1)P(r_i) = \left[2G\frac{\partial u}{\partial r} + \frac{2G\nu}{1 - 2\nu}\left(\frac{\partial u}{\partial r} + 2\frac{u}{r}\right)\right]_{r=r_i}. \tag{2.2}$$

At the outer boundary, $r = r_o$, there are two possible boundary conditions. One option is to impose the same condition on the forces at the outer boundary as at the inner boundary. This gives the boundary condition:

$$(\alpha - 1)P(r_o) = \left[2G\frac{\partial u}{\partial r} + \frac{2G\nu}{1 - 2\nu}\left(\frac{\partial u}{\partial r} + 2\frac{u}{r}\right)\right]_{r=r_o}. \tag{2.3}$$

This condition describes hydrocephalus in infants where the unfused skull may deform to accommodate the enlarged brain.

Levine imposes the following condition describing adult hydrocephalus:

$$u(r_0) = 0, \tag{2.4}$$

---

[2]It is our opinion that Levine has a mistake at this stage. On the left hand side of the Equation (2.2) Levine would have $-P(r_i)$ according to equation (14) of [2], but this disagrees with both Equation (12) from [7] and Equation (4.3) from [6]. Levine seems to neglect the $-\alpha P$ term in the first of the equations (12) in [2]. Equation (2.2) is what we believe to be correct.

which enforces zero displacement at the outer boundary due to the rigid skull preventing radial expansion of the outer surface of the brain. This boundary condition, however, excludes contraction of the outer surface of the brain which means the brain behaves like it is welded to a perfectly rigid skull at the outer boundary.

If the model always predicts positive radial displacement then this is not a problem, since the boundary condition prevents expansion. However, in some cases the pressure distributions cause negative radial displacement near the outer boundary, indicating that the imposed boundary condition is preventing contraction of the outer surface of the brain.

The appropriate course may be to solve for the displacement using the boundary condition (2.3) and then, if $u(r_o) > 0$, apply a corrective radial traction at the outer boundary such that $u(r_o) = 0$. The magnitude of the corrective traction will correspond to the force exerted on the brain by the skull. The end result should be equal to that obtained by replacing (2.3) with (2.4).

2.2 Equations for pressure. The models in [7, 2, 6] all include a differential equation describing the pressure distribution in the brain. They are based on the static or quasi-static assumption that the volume fraction of the brain occupied by CSF at each point does not vary in time, and that the flow of fluid in the brain obeys Darcy's law. Levine [2] writes these equations as:

$$V_r(r) = -k'\frac{\partial P}{\partial r}, \tag{2.5}$$

$$V_{ab} = \hat{k}P, \tag{2.6}$$

$$\frac{\partial \zeta}{\partial t} = k'\left(\frac{\partial^2 P}{\partial r^2} + \frac{2}{r}\frac{\partial P}{\partial r}\right) - \hat{k}P. \tag{2.7}$$

Here, $V_r(r)$ is the radial flow of CSF, which corresponds to $\phi v(r)$, where ϕ is the volume fraction of CSF at a given point and $v(r)$ is the radial velocity of the fluid at the same point. Equation (2.5) is Darcy's law where k' is the hydraulic permeability of the parenchyma. Equation (2.6) is Starling's law which relates the volume of CSF absorbed per unit volume of the parenchyma per unit time (V_{ab}) to the pressure difference across the capillary wall. Here $\hat{k}$ is the absorbtion coefficient. This equation assumes that blood pressure and net colloid osmotic pressures sum to zero, leaving P as the driving force behind the transfer of fluid from the interstitium into the capillaries. Equation (2.7) gives an expression for the increment of fluid content, $\zeta = \zeta(r,t)$, in the parenchyma ($\zeta = \phi - \phi_0$, if ϕ_0 is the initial volume fraction of fluid in the parenchyma). The two factors affecting the volume fraction of fluid are the absorbtion of fluid by capillaries and the divergence of the fluid flow.

In the quasi-static case, where $\dfrac{\partial \zeta}{\partial t} = 0$, we have

$$\frac{d^2 P}{dr^2} + \frac{2}{r}\frac{dP}{dr} - \frac{\hat{k}}{k'}P = 0. \tag{2.8}$$

The boundary conditions specified by Levine [2] are:

$$P(r_i) = P_v \qquad \text{and} \qquad P(r_o) = 0,$$

where P_v is the ventricular pressure. However, in communicating hydrocephalus the ventricular space and the subarachnoid space are connected via the cerebral aqueduct, so the boundary conditions should be closer to

$$P(r_i) = P(r_o) = P_v. \tag{2.9}$$

2.3 Radial displacement and ventricular expansion. It is probable that the absorbtion and permeability coefficients vary spatially and thus by choosing $\hat{k}$ and k' appropriately, one may obtain a pressure profile of any desired shape. For now, these coefficients are assumed to be constant and their ratio is defined as $k = k'/\hat{k}$. Equation (2.8) is solved subject to (2.9) to obtain pressure profiles for various values of the ratio k.

Figure 2 illustrates the dependence of this pressure distribution on the ratio k as well as the dependence of the parenchymal displacement (determined by (2.1) with boundary conditions (2.2) and (2.4)) on the pressure profile. When absorption is equal to permeability ($k = 1$), pressure drops only slightly mid-parenchyma which causes the negligible deformation seen in Figure 2b. When absorption dominates permeability ($k \ll 1$), significant drops in pressure occur mid-parenchyma and small negative displacements result near the outer surface of the brain.
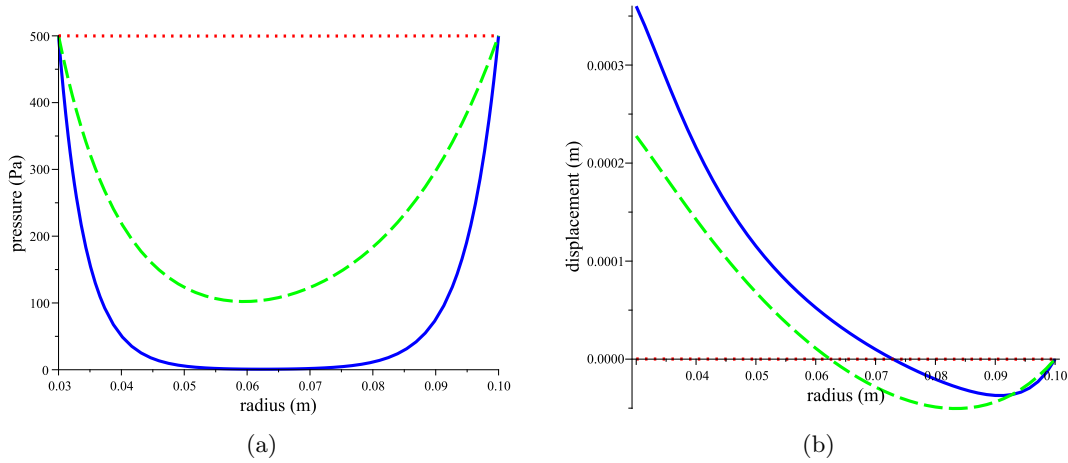

Figure 2: (a) Pressure profiles obtained by solving (2.8) with (2.9) for various values of k, and (b) the corresponding displacements obtained by solving (2.1) with boundary conditions (2.2) and (2.4). The red dotted curves are for $k = 1$ and the blue solid and green dashed curves are for $k \ll 1$ ($G = 8$ kPa and $\nu = 0.35$).

If a small pressure gradient from the ventricles to the subarachnoid space was applied as well as the given pressure distribution through the parenchyma, the negative displacements near the outer boundary may be changed to positive displacements. A small pressure gradient, less than 1 mmHg, would be below the sensitivity of the transducers used by Linninger et al. [3], and thus would not have been observed in their measurements.

To investigate the dependence of displacement on the shape of the pressure distribution through the parenchyma, two types of pressure profiles were constructed, inverted spike profiles and trough profiles. The constructed pressure profiles and their corresponding displacements according to (2.1) with (2.2) and (2.4) are shown in Figure 3. The pressure spikes cause the majority of the parenchyma to move inward while the ventricle walls move outward creating compression in the middle of the parenchyma. The trough profiles cause the majority of the parenchyma to move outward while a region near the outer boundary moves inward, again creating compression of the parenchyma.

(a) Spikes

(b)

(c) Troughs

(d)
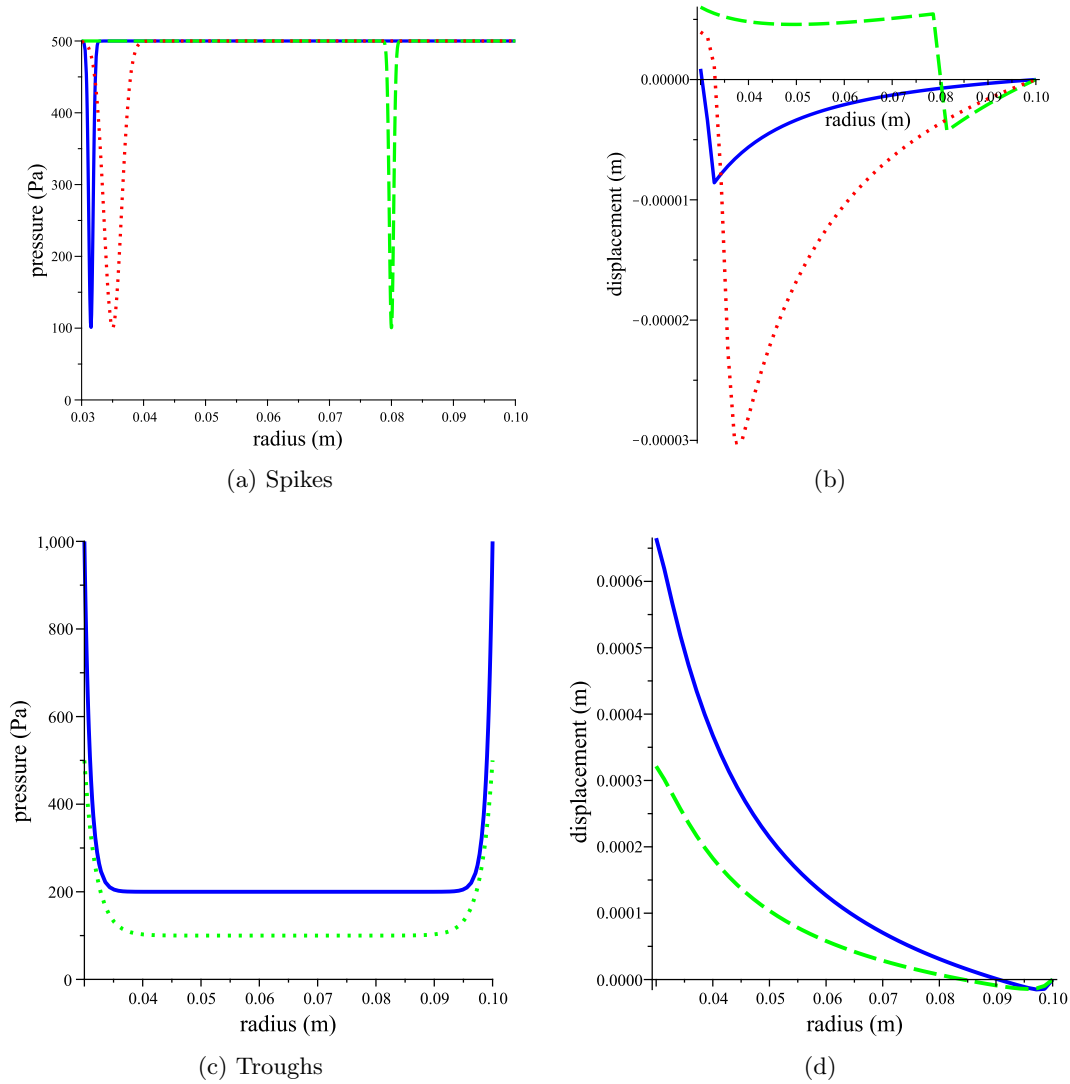
Figure 3: Hypothetical spike (a) and trough (c) pressure profiles and the corresponding displacements, (b) and (d) respectively, obtained from (2.1) with (2.2) and (2.4) ($G = 8$ kPa and $\nu = 0.35$).

Assuming a spherical ventricle, the percentage change in volume due to the trough pressure profiles from Figure 3c are given by the formula:

$$\text{Percentage Change} = 100\frac{\Delta V}{V} = 100\frac{(r + \mathrm{d}r)^3 - r^3}{r^3}.$$

Thus, at the ventricle wall, the percentage increase in volume due to a drop of 400 Pa is 3.2% and the percentage increase in volume due to a drop of 800 Pa is 6.7%, approximately double the increase caused by a 400 Pa drop. These percentages, however, depend on the values of G (8 kPa) and ν (0.35) used in the computation of displacement.

2.4 Discussion. The ventricular enlargements predicted by this model are small compared to the expansion seen in Johnston's animal experiments [4]. There are two possible explanations for this discrepancy. First, the material parameters of the animal brain parenchyma were not known and so rough estimates of the values were used. And second, the expansion seen in the animal experiments occurred over a time scale of two weeks. The displacements predicted by this model are equilibrium solutions, but the time scale on which this occurs is not known and may in fact be quite small depending on the material properties of the parenchyma. Thus, it is possible that large displacements may occur if these pressure distributions reoccur transiently and in response to each transient the parenchyma actively restructures its extracellular environment.

3 The Physical Mechanism - Objective II

To investigate the potential role of anti β_1 integrin antibodies in reducing the interstitial fluid pressure observed in the parenchyma, we hypothesize that the dissociation of the β_1 integrins creates a drop in local parenchymal pressure by changing the mechanical properties of the tissue, such as the elasticity, permeability, and absorption coefficients.

More specifically, the antibodies bind to the β_1 integrins that protrude from cell membranes. Tissue cells are attached to the extracellular matrix (ECM) via integrins, and this forms the tight and rigid matrix structure of the tissue. When the integrins are blocked by the antibodies, the ability of cells to adhere to the ECM is reduced, increasing cell motility and decreasing the rigidity of the tissue structure, see Figure 4. We hypothesize that when cell adhesion decreases, the matrix relaxes slightly which creates a local drop in pressure and reduces the elasticity of the tissue.
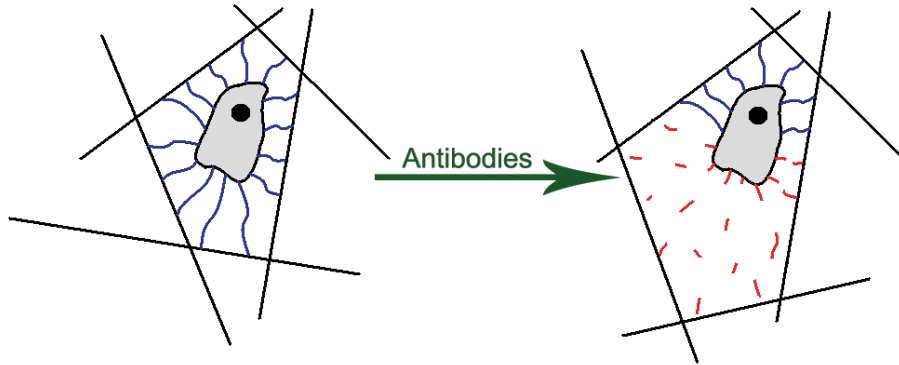
Figure 4: Schematic of the effect of antibodies on the extracellular matrix as cells lose their ability to bind to the matrix.

3.1 Deriving the model. To test this hypothesis, we develop a model on a macroscopic scale that considers the concentration of antibodies in the parenchyma and their overall effect on the tissue mechanics. To account for the flow of CSF (and thus antibodies) through the tissue the theory of linear poroelasticity based on Biot's theory of consolidation [1] is applied to the problem. In the model, material parameters that are assumed to be affected by the β_1 integrin antibodies, such as elasticity and permeability, have spatial and

temporal dependence determined by the antibody concentration history. The concentration of antibodies is governed by a convection-diffusion equation.

Let $\Omega \subset \mathbb{R}^3$ be the domain of the parenchyma, then on Ω conservation of momentum at steady-state, neglecting the inertia terms, gives,

$$\nabla \cdot \tau = 0. \tag{3.1}$$

Here, τ is the total stress tensor and is defined by

$$\tau_{ij} = \sigma_{ij} - p\delta_{ij}, \tag{3.2}$$

where σ is the effective stress tensor and p is the hydrostatic pressure. The effective stress is defined by

$$\sigma_{ij} = \lambda \mathrm{e}_{kk}\delta_{ij} + 2G\mathrm{e}_{ij}, \tag{3.3}$$

where $\lambda = \lambda(\mathbf{x}, t)$ and $G = G(\mathbf{x}, t)$ are the Lamé parameters of elasticity which depend on space and time due to the antibody concentration history through the parenchyma. The strain is assumed linear:

$$\mathrm{e}_{ij} = \frac{1}{2}\left(\nabla \vec{u} + \nabla \vec{u}^{\mathrm{T}}\right), \tag{3.4}$$

with $\vec{u}$ the displacement of the material and $(\cdot)^{\mathrm{T}}$ the transpose operator.

Combining (3.1)–(3.4) gives the following equation of motion:

$$
\begin{aligned}
0 = -\nabla p + (\lambda + G)\nabla(\nabla \cdot \vec{u}) + G\nabla^2 \vec{u} \\
+ (\nabla \cdot \vec{u})\nabla\lambda + (\nabla\vec{u} + \nabla\vec{u}^T) \cdot \nabla G.
\end{aligned} \tag{3.5}
$$

The first line in (3.5) is the standard equation of motion in linear poroelasticity and the second line arises due to the spatial variability of λ and G.

Darcy's law relates the velocity of the fluid through the porous material to the gradient of the pressure:

$$\phi\vec{W} = -k'\nabla p. \tag{3.6}$$

Here, ϕ is the porosity (or the fluid volume fraction which is equivalent in a saturated media), $\vec{W}$ is the filtration of the fluid (defined to be the velocity of the fluid relative to the solid phase), and $k' = k'(\mathbf{x}, t)$ is the hydraulic permeability.

Remark 3.1 In order for CSF pressure to be equal in the ventricle and the subarachnoid space and to be lower inside the parenchyma, an absorption process must occur in the parenchyma to remove the fluid. One possible explanation is that the anti β_1 integrin antibodies degrade the blood brain barrier so that CSF is readily absorbed by the capillaries. This theory, however, is not complete since it only considers hydrostatic pressure gradients as the driving force for CSF into the capillaries.

A more complete explanation for parenchymal absorption is that the antibodies alter the osmotic pressure gradient that exists across capillary walls. By altering the osmotic gradient, CSF can be absorbed into the capillaries even when hydrostatic pressure gradients appear to be inconsistent with such absorption.

Applying conservation of mass to the fluid and solid phases gives

$$\phi_t + \nabla \cdot \left(\phi(\vec{W} + \vec{u}_t)\right) = -Q(\mathbf{x}, t) \quad \text{and} \quad (1 - \phi)_t + \nabla \cdot ((1 - \phi)\vec{u}_t) = 0,$$

where $Q(\mathbf{x}, t)$ represents absorption of CSF by the capillaries (due to osmotic pressure gradients) and depends on space and time due to the antibody concentration. Adding these two equations gives

$$\nabla \cdot (\phi \vec{W} + \vec{u}_t) = -Q(\mathbf{x}, t).$$

Taking the divergence of Darcy's Law (3.6) and substituting into the above equation gives a second equation relating pressure to displacement:

$$\nabla k' \cdot \nabla p + k' \Delta p = \nabla \cdot \vec{u}_t + Q(\mathbf{x}, t). \tag{3.7}$$

Finally, the concentration of antibodies in the parenchyma is governed by the convection-diffusion equation:

$$c_t + \nabla \cdot (c\,(\vec{W} + \vec{u}_t)) = D\Delta c - \alpha c, \tag{3.8}$$

where D is the diffusion constant and α is an absorption constant. The initial condition $c(0) = 0$ is prescribed meaning that for all $\vec{x}$ the antibody concentration is zero at $t = 0$.

The remaining model parameters satisfy the following evolution equations and initial conditions:

$$k'_t = \nu c \qquad\qquad\qquad\qquad k'(0) = \frac{k}{\eta} \tag{3.9}$$

$$\lambda_t = -\gamma H(\lambda - \lambda_{crit})c \qquad\qquad\qquad\qquad \lambda(0) = \lambda_0 \tag{3.10}$$

$$G_t = -\mu H(G - G_{crit})c \qquad\qquad\qquad\qquad G(0) = G_0 \tag{3.11}$$

$$Q_t = \rho H(Q_{crit} - Q)c \qquad\qquad\qquad\qquad Q(0) = Q_0 \tag{3.12}$$

$$\phi_t = -\nabla \cdot \left(\phi(\vec{W} + \vec{u}_t)\right) - Q(\mathbf{x}, t) \qquad\qquad\qquad\qquad \phi(0) = \phi_0 \tag{3.13}$$

where ν, γ, μ, and ρ are positive constants, k is the initial permeability of the parenchyma, η is the viscosity of the CSF, $H(\cdot)$ is the Heaviside function, the subscript $crit$ denotes the critical value (maximum or minimum), and the subscript 0 denotes the initial value.

We assume the same spherical geometry as Figure 1, and thus prescribe boundary conditions at the ventricle boundary, $r = r_i$, and the subarachnoid space boundary, $r = r_o$. The pressure in the parenchyma should equal the pressure in the ventricle, p_i, at $r = r_i$ and it should equal the pressure in the subarachnoid space, p_o, at $r = r_o$, or:

$$p(r_i) = p_i \qquad\qquad \text{and} \qquad\qquad p(r_o) = p_o.$$

Note that for communicating hydrocephalus, p_i should approximately equal p_o.

The boundary condition for displacement arises due to the continuity of stress at each boundary. That is, the effective stress at each boundary is zero:

$$\sigma_{ij}n_j = 0 \quad \text{at } r = r_i \text{ and at } r = r_o.$$

Note that this case represents infant hydrocephalus where the cerebral plates have yet to fuse and so the skull may enlarge. For adult hydrocephalus, where the skull is rigid, the outer boundary condition should be changed to $u(r_o) = 0$.

Finally, the boundary conditions for the concentration of antibodies are:

$$c(r_i) = c_0 \mathrm{e}^{-\theta t} \qquad\qquad \text{and} \qquad\qquad c(r_o) = 0.$$

The inner condition represents an exponentially decaying source of antibodies in the ventricle which approximates the bolus injection draining through the aqueduct. The outer condition represents absorption of the antibodies through the normal CSF absorption mechanisms (arachnoid villi or lymphatic drainage).

3.2 Sensitivity to permeability and absorption. Equations (3.5) and (3.7) are coupled equations for displacement and pressure. By assuming a quasi-static state, $\vec{u}_t = 0$, the equations are decoupled giving a single equation determining the pressure:

$$\nabla k' \cdot \nabla p + k' \Delta p = Q(\mathbf{x}, t). \tag{3.14}$$

The quasi-static state assumes the pressure distribution changes and the solid deforms in response to the pressure change. In reality, the deformation of the solid affects the pressure, but this simplifying assumption is made here to decouple the problem.

An indication of the modelling attempt is obtained by solving (3.14) with prescribed hydraulic permeability and absorption as either constants or linear functions of r. The linear functions used are $k' = 0.05(1 - r)$ and $Q = 800(1 - r)$ and the constants used are $k' = 0.05(1 - 0.2)$ and $Q = 800(1 - 0.2)$ for $0.2 \le r \le 0.8$. These functions and values are not physical and were chosen for simplicity. Figure 5 shows these results.
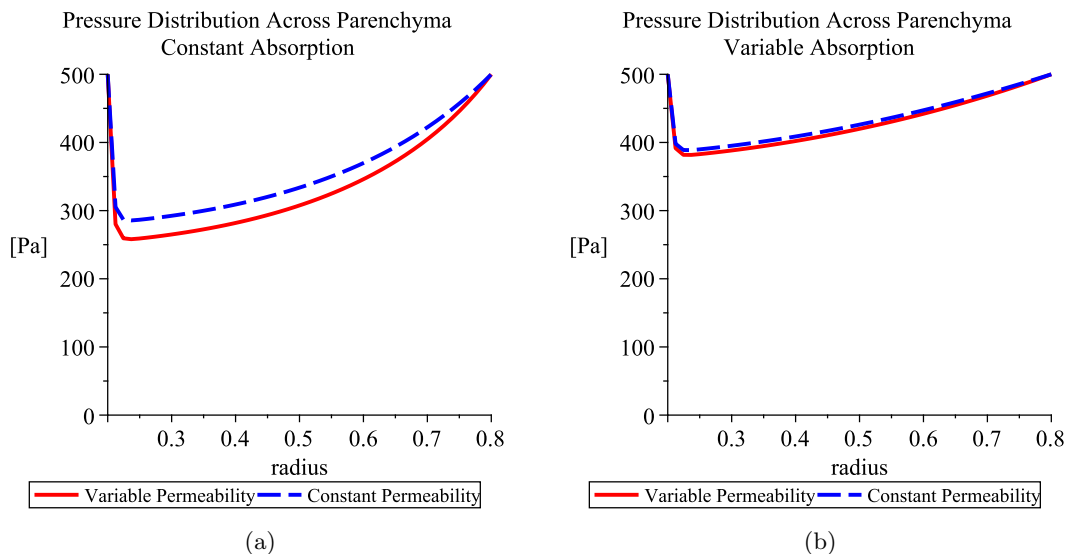
Figure 5: Pressure distributions through the parenchyma assuming constant permeability or variable permeability for either constant absorption (a) or variable absorption (b).

As shown in the simulated pressures in Figure 5, variable permeability slightly lowers the minimum of the pressure curve and absorption strongly affects the shape of the pressure profile. This results from (3.14), since the only solution with $Q(\mathbf{x}, t) = 0$ is $p = p_i = p_o$. Thus, absorption in the parenchyma significantly affects the pressure distribution throughout the brain tissue but permeability does not, so hydraulic permeability, $k'(\mathbf{x}, t)$, may be assumed constant to further simplify the model.

4 Conclusions and Future Work

In working to complete the two objectives outlined in this report, we have identified the pressure distribution throughout the parenchyma and the material parameters of brain tissue as important factors. Future work addressing Objective I would investigate incorporating the compressibility of brain tissue ($\alpha < 1$) into the model and would perform

a sensitivity analysis on how the percentage volume change of the ventricles varies with respect to the model parameters (G and ν in the linear elasticity case as well as k' and $\hat{k}$).

Objective II presents a new model capable of simulating the effect of the antibodies on brain tissue. Future work would include solving the model presented in Section 3.1 and comparing the displacement results to those discussed in Objective I which were obtained from Levine's model [2]. A first approach would be to use the quasi-static state assumption to decouple the model equations for pressure and displacement and to assume constant permeability. A finite element scheme may be necessary to solve the fully coupled model. The large number of model parameters that must be determined from experimental data and the fact that the model is based on linear elasticity are the main limitations of the proposed model.

This preliminary investigation seems to indicate that our assumed mechanical alterations resulting from the injection of anti β_1 integrin antibodies provides the necessary environmental changes in the parenchyma for the pathogenesis of hydrocephalus. A drop in interparenchymal pressure combined with the required increase in CSF absorption by the parenchyma creates the necessary conditions for ventricular enlargement. Add to this, the possibility that antibodies may decrease the elasticity of brain tissue and even more favourable conditions for hydrocephalus are created.

References

1. M.A. Biot, *General theory of three-dimensional consolidation*, J. App. Phys. **12** (1941), no. 2, 155–164.
2. D. N. Levine, *The pathogenesis of normal pressure hydrocephalus: A theoretical analysis*, Bull. Math. Biol. **61** (1999), 875–916.
3. A.A. Linninger, C. Tsakiris, D.C. Zhu, M. Xenos, P. Roycewicz, Z. Danziger, and R. Penn, *Pulsatile cerebrospinal fluid dynamics in the human brain*, IEEE Trans. Biomed. Eng. **52** (2005), no. 4, 557–565.
4. G. Nagra, L. Koh, I. Aubert, M. Kim, and M. Johnston, *Intraventricular injection of antibodies to $\beta1$-integrins generates pressure gradients in the brain favoring hydrocephalus development in rats*, Am. J. Physiol. Regul. Integr. Comp. Physiol. **297** (2009), no. 5, R1312–1321.
5. A. Peña, N.G. Harris, M.D. Bolton, M. Czosnyka, and J.D. Pickard, *Communicating hydrocephalus: the biomechanics of progressive ventricular enlargement revisited*, Acta Neurochir. Suppl. **81** (2002), 59–63.
6. A. Smillie, I. Sobey, and Z. Molnar, *A hydrostatic model of hydrocephalus*, J. Fluid. Mech. **539** (2005), 417–443.
7. G. Tenti, S. Sivaloganathan, and J. M. Drake, *Brain biomechanics: Steady-state consolidation theory of hydrocephalus*, Can. Appl. Math. Q. **7** (1999), no. 1, 93–110.
8. H. Wiig, K. Rubin, and R.K. Reed, *New and active role of the interstitium in control of interstitial fluid pressure: Potential therapeutic consequences*, Acta Anaesthesiol. Scand. **47** (2003), no. 2, 111–121.

Mediators of mechanotransduction between bone cells

Problem Presenter: Svetlana V. Komarova (McGill University)

Contributors: Luciano Buono (UOIT), Svetlana V. Komarova (McGill University), Monserratt Lopez (McGill University), Robert M. Miura (NJIT), Adam Pan (University of Toronto), Mary Pugh (University of Toronto), Sanjive Qazi (Gustavus Adolphus College), David J.N. Wall (University of Canterbury, NZ), Thomas J.W. Wright (Hospital for Sick Children)

Report prepared by[1]**:** S.V. Komarova, M. Lopez, R.M. Miura, S. Qazi, and D.J.N. Wall.

1 Introduction

Mechanical forces are known to regulate the function of tissues in the body, including bone. Bone adapts to its mechanical environment by altering its shape and increasing its size in response to increases in mechanical load associated with exercise, and by decreasing its size in response to decreases in mechanical load associated with microgravity or prolonged bed rest [8]. Changes in bone size and shape are produced by a cooperative action of two main types of the bone cells - osteoclasts that destroy bone and osteoblasts that build bone [7]. These cell types come from different developmental origins, and vary greatly in their characteristics, such as size, shape, and expression of receptor subtypes, which potentially may affect their responses to mechanical stimuli [4]. The objective of this study is to compare the responses of osteoclasts and osteoblasts to mechanical stimulation.

2 Experimental Setup

Bone marrow cells were isolated and plated on a glass-bottom culture dish. The cultures were treated for 4-8 days with ascorbic acid to induce osteoblast differentiation and with RANKL to induce osteoclast differentiation. On the days of the experiments, each dish was first loaded with calcium-sensitive dye fura-2, then the dye was washed out and the dish was placed on the microscope stage. A single cell in the field was identified as an osteoblast or osteoclast based on its morphological features - osteoblasts are small spindle-shaped mononucleated cells and osteoclasts are large cells of 30-60 μm in diameter that contain more than 2 nuclei. Changes in emission at 510 nm following alternating illumination at 340 and 380 nm were recorded, from which cytosolic free calcium concentrations $[\text{Ca}^{2+}]_i$ were later

---

[1]`svetlana.komarova@mcgill.ca, lopezm@physics.mcgill.ca, miura@njit.edu,`
`sqazi@gustavus.edu, d.wall@math.canterbury.ac.nz`

calculated based on a calibration. For each experiment, after 10 s of basal recording, a single osteoclast or osteoblast (primary cell) was gently touched by a micropipette (mechanical stimulation) and changes in $[Ca^{2+}]_i$ in the primary cell as well as other cells in the field (secondary cells) were recorded over 80-120 s. In response to the mechanical stimulation, the primary cell exhibited an increase in $[Ca^{2+}]_i$ that was fast at the onset and then declined relatively slowly. In the neighbouring cells, delayed elevations in $[Ca^{2+}]_i$ were observed consistent with a release of a mediator(s) from a primary cell. To examine if the nature of a mediator can be identified from these experiments, 3 independent recordings with an osteoblast as the primary cell and 5 independent recordings with an osteoclast as the primary cell were analyzed.

3 Analysis and Modelling

3.1 Data analysis of osteoblast and osteoclast recordings. For each experiment, the following information was available:

1. The geographic location of different cells.
2. The temporal dependence of $[Ca^{2+}]_i$ in the primary and secondary responders.

From these data we have assessed the following parameters:

1. The distance R between the centroids of the primary (stimulated) and each of the secondary cells.
2. The time t between the onset of $[Ca^{2+}]_i$ elevation in the primary cell and in each of the secondary responders.
3. The apparent diffusion coefficient (R^2/t) for each secondary responder.
4. The maximum amplitudes of $[Ca^{2+}]_i$ in the primary and secondary responses.
5. The frequency and power of the oscillatory component present in the secondary responders.

Analysis of covariance (ANCOVA) was performed to assess the significance of the distance and the experimental factors on the apparent diffusion coefficient. In the model, the distance factor was the co-variate on the experimental factor, and an interaction term was included to determine if any effect of distance was dependent on the experiment. We log transformed the apparent diffusion coefficient measurement for each cell response to homogenize the group variance and normalize the scatter around the line of best fit. The null hypothesis was that the apparent diffusion coefficient will not be different between experiments and will be consistent for all cell responses for all distances from the source. To test for significance of the departure from the null hypothesis, an F-test with an F-distribution was used to compare statistical models. The probability value P of less than 0.05 was deemed significant [2]. We have found that if the primary cell was an osteoblast, then the three different experiments demonstrated similarity in the apparent diffusion coefficient (R^2/t; ANCOVA, $F_{2,44} = 0.25$, $P = 0.78$). In contrast, the experiments in which an osteoclast was the primary cell demonstrated significant difference in R^2/t between different experiments ($F_{4,22} = 4.25$, $P = 0.011$), while R^2/t remains consistent within experiments (Figure 1A; ANCOVA Interaction term, $F_{4,22} = 1.22$, $P = 0.33$).

We further investigated the dependence of R^2/t on distance from a primary cell, and found that in osteoblast experiments, it positively correlated with the distance (Figure 1B; $F_{1,44} = 8.68$, $P = 0.005$). This dependence was weaker or non-existent in different experiments in which the primary cell was an osteoclast (ANCOVA Distance factor, $F_{1,22} = 0.024$,

$P = 0.88$). We also investigated multiple peaks in $[\mathrm{Ca}^{2+}]_i$ present in a high number of secondary responders. These peaks may result either from internally-driven oscillations or from a superposition of signals from different sources (suggesting that some of the secondary responders may in turn release the mediator). Fourier analysis demonstrated that the period
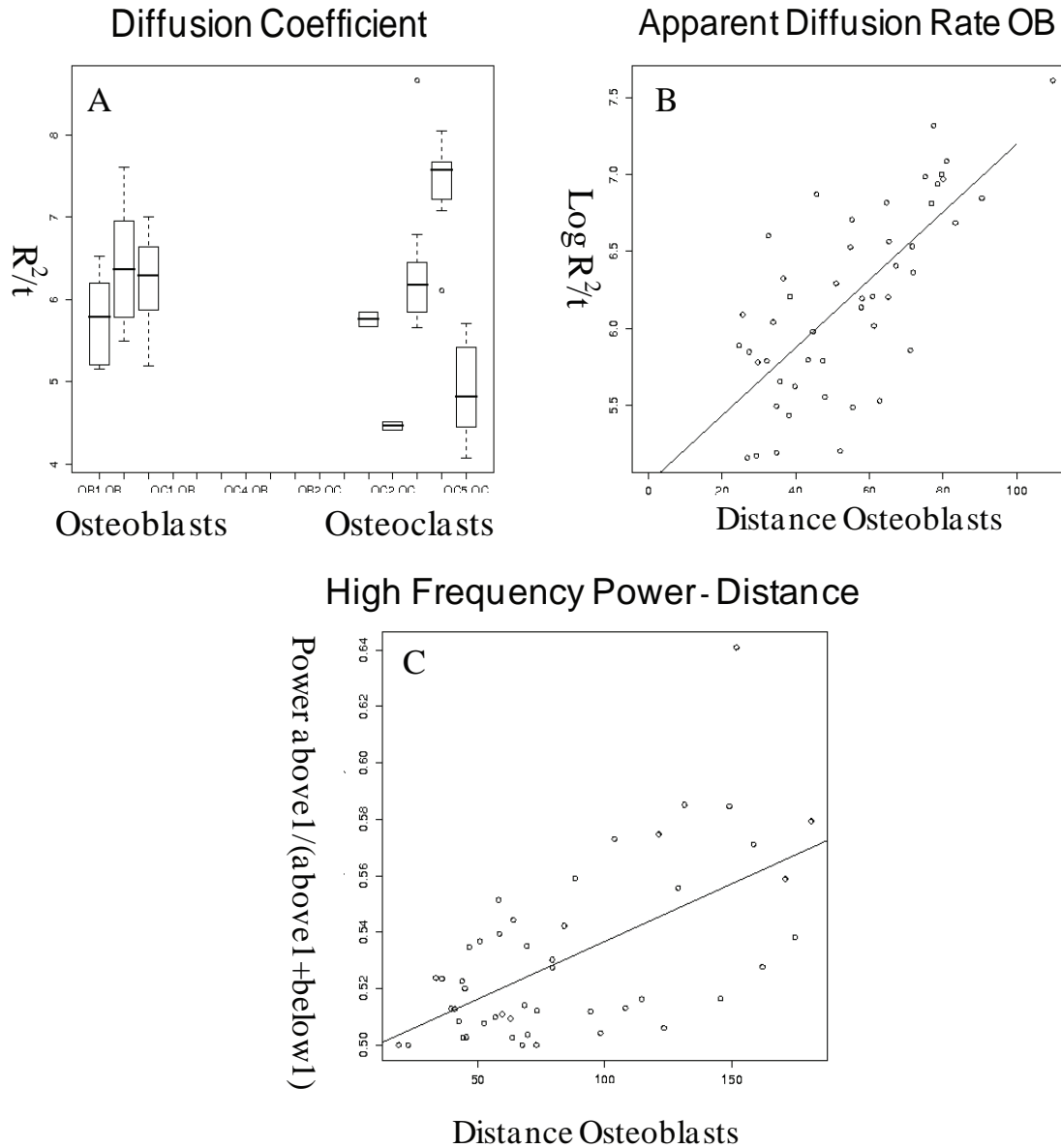
Figure 1 Data analysis of signal propagation initiated by mechanical stimulation. A) An estimate of the diffusion coefficient for 3 experiments in osteoblasts (left) and 5 experiments in osteoclasts (right). B) The relationship between the estimated diffusion coefficient and distance from the primary cell in the 3 osteoblasts experiments. C) The normalized power of the Fourier transform of the oscillatory secondary responses for frequencies above 1Hz.

between the peaks was similar in all of the experimental recordings, strongly supporting the presence of self-sustained oscillations in the secondary responders. In addition, we have found that the probability of observing an oscillatory component increases with the distance from the primary cell (Figure 1C).

Together with the increase in apparent diffusion rate, this allowed us to formulate a hypothesis that a single mediator is released from a primary cell, and subsequently starts to degrade and thus move faster as it travels further away from the source, resulting in a change in the apparent diffusion coefficient as well as the pattern of induced responses. Since a different set of data indicated that ATP is one of the potential mediators of these responses, we conjectured that ATP is released from a source cell and is degraded to ADP by extra-cellular nucleotidases. Whereas ATP mainly acts through P2X ligand gated ion channels, ADP only acts on P2Y G-protein coupled receptors, which accounts for the appearance of oscillations in secondary cells.

3.2 Model for combining ATP degradation and diffusion dynamics. Model assumptions are that:

1. ATP is released by a primary cell and can be degraded to ADP, which in turn degrades to AMP by extracellular nucleotidases.
2. ATP, ADP, and AMP diffuse by radial 2-dimensional diffusion with the diffusion coefficients inversely proportional to the square roots of their molecular weights, respectively.
3. ATP is released in a continuous manner over the duration of an experiment.

Then the chemical reactions are modeled by

$$\frac{\partial a_1}{\partial t} = D_1 \Delta a_1 - k_1 a_1, \tag{3.1}$$

$$\frac{\partial a_2}{\partial t} = D_2 \Delta a_2 + k_1 a_1 - k_2 a_2, \tag{3.2}$$

$$\frac{\partial a_3}{\partial t} = D_3 \Delta a_3 + k_2 a_2 - k_3 a_3, \tag{3.3}$$

where a_1, a_2, a_3 are concentrations of ATP, ADP, and AMP, respectively; D_1, D_2, D_3 are diffusion constants for ATP, ADP, and AMP, respectively [3], k_1 is a rate constant for the ATP to ADP degradation reaction, k_2 is a rate constant for the ADP to AMP degradation reaction, k_3 is a rate constant for the AMP to adenosine degradation reaction, and $\Delta = \partial^2/\partial r^2$. The parameters values were chosen based on the following experimental data: measured ATP diffusion coefficient, $D_1 = 180$ $\mu\text{m}^2/\text{s}$, and estimated rate constants for the ATP to ADP and ADP to AMP reactions given by $k_1 = 0.5$ and $k_2 = 0.4$, respectively [5]. D_2 and D_3 were estimated based on the molecular weights of ATP, ADP, and AMP. We assumed that initially nucleotides are released in proportion to their concentrations in the cell, 100:10:1 for ATP:ADP:AMP [1].

When the simulations were performed for the model describing diffusion of nucleotides only ($k_1 = k_2 = k_3 = 0$), we observed that the main propagating species is ATP (Figure 2A). When we introduced the degradation of ATP to ADP ($k_1 = 0.5$, $k_2 = k_3 = 0$), the balance between the nucleotides changed as they travelled from the source, resulting in ADP becoming the main propagating species at longer distances (Figure 2B). Finally, when we added the degradation of ADP to AMP ($k_1 = 0.5$, $k_2 = 0.4$, $k_3 = 0$), then AMP became the
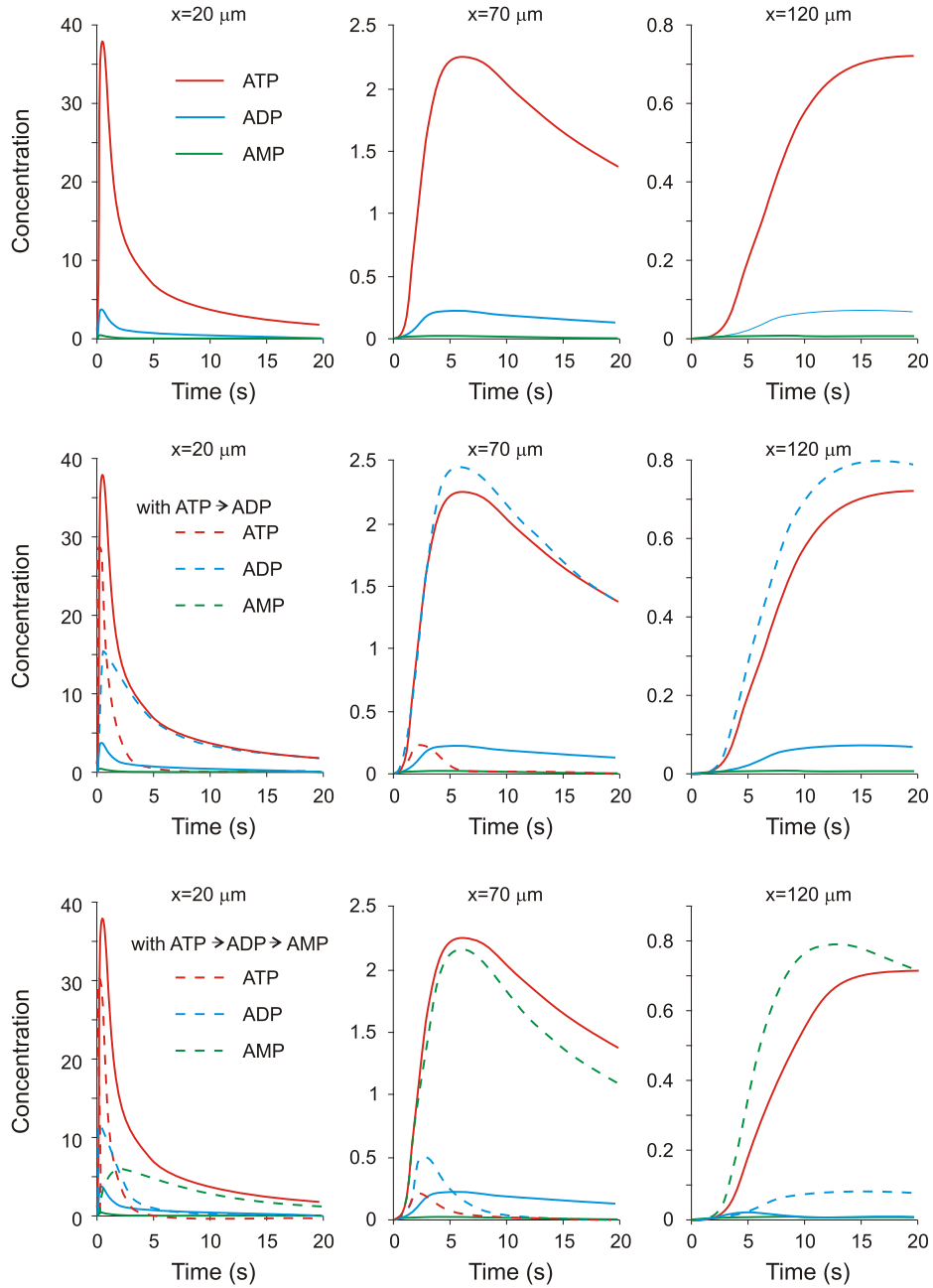
Figure 2 Changes in concentrations of ATP (red), ADP (blue), and AMP (green) at distances of 20 μm (left column), 70 μm (middle column), and 120 μm (right column) from the source, obtained from the model (3.1)-(3.3) describing: A) diffusion only (dashed lines in all figures); B) diffusion of ions and degradation of ATP to ADP; and C) diffusion of ions and degradation of ATP to ADP and ADP to AMP.

main propagating species at longer distances (Figure 2C). Thus, the model predicts that introduction of degradation of ATP to ADP is a plausible explanation for the experimentally observed increase in the value of the apparent diffusion coefficient (Figure 1B).

3.3 Model for osteoclast mediator propagation. To account for the differences observed in different experiments in which an osteoclast was stimulated, we hypothesized that since osteoclasts are vastly different in size, it is possible that the amounts of mediators released in the different experiments are quite different. This would result in significantly different contributions to the reaction time, i.e., the time needed to accumulate the required amount of a signalling molecule on the cell membrane, and to the propagation time in some of the experiments. To assess how large differences in the amount of released mediator may influence the results, the following model was built. The model assumptions are:

1. Only one mediator (with concentration $C = C(r,t)$) is released by a primary cell.
2. The mediator diffuses by 2-dimensional radial diffusion.
3. There is a threshold concentration of a mediator needed to induce a response in a secondary cell. This threshold is the same for all secondary cells.
4. The mechanical stimulation of different cells results in significantly different amounts of the mediator being released.
5. The mediator is released in a continuous manner over the duration of an experiment.

The model is simply the diffusion equation in polar coordinates with no angular dependence given by

$$D \left(\frac{\partial^2 C}{\partial r^2} + \frac{1}{r} \frac{\partial C}{\partial r} \right) - \frac{\partial C}{\partial t} = \frac{C_0}{D} \frac{\delta(r)}{r} H(t) \tag{3.4}$$

where D is the diffusion coefficient, $\delta(r)/r$ is the two-dimensional delta distribution, and $H(t)$ is the Heaviside function. This has the solution

$$C(r,t) = \frac{C_0}{4\pi D} \text{Ei} \left(\frac{-r^2}{4tD} \right) \tag{3.5}$$

where Ei is the exponential integral

$$\text{Ei}(-x) = - \int_x^\infty \frac{e^{-t}}{t} \, dt, \quad x > 0. \tag{3.6}$$

With the substitutions $x = 1/4\pi D$ and $\alpha = r^2/t$, this can be rewritten as:

$$\frac{C}{C_0} = x \text{Ei}(\alpha_{1,2} \pi x) \tag{3.7}$$

where α_1 and α_2 correspond to two values of α in each experiment. From each of two experiments, we then can compute

$$\beta(x) = \frac{C^1}{C^2} = \frac{\text{Ei}(\alpha_1 \pi x)}{\text{Ei}(\alpha_2 \pi x)} \tag{3.8}$$

where C^1 and C^2 correspond to the values of C for α_1 and α_2, respectively. The function $\beta(x)$ is plotted in Figure 3 for different values of D (180 $\mu m^2/s$ for ATP, 210 $\mu m^2/s$ for ADP). The model predicts that if the propagating species is ATP, with diffusion coefficient of 180 $\mu m^2/s$, then two specific ratios of C^1/C^2 will be predicted and observed at the same value of D in the experiments. Since ATP can be experimentally measured [6], the hypothesis can be tested in the future.
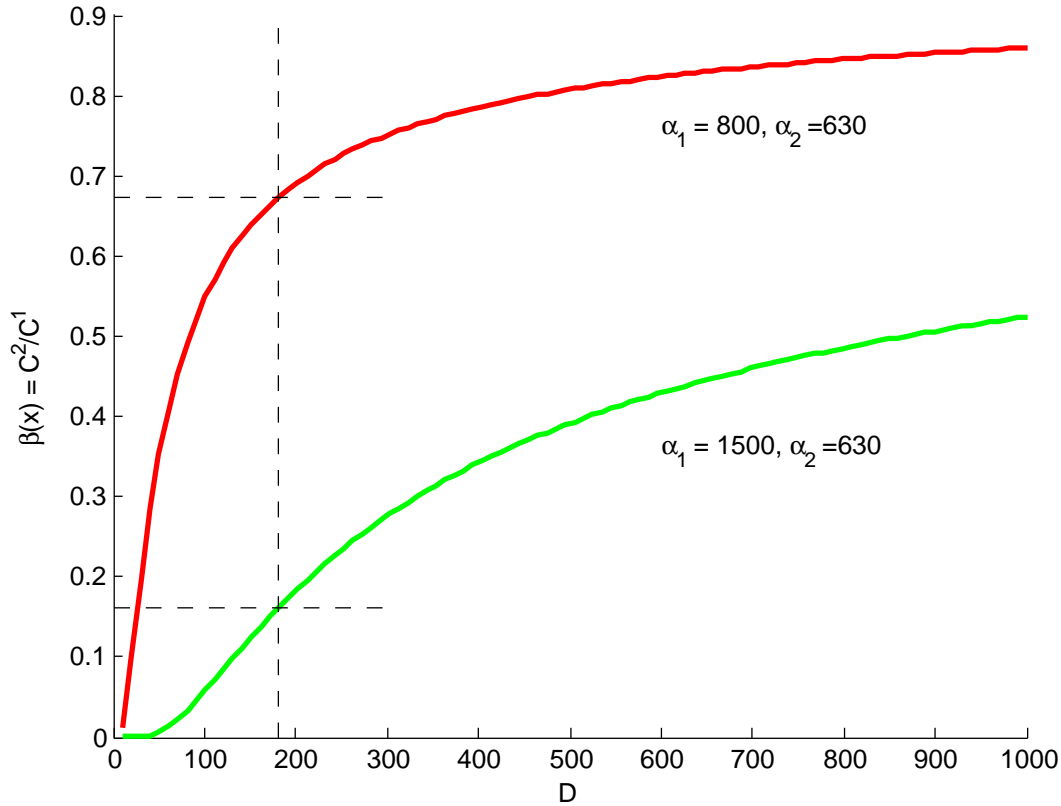
Figure 3 The function $\beta(x)$ is plotted for 2 sets of experiments in each of which α_1 and α_2 were measured. If ATP is the main mediator of the response, then the C^2/C^1 ratio also can be estimated for each experiment and they should intersect the $\beta(x)$ axis at the locations corresponding to the known value for the diffusion coefficient of ATP.

4 Conclusions

This study has allowed us to conclude the following:

1. A mediator is released from a single source cell.
2. The response to the mediator changes with distance.
3. The value of the apparent diffusion coefficient increases with distance.
4. A plausible proposed mechanism is that ATP is released and degrades to ADP.
5. Future experiments are required to confirm that ATP is the mediator as suggested.

References

[1] F.I. Ataullakhanov and V.M. Vitvitsky, *What determines the intracellular ATP concentration*, Biosci. Rep. **22** (2002), no. 5-6, 501–511.

[2] M. Evans, N. Hastings, and B. Peacock, *Statistical Distributions, 3rd Edition*, John Wiley and Sons, 2000.

[3] S.T. Kinsey and T.S. Moerland, *Metabolite diffusion in giant muscle fibers of the spiny lobster Panulirus argus*, J. Exp. Biol. **205** (2002), 3377–3386.

[4] A. Liedert, D. Kaspar, R. Blakytny, L. Claes, and A. Ignatius, *Signal transduction pathways involved in mechanotransduction in bone cells*, BBRC **349** (2006), no. 1, 1–5.

[5] P. Meghji, J.D. Pearson, and L.L. Slakey, *Kinetics of extracellular ATP hydrolysis by microvascular endothelial cells from rat heart*, Biochem J. **308** (1995), 725–731.

[6] I.R. Orriss, G.E. Knight, J.C. Utting, S.E. Taylor, G. Burnstock, and T.R. Arnett, *Hypoxia stimulates vesicular ATP release from rat osteoblasts*, J. Cell Physiol. **220** (2009), no. 1, 155–162.

[7] D. Taylor, J.G. Hazenberg, and T.C. Lee, *Living with cracks: damage and repair in human bone*, Nature Materials **6** (2007), no. 4, 263–268.

[8] C.H. Turner, *Bone strength: current concepts*, Ann. N.Y. Acad. Sci. **1068** (2006), 429–446.

Control of Calcium Carbonate Crystallization by a Serum Protein

Problem Presenter: D. Bassett and J. Barralet (Strathcona Anatomy & Dentistry, McGill University)

Contributors: C.S. Bohun (UOIT), C.J.W. Breward (University of Oxford), H. Huang (York University), M. Morfin (University of Toronto), N. Nigam (McGill University), J. Phillips (McGill University), B. Tilley (Franklin W. Olin College of Engineering), M.J. Tindall (University of Reading), J.A.D. Wattis (University of Nottingham)

Report prepared by[1]: Mario Morfin, C. Sean Bohun, and Jonathan Wattis

Abstract. Calcium carbonate crystals occur in a variety of shapes, each morphology having differing physicochemical properties. This problem involves the formation of calcium carbonate crystals in a gas diffusion process. Experiments showed the formation of clear shapes in the presence of a serum protein. These structures appear to be formed from calcium carbonate fibers arranged in cones, fiber bundles, discs, and other shapes. Some characteristics of the crystals, such as the layering of self similar structures, suggest a process which regulates crystallization. Here we propose a mechanism for the formation of calcium carbonate fibers and their assembly in the complex structures. We describe this process in two systems of partial differential equations. We aim to simulate the growth of these crystals in order to understand the effect of the concentrations and diffusion of the different elements and compounds that are present in the reaction, in the global regulator of the crystallization process.

1 Introduction

Calcium carbonate, $CaCO_3$, is one of the three most common biominerals, the other two being calcium phosphate and silica. When crystallised, $CaCO_3$ forms diverse morphologies with different mechanical, electrical and optical characteristics. This variety of morphologies makes calcium carbonate useful in industry. When biomineralization occurs, various proteins are found in mineralized tissues such as bone, teeth and shells. The presence of these proteins in the biomineralization process is known to effect the characteristics of the final crystal.

The problem posed is to describe the crystallization of calcium carbonate in a gas diffusion process. This process, which will be described in detail below, mimics the biomineralization of $CaCO_3$. It relies on the decomposition of ammonium carbonate to produce carbon dioxide and ammonia gas in a closed environment. The crystallization is achieved via the diffusion of carbon dioxide gas into a solution filled with calcium chloride.

It is well known that, in the absence of other agents, calcium carbonate will crystallize into its most stable form: rhombohedral microcrystals of calcite, see Figure 1 (left). In the experiments presented to the group, an external compound, a serum protein which we denote by P, was introduced to the solution of calcium carbonate. It is known that the serum protein, which is highly phosphorylated, is similar to those found in bone, serum and milk, and inhibits the formation of large calcium carbonate crystals. The aim of the experiment is to explore the effect of the serum protein on the crystallization process.

In the presence of serum protein under the conditions of our experiments, aggregate structures, such as fibres, cones, plate-like floating shapes and fibre bundles, were observed. These structures were formed as calcium carbonate fibre crystals bound together.

The crystals were found in the following configuration: the aggregate structures were formed in the aqueous solution, attached to the surface of the liquid. The cone tips and the binding point of the bundle were also attached to the surface, while the rest of the structure was suspended in the solution. Calcite was formed attached to the bottom of the vessel. Nanofibres were found loose at the bottom of the vessel after drying.
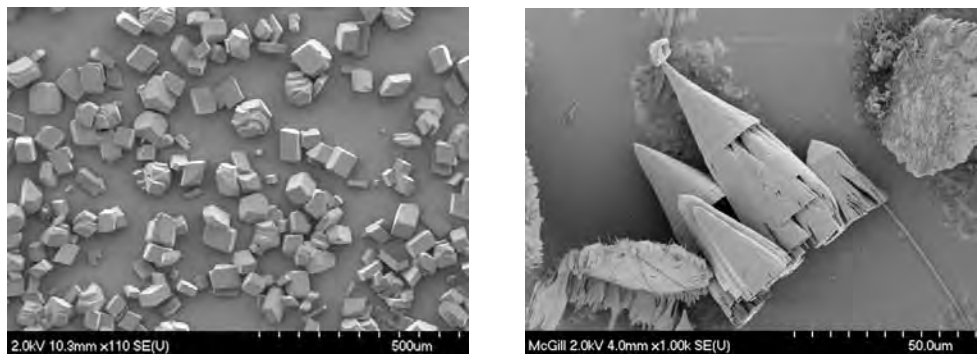
Figure 1 The image to the left shows rhombohedral calcite crystals. The presence of serum protein changes the morphology as illustrated by the image to the right which shows a beautiful set of crystallized cones.

Some global characteristics were observed. For example, in any one experiment, the cone-like shapes appear to be similar, in that they had a similar angle at each apex, even when embedded within each other. The lower boundary of the crystals, i.e. where the crystal stops growing, appear to be constant along separate aggregate structures. (See

Figure 1, right picture and Figure 4, right picture.) This suggests the existence of a global regulatory process.

In the present report, we propose a mechanism for the formation of calcium carbonate fibres and crystals in the complex structures described above. Also, we present two systems of partial differential equations (PDEs) which we use to simulate the growth of these aggregate structures. From the simulations, we attempt to understand the impact of the concentrations and diffusion of the various substances on this regulatory process.

2 The experimental gas-diffusion process

2.1 Methodology. A simple gas diffusion method was used to precipitate calcium carbonate. It was carried out in a closed desiccator at room temperature. The serum protein was dissolved in 100 mM $CaCl_2$ aqueous solution and 1 ml of solution was placed in the reaction vessel. The reaction vessel was then covered with parafilm and punctured six times with a needle. Crushed ammonium carbonate was placed in a dish, covered with parafilm, then punctured in the same way, placed in the bottom of the desiccator. Typically the reaction was allowed to stand for three days, as this was deemed to be when the reaction had reached completion; however, some samples were kept for shorter (one day) and longer (twenty days) times. See Figure 2 for an illustration of the physical setup. Upon completion of the crystallization, the calcium carbonate was removed, dried and examined by X-ray diffraction, scanning and transmission electron microscopy (SEM and TEM).
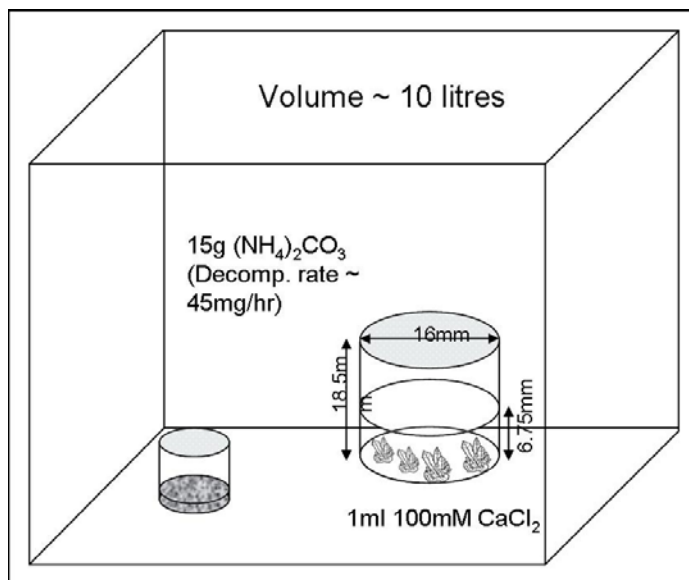

Figure 2 Experimental apparatus for the gas diffusion process.

2.2 Chemical reactions. The ammonium carbonate sublimation chemical reactions are

$$(NH_4)_2CO_{3(s)} \rightleftharpoons NH_{3(g)} + CO_{2(g)} + H_2O_{(g)} \qquad (2.1)$$

$$CO_{2(g)} + H_2O_{(l)} \rightarrow CO_3^{2-} + 2H^+ \qquad (2.2)$$

$$NH_{3(g)} + H_2O_{(l)} \rightarrow NH_4^+ + OH^- \qquad (2.3)$$
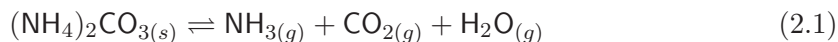
Carbon dioxide was released to the desiccator, and then dissolved in the solution forming dissolved carbon dioxide as well as carbonate ions (CO_3^{2-}) and H_3O^+. According to the diffusion equation, under these experimental conditions, it should take around five hours for these ions to diffuse to the bottom of the vessel. Carbonate ions then react, in the presence of protein, with the Ca^{2+} ions to form $CaCO_3$ in the aqueous solution, according to the reactions

$$CaCl_2 \rightarrow Ca^{2+} + 2Cl^- \tag{2.4}$$

$$Ca^{2+} + CO_3^{2-} \rightleftharpoons CaCO_3. \tag{2.5}$$

The protein is about 200nm long, it has a molecular weight of about 60 kDa, and it is highly phosphorylated. It is amphiphilic since its ends are hydrophobic whilst its centre is slightly hydrophilic. If present at high enough concentration in water, it forms micelles. In the presence of $CaCO_3$, in order to minimise energy, its ends will be in contact with $CaCO_3$ rather than water, thus we might expect the polymer to interact with crystal surfaces once the crystals grow to a large enough size.

2.3 Summary of experimental results. Two types of structures were observed after the crystallization process: nanofibres and aggregated structures (the former appear to be the building blocks of the latter). Nanofibres were between 1 and 2 μm wide, while the size of the aggregated structures were hundreds of times larger (up to 0.5 mm).

At low concentrations of the serum protein (between 0.1 mg/ml and 0.5 mg/ml), only nanofibres were observed. Cones and bundles of fibres were only found at protein concentrations above 1 mg/ml, see Figure 3 (right) and Figure 4 (left and right). At concentrations lower than 0.1 mg/ml, the fibrous structure was lost — see the left panel of Figure 3.
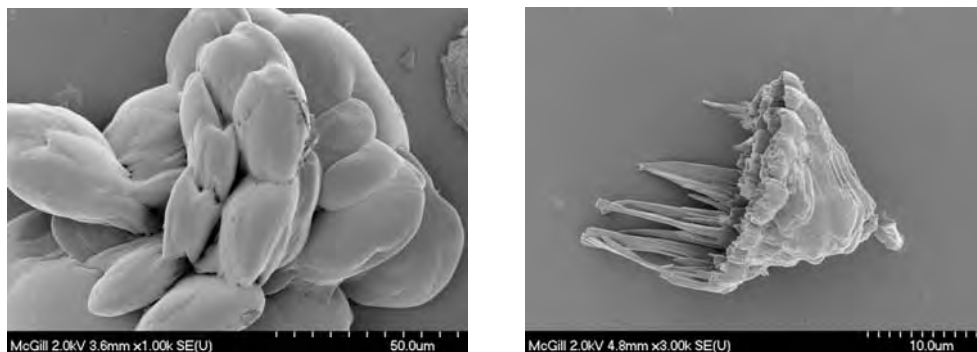
Figure 3 These pictures show the effect of low concentration of protein. On the left, the concentration is lower than 0.1 mg/ml (fibrous structure is lost); on the right, the concentration is 1 mg/ml.

The formation of the nanofibres and the aggregated structures is not simultaneous. It was observed that there are three phases of calcium ion uptake: 6 hours, 36 hours and 72 hours from the start of the reaction. The first detectable structures appear after around fifteen hours. Bundles and cones appear later, in the last phase of the experiment. Also, some calcite was crystallized at the bottom at the earliest stage of the experiment. These crystals were found attached to the vessel. Some nanofibres precipitated to the bottom, unattached to the vessel. (See Figure 4, left picture.) This suggest that the nanoparticles
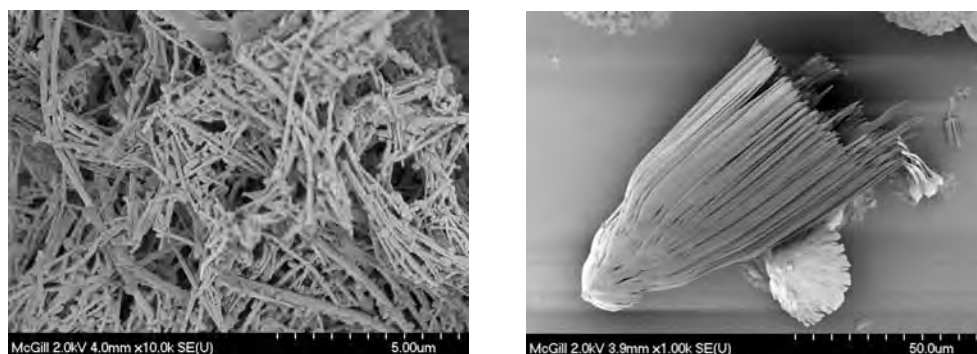
Figure 4 Individual fibres and an example of the bundling of fibres. The concentration of protein is 1 mg/ml.

were formed and assembled in the intermediate phase of the experiment. The remaining fibres fell down after drying.

We visualise cones as hanging vertically downwards from an upper point. The viscosity of the aqueous solution had a role to play as well. If we take a vertical transversal cut of one of the conical shapes, the line that defines the exterior of the crystal will not be straight in general; its concavity depends on the viscosity. Namely, as the viscosity increases, the cones appear to be more 'spread out' and have a larger angle at the tip. The shape of the bundles follows a similar pattern. However, the changes in viscosity did not alter the general shape of the aggregated structures, nor their global behaviours. See Figure 5.
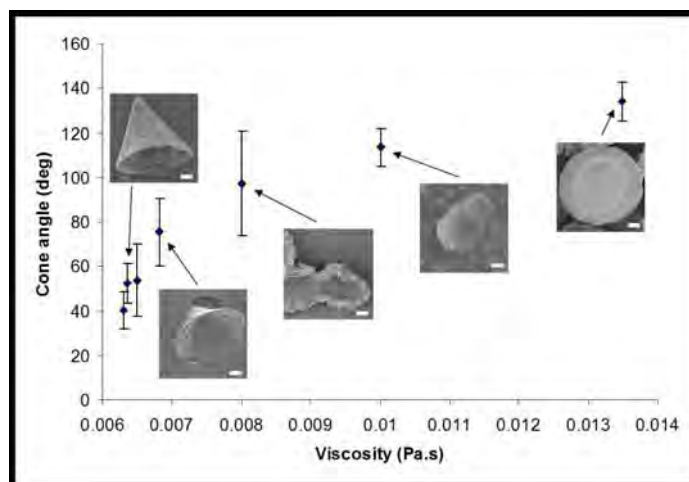
Figure 5 Changes in the opening angle of the fibre cones as a function of the viscosity of the aqueous solution.

The position of the water surface turned out to be important as well. A variation of the standard experiment was done in a very thin pipette, which was small enough that, if turned upside down, the water surface is preserved by surface tension, and the solution does not drop down. Two pipettes with the solution of protein and $CaCl_2$ were placed in the desiccator, one upside down and the other upright. The first did not show growth of crystals, while the other did. Other variations, such as rocking the containers, resulted in

the absence of crystals as well. This could simply be due to the fragility of the crystal structures.

This biomineralization-like process starts out with the diffusion of carbon dioxide into the protein solution. Since no other material is getting in or out the vessel, the time scales of the uptakes of the structures described above imply that they depend only on the concentration of each component. Therefore understanding these concentrations is one of the keys to understanding the interactions with respect to the crystallization process. This aggregation process is independent of the way the nanoparticles and the fibres are bound together.

Based on these observations, many interesting phenomena can be subjected to modeling. For instance, as observed before, The mechanism responsible for the crystallization must be responsible for the banding structure and the way clusters are formed, as well as the assembly of the self-similar structures in layers.

Our objective is to model the formation of calcium carbonate, with and without the protein. Then, considering the appropriate terms in the system, we simulate the uptakes of nanoparticles, the fibres and finally the crystal growth.

3 Mathematical modelling

3.1 Proposed mechanism. In this section, we propose a mechanism for the formation of the crystals. The two systems of PDEs that we present below describe this process. The key stages in the process are as follows:

1. Carbon dioxide dissolves into solution of water with calcium chloride and serum protein.
2. Carbonate ions combine with calcium ions to form calcium carbonate (which is insoluble).
3. Calcium carbonate, in the absence of a serum protein, forms large crystals, that is, the growth of crystals is not limited.
4. Calcium carbonate, in the presence of the serum protein, form nanoparticles. Though we do not model their shape or configuration, it is assumed that their morphology makes the nanoparticles bind into rather large filaments [9, 10]. This indicates some sort of growth-limiting effect of the serum protein.
5. When the concentration of nanoparticles reaches a critical level, they aggregate, or self-assemble, to form fibres. In the experiments, the serum protein was never fully consumed.
6. The fibres assemble to form sheets, bundles and cones. It is not clear whether this occurs after fibre-formation or whether the two processes occur simultaneously.

Our system of equations describes the three time stages of the problem, namely the diffusion of calcium and carbonate ions into the solution, the nucleation and growth of $CaCO_3$ crystals which may occur with interaction with the serum protein and, finally, the arrangement of the nanoparticles into crystallized superstructures.

3.2 Calcium carbonate formation and nanoparticles. We construct a system of PDEs that are one-dimensional in space, with the z-coordinate measuring depth from the top of the vessel; thus $z = 0$ corresponds to the top of the vessel. Here u and v are respectively the concentrations of calcium ions and carbonate ions at depth z and time t.

The initial conditions are as follows: first, there is no flow of any element or compound through the bottom of the vessel $z = L$. In addition, at the top of the vessel, we assume

Table 1 Summary of parameter values.

Parameter	Description	Value
L	Depth of container	6.75 mm
u_0	Initial concentration of calcium in vessel	50 ppm
v_{air}	Carbon dioxide concentration in air above vessel	387 ppm
h	Constant for dissolution of $CO_{2(g)}$	2×10^{-5} $mol\,m^{-2}s^{-1}$
α	Stoichiometic constant for crystal-protein ratio	3
P_0	Initial concentration of serum protein	$1\ mg\,ml^{-1}$
a	Inverse of diameter of nanoparticle X_p	1 nm
k_1	Reaction rate for $Ca+CO_3 \rightarrow CaCO_3$	1×10^{-5}
k_2	Reaction rate for $\alpha X+P \rightarrow X_p$	1×10^{-2}
k_3	Rate of fibre growth in model system 1	1
$\widehat{k_3}$	Rate of fibre growth in model system 2	2×10^{-5}
$\widehat{k_4}$	Rate of sidebranching in model system 2	2×10^{-4}
ε	Rate of new fibre nucleation in model system 2	2×10^{-3}
D_1	Diffusion constant for calcium ions, u	2 cm^2s^{-1}
D_2	Diffusion constant for carbonate ions, v	2 cm^2s^{-1}
D_4	Diffusion constant for microcrystals, X	1 cm^2s^{-1}
D_5	Diffusion constant for nanoparticles, X_p	1 cm^2s^{-1}

a Robin condition for the diffusion of $CO_{2(g)}$, with no carbon dioxide in the solution at time $t = 0$ and a positive atmospheric concentration, v_{air}. We will also assume uniform concentrations of calcium and protein initially in the solution. Hence we have

$$u(z,0) = u_0, \qquad u_z(0,t) = 0, \qquad v_z(0,t) = h(v_{air} - v(0,t)), \qquad (3.1)$$

$$v(z,0) = 0, \qquad u_z(L,t) = 0, \qquad v_z(L,t) = 0 \qquad (3.2)$$

with the constant of dissolution of $CO_{2(g)}$ given in Table 1.

We apply the law of mass action to the governing chemical equations (2.5), which can be written chemically as $u + v \xrightarrow{k_1} X$, to obtain the following system of coupled non-linear equations

$$\frac{\partial u}{\partial t} = D_1\frac{\partial^2 u}{\partial z^2} - k_1 uv, \qquad\qquad \frac{\partial v}{\partial t} = D_2\frac{\partial^2 v}{\partial z^2} - k_1 uv, \qquad (3.3)$$

where D_1 and D_2 are the diffusion coefficients for calcium and carbonate ions respectively, and k_1 is the reaction term for the calcium and carbonate ions to combine and form the insoluble crystal, X, whose concentration we denote by $X(z,t)$.

Denoting the protein concentration by $P(z,t)$, the boundary and initial conditions for X and P describe the fact that neither can escape from the top or bottom of the reaction vessel. Whilst there is no crystal present at $t = 0$, the protein is present, at some concentration, P_0 distributed uniformly, hence we have

$$X_z(0,t) = 0, \qquad X_z(L,t) = 0, \qquad X(z,0) = 0, \qquad (3.4)$$

$$P_z(0,t) = 0, \qquad P_z(L,t) = 0, \qquad P(z,0) = P_0. \qquad (3.5)$$

The second set of PDEs describe the formation of $CaCO_3$ when they interact with the serum protein, which is present at concentration $P(z,t)$. The chemical model we wish to describe

is $\alpha X + P \xrightarrow{k_2} X_p$, where X_p denotes a nanocrystal of calcium carbonate which is large enough to have adsorbed at least one protein molecule onto its surface. Hence,

$$\frac{\partial P}{\partial t} = D_3 \frac{\partial^2 P}{\partial z^2} - k_2 X^\alpha P, \qquad\qquad \frac{\partial X}{\partial t} = D_4 \frac{\partial^2 X}{\partial z^2} - k_2 X^\alpha P + k_1 uv, \qquad (3.6)$$

where D_3 and D_4 are the diffusion coefficients, k_2 is the combined reaction term for the nucleation and growth of a calcium carbonate crystal and its subsequent combining with protein. Rather than go to the complexity of modelling clusters of the full range of sizes, we go straight to an approximation in which many particles are assumed to interact to form a much larger complicated structure. This can be derived in a more rigorous fashion, as analysed in other work [3, 5], and has been used successfully in a number of applications from surfactant flow [1, 2] to other models of nucleation, competition and inhibition [4, 11].

The third part of the model has been approached in two different ways, these are presented in the next two subsections. The first model's growth occurs only at the tips, whilst the second takes into account the possibility that fibres may branch as they grow, giving rise to triangular surfaces.

3.3 Formation of fibre nanocrystals and fibres: system 1. We assume that fibres are initiated at the top surface and grow vertically downwards, so a fibre of length q ends at a depth $z = q$. Let X_p be the concentration of nanoparticles and $Y(z,t)$ the number of fibres of length z ending at depth z at time t. We assume that nanoparticles can move by diffusion, but that fibres are fixed. Nanoparticles are created by the process $\alpha X + P \xrightarrow{k_2} X_p$ discussed above, hence X_p is determined by an equation similar to (3.6):

$$\frac{\partial X_p}{\partial t} = D_5 \frac{\partial^2 X_p}{\partial z^2} + k_2 X^\alpha P - k_3 a X_p Y, \qquad (3.7)$$

where D_5 is the diffusion coefficient of the nanoparticles X_p, k_2 is as before, and k_3 is the reaction term for the nanoparticles and calcium carbonate fibres. The derivation of an equation for $Y(z,t)$ is more complex.

The quantity $Y(z,t)$ can only change if there are fibres that end at $z - \delta$ (for some small $\delta \ll 1$). Because fibres grow downwards, we must have $Y(z - \delta) > Y(z)$. In a discrete approximation to the system, we let $Y(n\Delta z, k\Delta t)$ be the number of fibres of length $n\Delta z$ at time $k\Delta t$. In the next time interval, a particle X_p will be added with probability which depends linearly on the concentration X_p, hence we denote this probability by pX_p. Incorporation of tips of length $n\Delta z$ is done at the expense of tips located at $(n-1)\Delta z$. Thus we have

$$Y(n\Delta z, (k+1)\Delta t) = Y(n\Delta z, k\Delta t) - pX_p Y(n\Delta z, k\Delta t) + pX_p Y((n-1)\Delta z, k\Delta t). \qquad (3.8)$$

Taking the limits $\Delta z \to 0$, $\Delta t \to 0$ with $\Delta z \sim \Delta t$, and defining $k_3 = p \lim_{\Delta t \to 0}(\Delta z/\Delta t)$, we obtain

$$\frac{\partial Y}{\partial t} = -k_3 X_p \frac{\partial Y}{\partial z}. \qquad (3.9)$$

Hence fibres grow at the rate $k_3 X_p$, with k_3 having units of $[k_3] =$ length per concentration per time. For (3.7) we require the units of $k_3 a X_p Y$ to match that of $\partial X_p/\partial t$. Therefore the units of the constant 'a' must be inverse length. In fact $1/a$ can be thought to correspond to the diameter of an X_p nanoparticle.

In this system, fibres grow only at the tip, that is, there is no side-branching. In this formulation, k_3 is the reaction term for the nanoparticles and the tips' aggregated structure.

3.4 Formation of fibre nanocrystals and fibres: system 2. In this formulation, as well as fibres growing from the surface downwards with growth only occurring at their lower ends, we permit the formation of new fibres anywhere in the vessel where there are sufficient nanoparticles (X_p), and we allow growing fibres to sidebranch, so that the aggregated structures become wider at the bottom than the top.

Let $X_p(z,t)$ be as before, but now $Y(z,t)$ is the *mass* of fibres at depth z; we assume that two nanoparticles colliding can initiate the growth of a new fibre – which will be a small effect, hence the rate constant is taken to be ε. More important is the extensional growth of existing fibres, which occurs with a rate constant $\widehat{k}_3$ ($[\widehat{k}_3]$ = length per concentration per time) and the side-branching which occurs at a rate $\widehat{k}_4$ ($[\widehat{k}_4]$ = per concentration per time). Side-branching causes the crystals to become wider further down the vessel. In accordance with (3.7) and (3.9) one has in this case

$$\frac{\partial X_p}{\partial t} = D_5 \frac{\partial^2 X_p}{\partial z^2} + k_2 X^\alpha P - \widehat{k}_3 a X_p Y - \varepsilon X_p^2 - \widehat{k}_4 X_p Y, \qquad (3.10)$$

$$\frac{\partial Y}{\partial t} = -\widehat{k}_3 X_p \frac{\partial Y}{\partial z} + \varepsilon X_p^2 - \widehat{k}_4 X_p Y, \qquad (3.11)$$

where the first term of the latter equation stands, as before, for the growth of the fibres. Typically we expect $\varepsilon < \widehat{k}_4 < \widehat{k}_3 a$. The boundary conditions for (3.10)–(3.11) are all zero flux and the initial conditions are also zero, namely

$$X_{p,z}(0,t) = 0, \qquad X_{p,z}(L,t) = 0, \qquad X_p(z,0) = 0, \qquad (3.12)$$

$$Y_z(0,t) = 0, \qquad Y_z(L,t) = 0, \qquad Y(z,0) = 0. \qquad (3.13)$$

3.5 Diffusion constants and other observations. Now we face the problem of estimating the constants for the various processes. These rates are known for the formation of calcium carbonate in alkaline environments, but not for environments where the serum protein is present; in these cases they have to be inferred. Rate constants are extracted from time dependent concentration profiles determined from experiment. Such profiles are depicted in Figure 6.

In the case of α, we set a value of 3, instead of 300, since for large α the equations become too stiff for the numerical method used. However, we can infer the results for large α. This will be detailed below. We also estimated the rest of the unknown coefficients, using similar principles.

4 Results

The systems of PDEs were solved using MatLab 7.5. The graphs below show the concentration of each component in the time-space phase plane. The color scale goes from blue to red, where blue signifies the absence of the component, and red the highest concentration.

4.1 Formation of fibre nanocrystals and fibres: system 1. Here we solve equations (3.1)–(3.9). First we present the solution of the system in the absence of protein, see Figure 7. The concentrations of calcium, carbonate ions, and calcium carbonate crystals conform to experimental observation. That is, nearly uniform production of calcium carbonate microcrystals with carbonate diffusing into solution from the position $z = 0$. We now compare Figures 7 and 8, the latter having protein in the solution. In both cases, the concentration of calcium decays through the experiment but is always nearly uniform through the vessel, the concentration of carbonate starts at zero and increases, initially
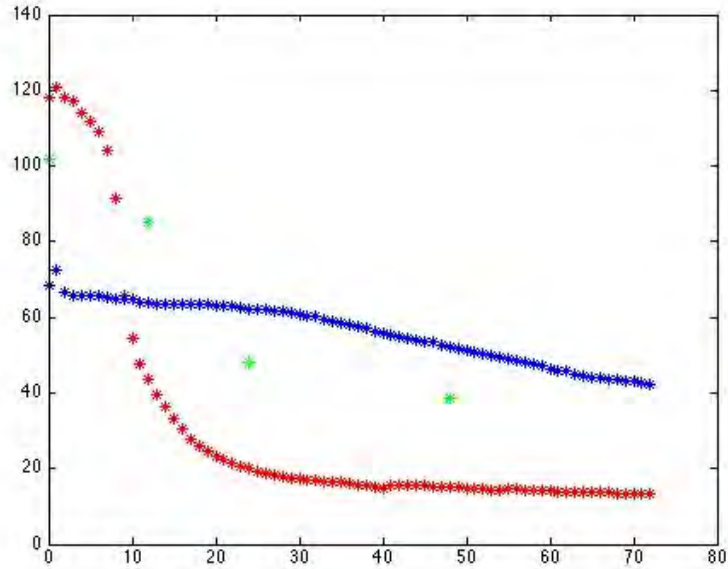
Figure 6 This graph shows the concentration of Ca^{2+} in the solution plotted against time for the cases with (red) and without (blue) protein. Without protein the concentration falls very slowly whereas with protein there is a significant decrease at about $t = 10$. The green data points are more careful measurements which compensate for the build up of $CaCO_3$ on the probes. These values are acquired less frequently (isolated data at $t = 10, 25, 50$).

from the top of the vessel, and always has a significant gradient from top to bottom of the vessel. The concentration of calcium carbonate has similar behaviour, although with a less pronounced gradient.

In Figure 8, we see the concentration of nanocrystals, fibres and the consumption of the protein in accordance with the first system of PDEs, where the initial concentration of the protein is not zero. In this simulation, the protein is consumed uniformly, but the nanocrystals at the top of the vessel are used first in the assembly of aggregated structures (fibres). In this case the assembly of nanocrystals into fibres occurs so rapidly that we see the formation of fibres from the top of the vessel, and never observe any significant concentration of nanocrystals, except for midway through the simulation when there is a small concentration at the bottom of the vessel. They cannot attach to fibres, because at this point in the simulation there are only fibres at the top of the vessel. Note that fibres grow monotonically.

Now we test the results of the simulation by varying the concentration of protein, and find results consistent with the experimental observations described above. At lower protein concentrations, it will take longer for the crystals (X) to interact with protein forming the nanoparticles X_p. Hence the formation of fibres would also be delayed; see Figure 9 top. An additional process in the experiment which has yet to be built into our models is that the crystals would grow larger before having their growth inhibited by the protein, and hence there would be fewer, but larger nanoparticles to form the fibres. On the other hand, if the
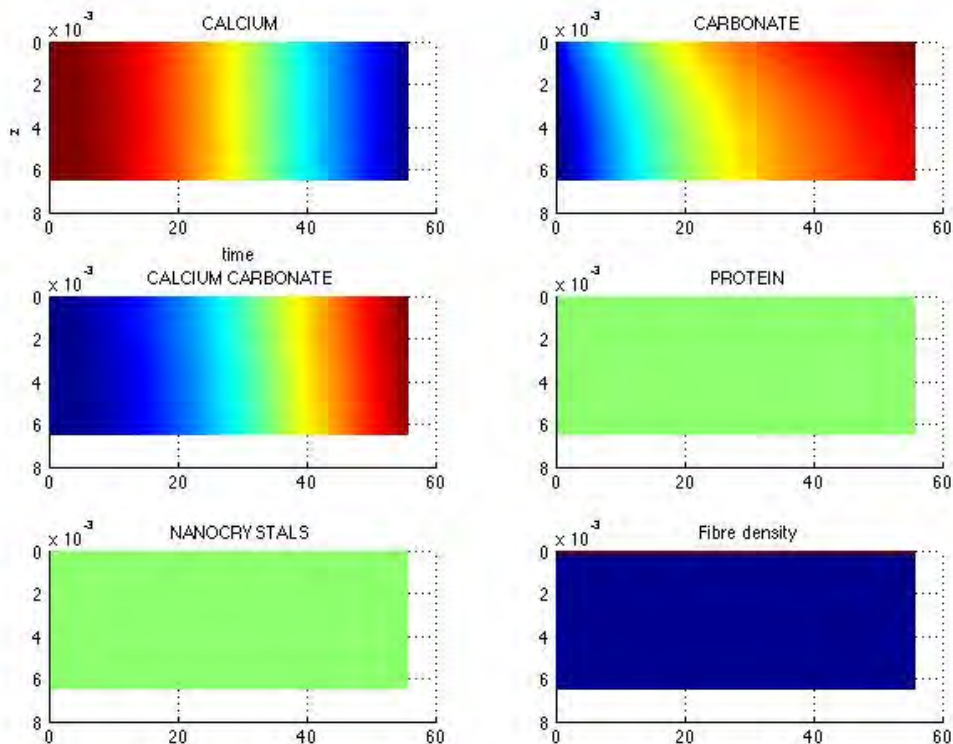
Figure 7 Solution of (3.1)–(3.9) without the addition of any protein. In this situation calcium chloride forms throughout the length $0 < z < L$.

concentration of protein is higher, the increase in fibre density occurs sooner, due to the more rapid formation of the X_p nanoparticles; see Figure 9 bottom.

As pointed out above, we have set α to 3, instead of 300, since for large α the equations become too stiff for the numerical method used. This parameter, determines the size of the nanoparticle. If its value increases, more calcium carbonate would be needed to form the aggregated structures. However, the global behaviour of the system would remain unaffected, and differences in timescales caused by changing α can be compensated for by simultaneously changing k_2.

4.2 Formation of fibre nanocrystals and fibres: system 2. Here we solve equations (3.1)–(3.6) and (3.10)-(3.13). Considering the possibility of branching allows us to describe other characteristics that we could not see using the first system. For a small amount of side branching the concentration profiles of the various species are not suprisingly quite similar to Figure 8 and are omitted for brevity. When nucleation of new fibres is significant in the model, we obtain a much clearer front in the formation of fibres as evidenced in Figure 10.

4.3 Effect of variations in viscosity. Recall that the viscosity of the aqueous solution did not alter the growth of the fibres, but did change the shape of the conical aggregate
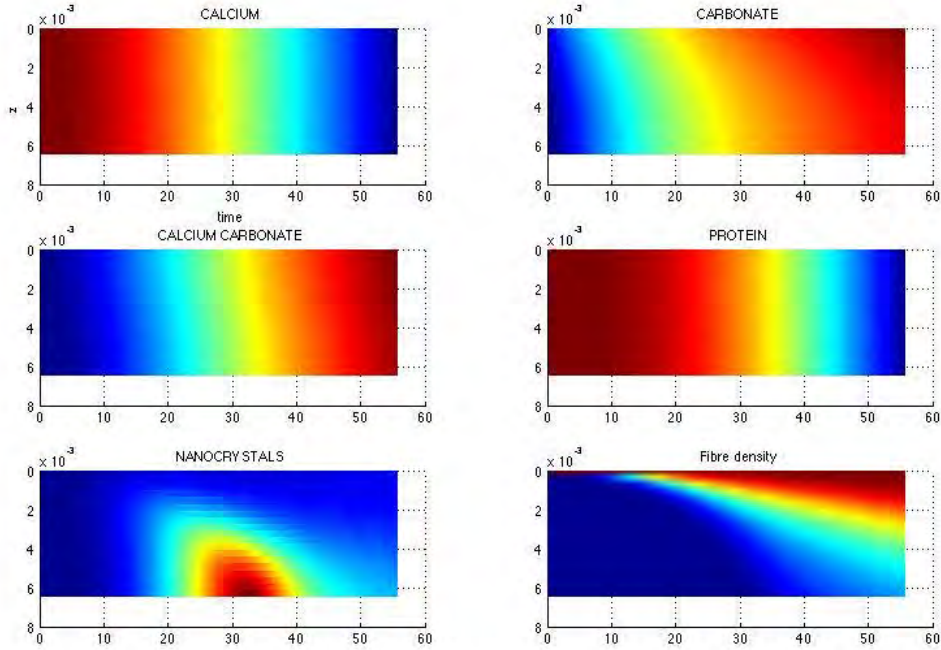
Figure 8 Solution of (3.1)–(3.9) with the addition of a small amount of serum protein.
Notice that the protein depletes uniformly in space. Nanocrystals form throughout but
are incorporated into fibres starting at the top of the vessel.

(which we are not concerned with in this model). Since our model has no viscosity param-
eter, we model the change by changing the diffusion constants, and noting that these are
given by $D = k_B T / 6\pi a \eta$, where k_B is Boltzmann's constant, T is temperature, a is the ra-
dius of the diffusing particle and η is the viscosity. Hence a doubling viscosity corresponds
to reducing all the diffusion constants by a factor of two. Changing the viscosity had no
appreciable effect for system 1 or system 2 with small side branching. However for system 2
with significant side branching, the crystallization front of both the nanoparticles and fibres
is smoothed out by this change in viscosity; see Figure 11.

5 Discussion

We have formulated a model for the concentrations of the various species of ion, protein,
microcrystals, and larger scale crystal complexes present in the system as a function of depth
in the vessel, which describes their variation through the time course of the experiment. The
models have the form of a coupled system of partial differential equations with parameters
which we have derived from crude calculations based on experimental data. The ordering
of events, and predicted form of the solution matches well with the observed data, although
the model lacks the spatial resolution to describe the precise geometry of structures formed.
We speculate that this structure may be related to the properties of the actual molecular
level details of the protein present in solution.
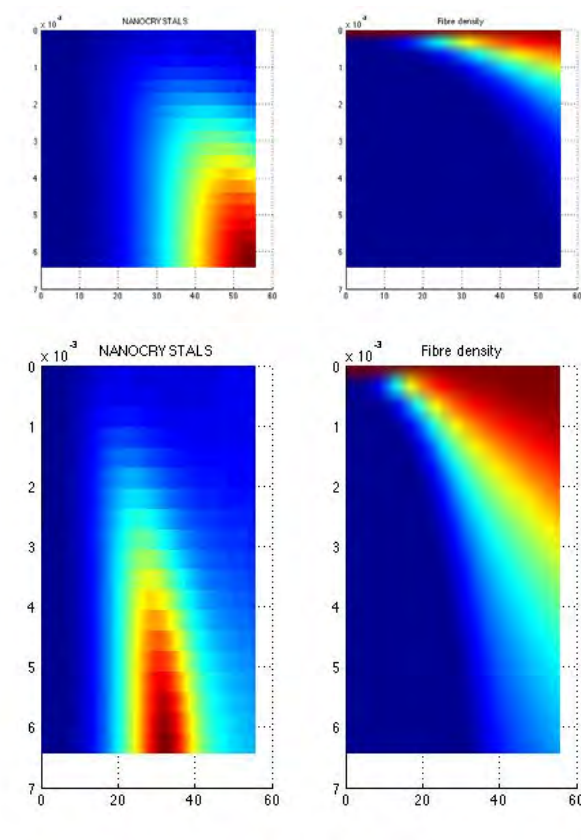
Figure 9 The effect of varying the initial protein concentration. Above the initial protein is 0.5 units, and below the initial protein is 2 units. Compare these with Figure 8, where the concentration is 1 unit.

We predict the presence of a diffusive wave of calcium carbonate which travels down through the reaction vessel. Serum protein interacts with these particles to form microcrystals coated in protein that then self-assemble into bundles of fibres which occasionally undergo side-branching. Side-branching forces the growing surface to become wider the further down the vessel it grows, causing an inverted cone-shaped structure to form.

Our model does not capture the geometry of the described aggregation phenomena beyond the fibres; namely, the ensemble of bundles and cones is not described. However, we can derive some conjectures that are consistent with the models described above, and the experimental data. For instance, at moderate concentrations of protein, fibres should grow in bundles, with a distribution of lengths. At intermediate concentrations, the fibres should grow to a length where secondary effects (competition of nucleation vs. increasing electrostatic energy) inhibit further growth. Under these conditions, cones will appear. Finally, for large concentrations of protein, nucleation should proceed on the inner surfaces of cones, and banding should appear. There are thus many questions which this report leaves open for further study.
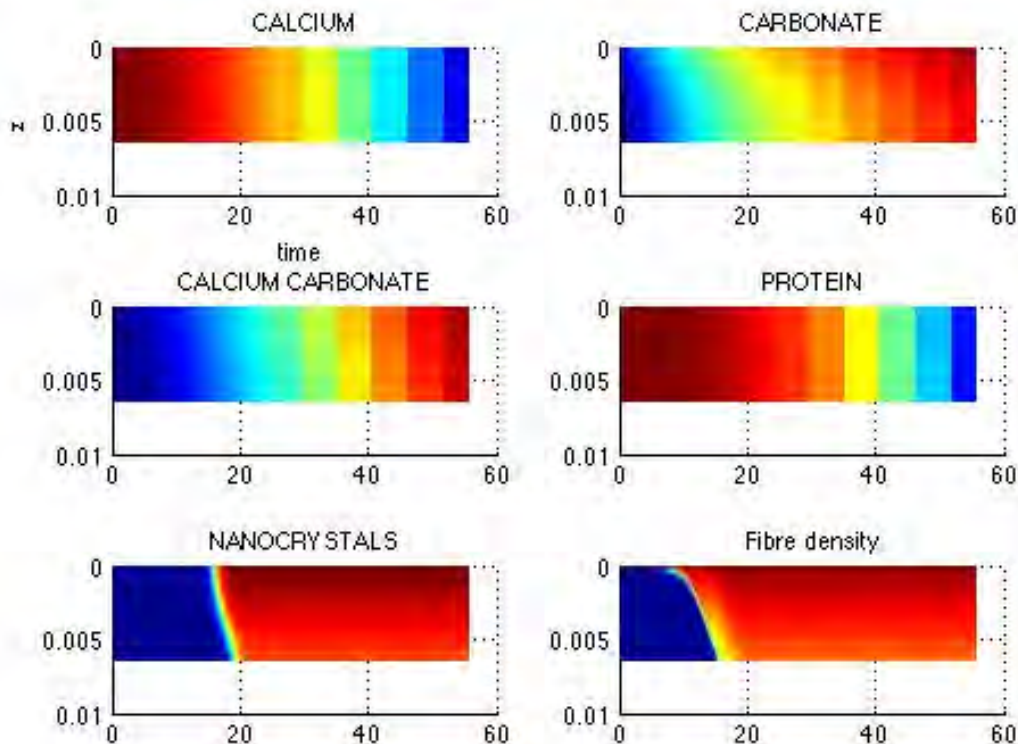
Figure 10 Solution to (3.1)–(3.6) and (3.10)-(3.13) when there is a significant amount of side branching. Compare to Figure 8 where no side branching occurs.

References

[1] C.G. Bell, C.J.W. Breward, P.D. Howell, J. Penfold and R.K. Thomas, *Macroscopic modeling of the surface tension of polymer–surfactant systems*, Langmuir **23** (2006), 6042–6052.

[2] C.J.W. Breward and P.D. Howell, *Straining flow of a micellar surfactant solution*, Euro. J. Appl. Math. **15** (2004), 511–531.

[3] C.D. Bolton and J.A.D. Wattis, *Generalised coarse-grained Becker-Doring equations*, J. Phys. A: Math. Gen. **36** (2003), 7859–7888.

[4] C.D. Bolton and J.A.D. Wattis, *The Becker-Doring equations with input, competition and inhibition*, J. Phys. A: Math. Gen. **37** (2004), 1971–1986.

[5] P.V. Coveney and J.A.D. Wattis, *Analysis of a generalized Becker-Döring model of self-reproducing micelles*, Proc. Roy. Soc. Lond. A **452** (1996), 2079–2102.

[6] S. Hayashi, K. Ohkawa, Y. Suwa, T. Sugawara, T. Asami and H. Yamamoto, *Fibrous and helical calcite crystals induced by synthetic polypeptides containing O-phospho-L-serine and O-phospho-L-threonine*, Macromolecular Bioscience **8** (2008), 46–59.

[7] X. Liu, B. Liu, Z. Wang, B. Zhang, and Z. Zhang, *Oriented vaterite $CaCO_3$ tablet-like arrays mineralized at air/water interface through cooperative regulation of polypeptide and double hydrophilic block copolymer*, J. Phys. Chem. C **112** (2008), 9632–9636.

[8] T. Somasundaram, M. in het Panhuis, and R.M. Lynden-Bell, *A simulation study of the kinetics of passage of CO_2 and N_2 through the liquid/vapor interface of water*, J. Chem. Phys. **111** (1999), 2190–2199.
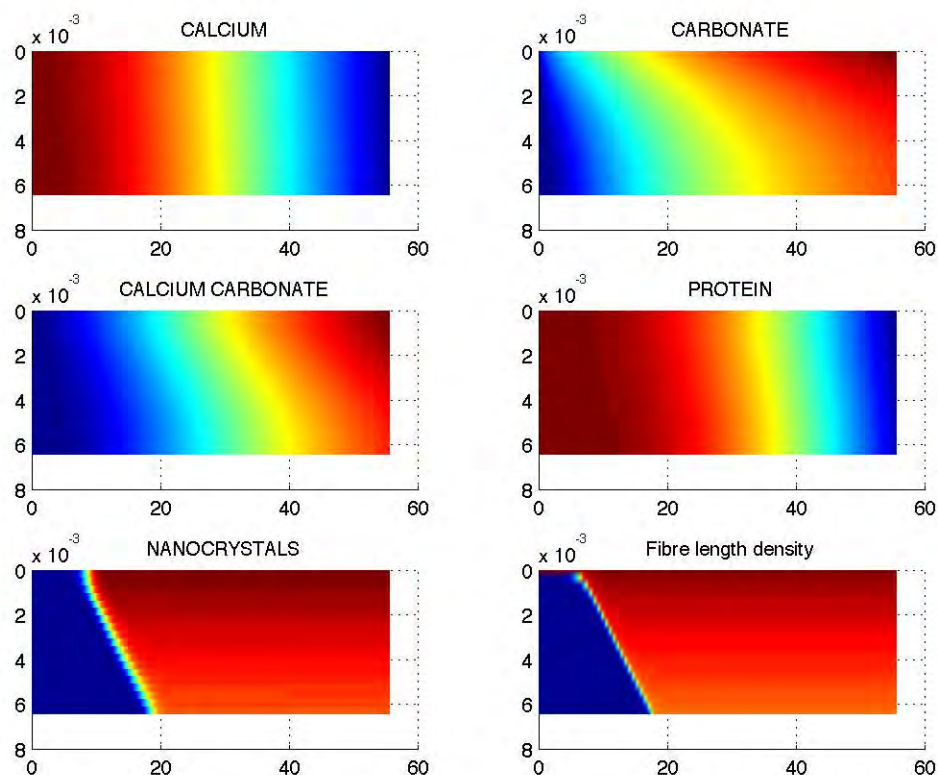
Figure 11 Solution to (3.1)–(3.6) and (3.10)-(3.13) with a solution of twice the viscosity which is simulated by halving all of the diffusion coefficients. The smoothing out of the crystallization fronts is evident when compared to Figure 10.

[9] T. Wangu, A. Reinecke, and H. Cölfen, *In situ investigation of complex $BaSO_4$ fiber generation in the presence of sodium polyacrylate. 2. crystallization mechanisms*, Langmuir **22** (2006), 8986–8994.

[10] T. Wangu and H. Cölfen, *In Situ investigation of complex $BaSO_4$ fiber generation in the presence of sodium polyacrylate. 1. kinetics and solution analysis*, Langmuir **22** (2006), 8975–8985.

[11] J.A.D. Wattis and P.V. Coveney, *Generalised nucleation theory with inhibition for chemically reacting systems*, J. Chem. Phys. **106** (1997), 9122–9140.

Sodium Flux during Haemodialysis

Problem Presenter: Dr. Sushrat Waikar (Brigham and Women's Hospital, Boston, MA and Harvard Medical School).

Contributors: C. Sean Bohun (UOIT), Chris Breward (Oxford), Radina Droumeva (SFU), Ian Griffiths (Oxford), Matt Hennessy (UOIT), Huaxiong Huang (York), Matt Kloosterman (UOIT), Adam Pan (Toronto), Chris Raymond (Delaware), Don Schwendeman (RPI), Jennifer Siggers (Imperial College London), B.S. Tilley (Olin College of Engineering), Marcus Tindall (University of Reading), Jonathan Wattis (University of Nottingham), Jonathan Whiteley (Oxford), Robert Whittaker (Oxford), JF Williams (SFU)

Report prepared by: B.S. Tilley[1]

Abstract. Dialysis is aimed at the removal of charged ionic species in the blood that arise from complications in kidney disease. Although the process for the removal of urea and other unwanted charged species is understood, the effect of this removal on the net sodium concentration in the blood after treatment is not clear. In this report, we focus on formulating a fundamentally-based model to address this question. We consider the formulation near the membrane at the pore scale in order to determine effective jump conditions in ionic concentrations, electric potential and flow rate based on the membrane properties, and in order to determine whether electroneutrality holds within the pore. Secondly, we consider the local blood-cell concentration within one of the fibres and how this varies axially within the dialysis cartridge. Lastly, we consider a simple one-dimensional model of the charged species problem and find that advection transport through the membrane is important for sodium transport, but less pertinent for transport of other cation species.

---

[1]`tilley@wpi.edu`

1 Introduction

Kidney disease is treated worldwide by the use of surgical transplantation and more often, due to lack of donor organs, dialysis. The overall aim of dialysis is to remove waste products, such as urea, from the patient's blood. Dialysis is performed using a dilayzer machine, whereby blood is taken from the patient, and passed through the dialyzer where filtration occurs, before being returned to the patients bloodstream in a continual process. A single dialysis session can last anywhere up to four hours.

The process, however, is by no means perfect. Patients post-dialysis show a wide variation in the concentration of certain solutes within their blood, for instance sodium. Sodium imbalance, for instance excess, can lead to higher water retention which can have adverse health effects. With end stage renal disease increasing by between 5% and 10% per year worldwide, there is an ever increasing need to more fully understand and improve the dialysis process. In this report we present a number of mathematical models which go some way towards providing a deterministic model of dialysis by focusing on the mechanisms involved in the filtration of waste products from the blood in a dialyzer.

A typical dialyzer is illustrated in Figure 1. The machine works by passing blood through perforated tubes encased in a cassette within the dialyzer. As blood flows in one direction down the tubes (radius$\sim 200\mu$m), dialysate, the filtration fluid, is passed in the opposite direction, thus forming a counter-current flow regime between the two fluids. The two flows are connected by a number of smaller channels (radius$\sim 5\mu$m), which allows exchange of solutes between the blood and dialysate. The exchange of solutes is driven by both diffusion and convection through the channels. Details on the geometry of the tubes, the size of the interconnecting channels, channels per tube and other details relevant to the problems discussed in this report are detailed in Table 1.

Dialysate is designed to filter the blood during the dialysis process (which can take anywhere up to four hours) without altering the solute concentrations within it. As such the dialysate contains the main solutes found within blood (e.g. potassium-K^+, sodium-Na^+, and chlorine-Cl^-). The unfiltered blood contains these same solutes as well as urea (to be filtered), along with blood cells and various negatively-charged proteins that are not filtered.

Whilst it is relatively simple to understand the basic elements of dialysis, the effect of the physical processes (fluid flow, solute transport) within a dialyzer requires detailed quantitative understanding of each process in order to accurately understand the overall blood filtration effects. As such the problem is ripe for mathematical modelling, with a number of models formulated to date. We briefly review here the different modelling approaches. For further details the reader should consult the recent review of [3].

Mathematical modelling approaches fall in to two main areas: (i) compartmental ordinary differential equation (ODE) which model the patient-dialyzer system; and (ii) models which describe the spatial variation in solute concentration fluid flow within a dialyzer using the theory of partial differential equations (PDEs). Both model types are generally parameterised by comparing and/or fitting model outcomes to experimental and/or patient data. Their main use then is in predicting the effective removal of urea from the blood stream and the solute concentration at the end of the process. Sodium is a common solute of interest given the issue of overhydration and the resultant health issues.

Compartmental models include descriptions of the fluid (blood plasma, dialysate) and solutes within the patient/dialyzer system, and focus on key issues, for instance urea or
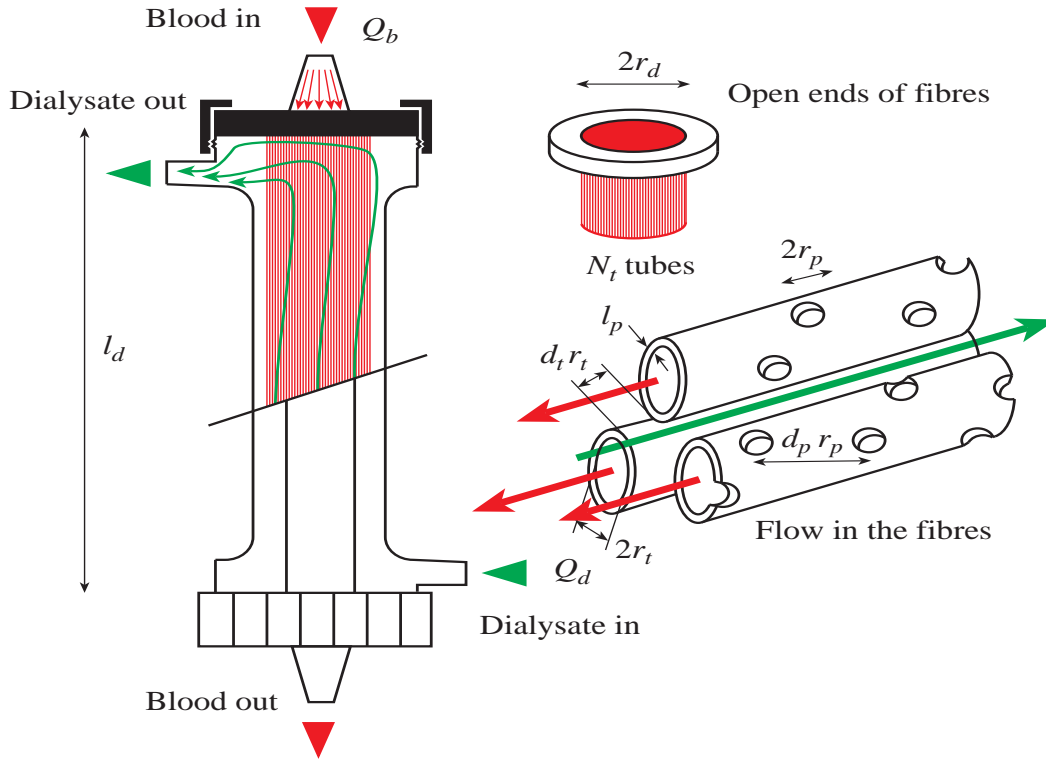
Figure 1 A schematic representation of a typical dialyzer (left) and the geometrical layout of a cassette showing the porosity of the tubes (right).

specific solute clearance. The basic urea model [3] considers a single compartment into which urea passes and is then separated into a fluid of volume V and urea of concentration C. Urea is then removed from the compartment at a constant rate. This leads to a single ODE which can be solved analytically to determine the change in urea concetration over time. More complicated models consider different compartmentalisations. For instance [9] built on the work of [10] and considered a three compartment model: intracellular (representing fluid inside patient cells), interstitial (representing fluid outside cells) separating the cell from the final compartment, the blood plasma. The dialysate only affects the blood plasma. Each compartment is separated by a 'membrane'. In the intracellular to extracellular compartments this is equivalent to that of the cell membrane, whereas the interstitial to blood plasma membrane represents resistance of solute flow between these regions. Similar models have been used to fit to experimental data regarding the profile of solutes from patients and experimentation on dialyzers [6].

A similar model [12] used three compartments for the body fluids (plasma, interstitial and intracellular, as mentioned above) and tracked transport of the main solutes between these compartments and between the blood and dialysate. The authors claim that the required parameters for the model can be determined a priori based on the body weight and measured pre-dialysis plasma concentration values for patients, and that their model's predictions agreed fairly well with the results from multiple dialysis sessions for six patients. They suggest using the model to tailor dialysis sessions (i.e. by varying the length of the dialysis session and/or the concentrations of various ions in the dialysate solution)

to the needs of individual patients. The desirability of implementing such a scheme, and some of the difficulties of doing so in an actual clinical setting, are discussed in [14]. Profiled hemodialysis is an even more ambitious scheme for minimizing the unpleasant side effects of dialysis by varying operational parameters of the dialysis machine (e.g. sodium concentration in dialysate) as a function of time [9].

In [13], some of the issues involved in building a compartmental model of the dialysis process are discussed. Starting from a simple one compartment model, several more detailed models with successively more compartments are built and investigated. All of the models considered in this reference only track one concentration, that of the main 'toxic substance' (presumably urea) that the dialysis treatment is designed to remove from the blood.

There are considerably fewer models of dialysis which include descriptions of the variation in fluid flow and solute concentrations within a dialyzer (see the introduction to [5] for a brief review). Such models are generally solved numerically. Ding *et al.* [4] modelled a hollow fiber hemodialyzer as two interpenetrating porous regions, of differing porosity, containing blood and dialysate respectively. The two regions are separated by a thin porous membrane. The fluid flow of blood and dialysate were considered to be governed by the Navier-Stokes equations, with the concentration of dialysate and blood modelled by quasi-steady state diffusion-convection equations in each region. The membrane flow is described by a difference in the pressure between the blood and dialysate regions and the concentration of the blood and dialysate. Ding *et al.* [4] obtained numerical solutions to their system of equations to predict the spatial variation in urea along the length of the dialyzer. This was compared with experimental data and shown to be in good agreement. Similar porous media models have been formulated and solved by Nordon and Shindhelm [7] and Osuga *et al.* [8].

Of interest here is to understand the dominant mechanisms of solute transport from the blood to the dialysate under normal operating conditions. The pore-scale processes within the membrane, which include advection from the flow of liquid from the blood to the dialyzer, electrodiffusion effects due to the induced electric fields from the ions themselves, and reverse osmosis effects due to the concentration jump across the membrane, are key to understanding this transport. Inherent in this understanding is the characteristic lengths and other scales related to this problem. In Table 1, we list the characteristic geometric parameters of the cartridge, the tubing, and the typical pore scales of the semi-permeable membrane, and we list the diffusion and concentration values in Table 1. In Table 1 we list the effective flow values during normal operating conditions, along with some typical nondimensional quantities based on the values in Table 1. Since the dialysate and the blood contains concentrations of charged species, we list some characteristic electrical parameters in Table 1,

In this report, we focus on three distinct problems. The first problem relates to the dependence of the solvent and solute transport through the pores in the semi-permeable membrane (see Section 2). The second problem, discussed in Section 3, considers the plasma/fluid transport through the membrane due to pressure differences in the blood and dialysate regions. Finally, in Section 4, we consider a simple one-dimensional model of solute transport across the membrane. We conclude in Section 5.

2 The problem in a single pore

The dialysis process of removing fluid, urea and potassium ions from the patient's plasma is controlled by the transport properties of the membrane. To understand these

Table 1 Geometrical quantities from literature, many from [17].

Quantity	Symbol	Value
Dialyser length	l_d	0.2 m
Dialyser radius	r_d	0.02 m
Number of tubes	N_t	12,000
Tube radius	r_t	10^{-4} m
Number of pores per unit area	n_{ppua}	10^{13} m^{-2}
Length of pore (wall thickness)	l_p	15×10^{-6} m
Pore radius	r_p	5×10^{-9} m
Cross-sectional area of dialyser	$A_d = \pi r_d^2$	1.3×10^{-3} m^2
Inner area - single tube	$A_{ti} = \pi r_t^2$	3.1×10^{-8} m^2
Outer area - single tube	$A_{to} = \pi(r_t + l_p)^2$	4.2×10^{-8} m^2
Area of inner tube surface	$A_s = 2N_t \pi r_t l_d$	1.5 m^2
Fraction of cross-sectional area occupied by tubes	$\phi_t = N_t A_{to}/A_d$	0.40
Scaled distance between neighbouring tubes (assumes triangular lattice)	$d_t = \sqrt{2\pi/(\sqrt{3}\phi_t)} - 2$	1.0
Number of pores	$N_p = 2N_t \pi r_t l_d n_{ppua}$	1.5×10^{13}
Area of pore	$A_p = \pi r_p^2$	7.9×10^{-17} m^2
Pore fraction of tube surface area	$\phi_p = \pi r_p^2 n_{ppua}$	7.9×10^{-4}
Nondim distance between neighbouring pores (assumes triangular lattice)	$d_p = \sqrt{2\pi/(\sqrt{3}\phi_p)} - 2$	66

Table 2 Flux/flow quantities.

Quantity	Symbol	Value
Fluxes:		
Flux of blood	Q_b	$400 \times 10^{-6}/60$ m^3/s
Flux of dialysate	Q_d	$800 \times 10^{-6}/60$ m^3/s
Blood filtration rate	Q_p	$10^{-3}/3600$ m^3/s
Flow:		
Average blood velocity	$U_b = Q_b/(N_t A_{ti})$	0.0018 m/s
Average diastolate velocity	$U_d = Q_d/(A_d(1 - \phi_t))$	0.0018 m/s
Average velocity in pore	$U_p = Q_p/(N_p A_p)$	2.3×10^{-4} m/s
Reynolds number of the blood	$Re_b = 2U_b r_t/\nu_b$	0.88
Reynolds number of the diastolate	$Re_d = U_d r_t d_t/\nu_d$	0.45
Péclet number of sodium (or potassium) in blood	$Pe_{Nab} = 2U_b r_d/D_{Na}$	3.5×10^5
Péclet number of sodium (or potassium) in pore	$Pe_{Nap} = U_p l_p/D_{Na}$	1.8

properties fundamentally, we need to investigate the ion and fluid transport through a single pore. During the workshop, we considered only transport of the ions by a prescribed pressure field, which is described in Section 2.1 below. In general, however, the flow in these membranes is driven by concentration gradients local to the membrane in the bulk.

Table 3 Electrical quantities from literature, many from [17].

Quantity	Symbol	Value
Electric constants:		
Proton charge	e	1.602×10^{-19} C
Permittivity of free space	ϵ_0	8.85×10^{-12} A^{2}s^{4}kg^{-1}m^{-3}
Relative permittivity	ϵ_R	80
Boltzmann's constant	k_B	1.38×10^{-23} J/K
Faraday's constant	$F = N_a\,e$	9.4×10^4 C/mol
Debye lengthscale	$\sqrt{\epsilon_0 \epsilon_R k_B T/(4\,\pi\,e\,F\,c_{Na})}$	1.2×10^{-9} m

Table 4 Diffusion and viscosity quantities from literature, many from [17].

Quantity	Symbol	Value
Diffusion and viscosity:		
Kinematic viscosity of blood	ν_b	4×10^{-6} m^2/s
Kinematic viscosity of dialysate	ν_d	4×10^{-6} m^2/s
Diffusion coefficient of sodium	D_{Na}	2×10^{-9} m^2/s
Diffusion coefficient of potassium	D_K	2×10^{-9} m^2/s
Diffusion coefficient of urea	D_{urea}	1.8×10^{-9} m^2/s
Operating Temperature	T	300 K
Avogadro's number	N_a	6.023×10^{23}
Sodium concentration in blood	c_{Na}	140 mmol/l$= 1.4 \times 10^2$ mol/m^3

Table 5 Typical pressure drops measured in the cartridge during dialysis [15].

Pressure drop	Value in literature (Pa)
Blood along tubes	2,666
Dialysate	6,666
Across pores (Δp_p)	40,000–49,400

We perform an analysis by Anderson and Malone [2], extended to electrolytes, to include osmotic effects. In this case, the flow field and concentration fields are necessarily coupled. This work is found in Section 2.2. Simple examples of these field equations are presented in each section.

The rationale for this extension is based on the following argument. Fournier [15] gives the blood and dialysate gauge pressures as 117,300 Pa and 74,600 Pa respectively and the pressure drops as 2,666 Pa and 6,666 Pa respectively, meaning the pressure drop across the pores varies between 40,000 Pa and 49,400 Pa. These values are compared in Table 2. This shows that the comparison is quite bad, particularly in the pores. However, both the calculated and the actual values do suggest that the pressure drop across the pores is much larger than that along the length of the dialyzer. We may also calculate the permeability (volume flux per unit area per unit pressure drop) across the walls of the tubes, which for $\Delta p_p = 45$ kPa gives

$$\frac{Qp}{2\pi r_t l_d N_t \Delta p_p} \approx 4.1 \times 10^{-12}\, \text{m}^2\text{s/kg}. \tag{2.1}$$
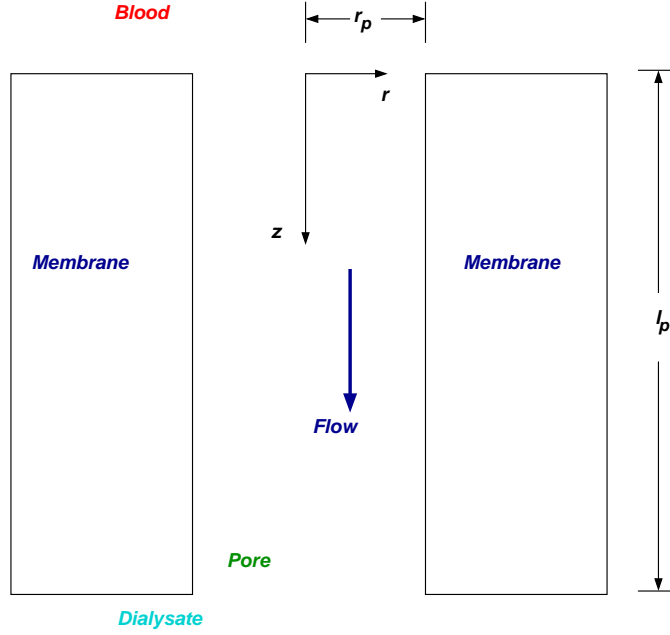
Figure 2 Geometry of pore problem investigated in Section 2.

Values of the permeability of biomaterials are given as 10^{-14}–10^{-9} m²s/kg, and in dialyzers are between 2×10^{-12} and 4×10^{-11} m²s/kg, so these values are consistent with purely pressure-driven flow.

The geometry of the pore problem is shown in Figure 2. The membrane surface on the blood side is at $z = 0$, and we focus on one pore of radius r_p and length l_p.

2.1 Pressure-driven flow. The governing equations for the axisymmetric ion transport are given by [16]

$$\frac{\partial c_i}{\partial t} + \mathbf{u} \cdot \boldsymbol{\nabla} c_i = \boldsymbol{\nabla} \cdot (D_i \boldsymbol{\nabla} c_i) + \boldsymbol{\nabla} \cdot (c_i z_i k_i e \boldsymbol{\nabla} \phi), \tag{2.2}$$

$$\epsilon \nabla^2 \phi = -4\pi \sum_i F\, c_i z_i, \tag{2.3}$$

$$w = \frac{1}{2} w_0 \left(1 - \frac{r^2}{r_p^2} \right), \tag{2.4}$$

where $\mathbf{u} = u\,\mathbf{r} + w\,\mathbf{z}$, ϕ is the electric potential, F is Faraday's constant (see Tables 1 and 1), and (2.2)–(2.3) apply on an axisymmtric domain $0 < r < r_p$ and $0 < z < l_p$. Equation (2.2) represents the transport of species i through the pore, where $i = 1, 2, \ldots N$ denote distinct species, and where c_i is the molar concentration of species i. The second term on the left-hand side represents advection of charge through the pore. The two terms on the right-hand side of (2.2) (from left to right) represent diffusion of charge through the pore and electrodiffusion, respectively. Each species in general has its own rate of diffusion, $D_i = k_B T k_i$, where k_B is Boltzmann's constant, T is the temperature of the solution, k_i is species mobility. In addition, each i-ion has a net charge $z_i e$, where e is the fundamental charge of an electron (see Table 1 for specific values). We assume the flow of the solute

within the pore is pressure-driven Stokes flow in cylindrical coordinates, which results in the quadratic profile shown in (2.4).

Electrodiffusion is driven by gradients in the electric potential ϕ. This potenial is found through (2.3), which represents Gauss's law in electrostatics, where ϵ is the relative dielectric permittivity of the solvent. Note that the net charge density $\rho = \sum_i e\, F\, z_i\, c_i$ is the quantity that drives potential gradients.

Boundary conditions for this problem are no flux conditions at $r \to 0$ and $r = r_p$,

$$r \to 0: \qquad r\frac{\partial c_i}{\partial r} \to 0 \;,\; r\frac{\partial \phi}{\partial r} \to 0, \tag{2.5}$$

$$r = r_p: \qquad \frac{\partial c_i}{\partial r} = \frac{\partial \phi}{\partial r} = 0 \;. \tag{2.6}$$

We are interested in finding effective jump conditions from above and below the pore, and so we assume Dirichlet boundary conditions at $z = 0$ and $z = l_p$

$$z = 0: \qquad c_i = C_i^{(+)} \;,\; \phi = \Phi^{(+)}, \tag{2.7}$$

$$z = l_p: \qquad c_i = C_i^{(-)} \;,\; \phi = \Phi^{(-)} \;. \tag{2.8}$$

We scale r on r_p, z on l_p, t on l_p/w_o, $\mathbf{u}$ on w_o, c_i on C_o, and ϕ on $k_B T/e$ to arrive at the following nondimensional problem

$$\delta^2 Pe_i \left(\frac{\partial C_i}{\partial t} + \frac{1}{2}\left(1 - r^2\right)\frac{\partial C_i}{\partial z} \right) = \frac{1}{r}\frac{\partial}{\partial r}\left(r\frac{\partial C_i}{\partial r}\right) + \delta^2 \frac{\partial^2 C_i}{\partial z^2} + \frac{1}{r}\frac{\partial}{\partial r}\left(z_i C_i \frac{\partial \phi}{\partial r}\right)$$
$$+ \delta^2 \frac{\partial}{\partial z}\left(z_i C_i \frac{\partial \phi}{\partial z}\right), \tag{2.9}$$

$$\frac{1}{r}\frac{\partial}{\partial r}\left(r\frac{\partial \phi}{\partial r}\right) + \delta^2 \frac{\partial^2 \phi}{\partial z^2} = -\frac{1}{\lambda^2}\sum_i z_i C_i, \tag{2.10}$$

where $\delta = r_p/l_p \simeq 3 \times 10^{-4}$ is the aspect ratio of the pore, $Pe_i = w_o l_p/D_i \approx 1.8$ is the Péclet number for each species, and $\lambda = \lambda_D/r_p$ is the Debye length ratio, where the Debye length is given by $\lambda_D = \sqrt{(\epsilon k_B T)/(4\pi e F C_o)}$. The boundary conditions (2.5)–(2.8) have the same form with this scaling

$$r \to 0: \qquad r\frac{\partial c_i}{\partial r} \to 0 \;,\; r\frac{\partial \phi}{\partial r} \to 0, \tag{2.11}$$

$$r = 1: \qquad \frac{\partial c_i}{\partial r} = \frac{\partial \phi}{\partial r} = 0, \tag{2.12}$$

$$z = 0: \qquad c_i = C_i^{(+)} \;,\; \phi = \Phi^{(+)}, \tag{2.13}$$

$$z = 1: \qquad c_i = C_i^{(-)} \;,\; \phi = \Phi^{(-)} \;. \tag{2.14}$$

Although the Debye length scale is on the same order of magnitude as the pore radius, we can consider the problem in the limit of small aspect ratio $\delta \to 0$. We use a regular asymptotic expansion for each of the quantities

$$C_i = n_{i0} + \delta^2 n_{i2} + \dots, \qquad \phi = \phi_0 + \delta^2 \phi_2 + \dots \;. \tag{2.15}$$

At leading order, we find that

$$\frac{1}{r}\frac{\partial}{\partial r}\left(r\frac{\partial n_{i0}}{\partial r}\right) + \frac{1}{r}\frac{\partial}{\partial r}\left(rz_i n_{i0}\frac{\partial \phi_0}{\partial r}\right) = 0, \tag{2.16}$$

$$\frac{1}{r}\frac{\partial}{\partial r}\left(r\frac{\partial \phi_0}{\partial r}\right) = -\frac{1}{\lambda^2}\sum z_i\, n_{i0}\ , \tag{2.17}$$

subject to the no-flux boundary conditions in r. We can integrate (2.16) directly in terms of r, and note that

$$\frac{\partial n_{i0}}{\partial r} + z_i n_{i0}\frac{\partial \phi_o}{\partial r} = 0\ , \tag{2.18}$$

since the fluxes are zero at $r = 0, 1$ for all $0 < z < 1$. A second integration of (2.18) gives the Nerst relation between concentration and potential

$$n_{i0}(r, z, t) = A_i(z, t)e^{-z_i\, \phi_o(r,z,t)}\ . \tag{2.19}$$

Hence, the leading order problem to consider for the potential problem gives

$$\frac{1}{r}\frac{\partial}{\partial r}\left(r\frac{\partial \phi_o}{\partial r}\right) = -\frac{1}{\lambda^2}\sum_i z_i\, A_i(z, t)e^{-z_i\phi_o}\ , \tag{2.20}$$

subject to no-flux boundary conditions (2.11)–(2.12). Note that the trivial solution $\partial\phi_o/\partial r = 0$, or for ϕ independent of r gives the electro-neutrality constraint.

At this stage, we must make a choice in order to solve for (2.20). The simplest choice is to prescribe electro-neutrality *ab initio*,

$$\sum_i z_i\, n_{i0} = \sum_i z_i A_i(z, t)e^{-z_i\phi_o} = 0\ , \quad 0 < r < 1\ , \tag{2.21}$$

which gives that $\phi_o = \phi_o(z, t)$ to leading order, and

$$n_{i0}(z, t) = A_i(z, t)e^{-z_i\phi_o(z,t)}\ .$$

To find the values of n_{i0}, ϕ_o, we go to the $O(\delta^2)$ problem

$$Pe_i\left[\frac{\partial n_{i0}}{\partial t} + \frac{1}{2}\left(1 - r^2\right)\frac{\partial n_{i0}}{\partial z}\right] = \frac{1}{r}\frac{\partial}{\partial r}\left(r\frac{\partial n_{i1}}{\partial r}\right) + \frac{\partial^2 n_{i0}}{\partial z^2} + \frac{1}{r}\frac{\partial}{\partial r}\left(z_i n_{i0}\frac{\partial \phi_1}{\partial r}\right)$$

$$+ \frac{\partial}{\partial z}\left(z_i n_{i0}\frac{\partial \phi_o}{\partial z}\right), \tag{2.22}$$

$$\frac{1}{r}\frac{\partial}{\partial r}\left(r\frac{\partial \phi_1}{\partial r}\right) + \frac{\partial^2 \phi_o}{\partial z^2} = -\frac{1}{\lambda^2}\sum_i z_i\, n_{i1}\ , \tag{2.23}$$

subject to the no-flux boundary conditions (2.11)–(2.12). With these conditions, we can find the effective equation for each n_{i0} as a function of ϕ_o,

$$Pe_i\left(\frac{\partial n_{i0}}{\partial t} + \frac{1}{4}\frac{\partial n_{i0}}{\partial z}\right) = \frac{\partial^2 n_{i0}}{\partial z^2} + \frac{\partial}{\partial z}\left\{z_i n_{i0}\frac{\partial \phi_o}{\partial z}\right\}\ . \tag{2.24}$$

The case of monovalent ions is a classical derivation if the Peclet numbers are the same [1, 16]. If $z_i = \pm 1$ and $Pe_i = Pe$, then we can define a conductivity σ and a charge density ρ_E as

$$\sigma = \sum_i z_i^2\, n_{i0}\ , \qquad \rho_E = \sum_i z_i\, n_{i0} = 0\ .$$

By electro-neutrality, the charge density is zero, and we can add all of the equations in (2.24) to obtain

$$Pe\left(\frac{\partial\sigma}{\partial t} + \frac{1}{4}\frac{\partial\sigma}{\partial z}\right) = \frac{\partial^2\sigma}{\partial z^2} , \tag{2.25}$$

while multiplying each (2.24) by z_i and adding the remainder of the equations gives the relation for the voltage potential

$$\frac{\partial}{\partial z}\left(\sigma\frac{\partial\phi_o}{\partial z}\right) = 0 , \tag{2.26}$$

which states that the current density is uniform in the axial direction of the pore. If we prescribe the conductivity along the blood side of the membrane $\sigma = \sigma_b$ at $z = 0$ and at the dialysate side of the membrane $\sigma = \sigma_d$ at $z = 1$, then we can analytically find the local conductivity and electric potential in the pore

$$\sigma = \frac{e^{Pe} - e^{Pe\,z}}{e^{Pe} - 1}\sigma_b + \frac{e^{Pe\,z} - 1}{e^{Pe} - 1}\sigma_d , \tag{2.27}$$

$$\phi_0 = J_E\frac{e^{Pe} - 1}{\sigma_b\,e^{Pe} - \sigma_d}\left(z - \frac{1}{Pe}\log\sigma\right) + \zeta . \tag{2.28}$$

With (2.27) and (2.28) we can find relations for the net conductivity flux through the pore, along with the net jump in voltage potential

$$Q_\sigma = Pe\,\sigma - \frac{\partial\sigma}{\partial z} = Pe\frac{e^{Pe}\sigma_b - \sigma_d}{e^{Pe} - 1} , \qquad \phi_0|_{z=0}^{z=1} = J_E\frac{e^{Pe} - 1}{e^{Pe}\sigma_b - \sigma_d}\left\{\frac{1}{Pe}\log\left[\frac{\sigma_d}{\sigma_b}\right] + 1\right\} . \tag{2.29}$$

Unfortunately this argument does not generalise easily to a larger number of solutes of general valency.

2.1.1 *Nonzero Pore Charge Density.* In this section, we consider the case when the electro-neutrality condition in (2.21) is relaxed. The leading-order problem is then fully nonlinear in terms of the species concentration and the electric potential. The classical approach to this problem can be found in standard texts (e.g [1]), where the potential is fixed along the pore wall at the ζ-potential. We focused on the case when the membrane acts as an electrical insulator. In order to simplify the analysis, we consider the situation when advection transport is small compared to diffusive transport.

We then consider the nonlinear problem, where both z and r are scaled on the pore radius,

$$\nabla^2 C_i + z_i\nabla\cdot[C_i\nabla\phi] = 0 \tag{2.30}$$

$$\nabla^2\phi = -\frac{1}{\lambda^2}\sum_i z_i C_i = -\alpha\sum_i z_i C_i \tag{2.31}$$

on the domain $0 < z < l_p/r_p \simeq 3\times 10^3$ and $0 < r < 1$, subject to zero normal derivative conditions

$$\frac{\partial C_i}{\partial n} = \frac{\partial\phi}{\partial n} = 0 ,$$

on the boundary. Note that there is no time-dependence on C_i, ϕ at this order.

If (2.19) holds, and we consider a monovalent mixture, we can then lump the positive species p and the negative species n as

$$p = \sum_{z_i=1} C_i \ , \qquad n = \sum_{z_i=-1} C_i \ .$$

If we define

$$C_+ = \sum_{z_i=1} C_i(0)e^{-\phi(0)} \ , \qquad C_- = \sum_{z_i=-1} C_i(0)e^{\phi(0)} \ ,$$

and with a shift in the potential by $\phi^* = \left[\log\left(C_-/C_+\right)\right]/2$, we find the following nonlinear eigenvalue problem for the shifted potential ϕ

$$\nabla^2 \phi \ = \ -\gamma \sinh\phi \ . \tag{2.32}$$

The two simplest classes of solutions for this problem are purely axial solutions and purely radial solutions. For purely axial solutions, let us consider the simplest problem with Dirichlet boundary conditions

$$\frac{d^2\phi}{dz^2} + \gamma\sinh\phi \ = \ 0 \ , \quad 0 < z < \frac{l_p}{r_p}, \tag{2.33}$$

$$\phi(0) = \phi_0 \ , \qquad \lim_{z\to l_p/r_p} \phi = \phi_1 \ . \tag{2.34}$$

Equation (2.33) can be integrated once, and from the constant of integration, we find the relation between the field strength to the difference in potential

$$\left.\left(\frac{d\phi}{dz}\right)^2\right|_{z=0} - \left.\left(\frac{d\phi}{dz}\right)^2\right|_{z\to l_p/r_p} = 2\gamma\left[\cosh\phi_1 - \cosh\phi_o\right] \ . \tag{2.35}$$

From this relation, we note that the classical results arise depending on the value of γ. In the limit $\gamma \gg 1$, then $\phi_1 = \phi_0$, or the pore acts like a conductor. In the limit $\gamma \ll 1$, then $|\phi_z|_{z=0} = |\phi_z|_{z\to l_p/r_p}$, which corresponds to a continuous electric field along the membrane, or the membrane acts like a perfect dielectric.

The purely radial problem

$$\frac{1}{r}\frac{d}{dr}\left[r\frac{d\phi}{dr}\right] = -\gamma\sinh\phi(r)$$

needs to be solved numerically. The eigenvalue γ is found by optimizing over the unknown reference potential $\phi(0)$.

2.2 Modified Solvent Flow. Osmosis through a semi-permeable membrane is described directly in elementary chemistry courses for nonelectrolytes. A membrane is designed to allow solvent molecules to pass through, but prohibit the transport of larger solute molecules. Due to the estimates in kinetic theory, the number of impacts per molecule on either side of the membrane is approximately the same, but the side which has a lower concentration of solute will have a larger number of solvent molecules striking the membrane. Since the solvent molecules can pass through, this results in a net flow of solvent from the low concentration side of the barrier to the higher concentration side. From [2], the accepted equation for the volume flux of solvent in such a system is given by

$$Q_p = L_p \,\Delta P_\infty - L_\Pi \,\Delta\Pi_\infty \ ,$$

where Q_p is the volume flux of the solute, L_p is a hydraulic coefficient, and the notation ΔP_∞ denotes the jump in bulk values of the hydraulic pressure P across the membrane.

Table 6 Typical osmotic pressure drops found from bulk plasma and dialysate values, assuming that there are no electrical effects. Note the bias in the hydrostatic pressure given in Table 2.

Species	Plasma (meq/L)	Dialysate (meq/L)	$\Delta\Pi$ (kPa)
Sodium	140	140	0
Potassium	5	3	5
Chloride	114	110	10
Bicarbonate	20	35	-37
Urea	40	0	99

The additional term corresponds to the "osmotic pressure" $\Pi = RT\,C_\infty$, and L_Π is a conductivity coefficient. For a perfect semi-permeable membrane, $L_\Pi = L_p$. Note that the scale for Π is on the order of $0.35\,\mathrm{MPa}$, which is about one order of magnitude larger than the characteristic hydraulic pressure scale. In the case when the membrane is "leaky", or some solute is allowed to pass through the membrane, $L_p > L_\Pi$. Note that these leaky membranes are the standard approach to simple models of the dialysis process with spatial variation (see [4]).

Note that the dialysis process is designed for the removal primarily of urea from the blood. The osmotic pressures for urea, based on its concentration, is below the hydraulic pressure difference between the blood and the dialysate (see Table 2.2). This suggests that the membranes used in dialysis are leaky, and the coefficient L_Π needs to be determined based on the concentration and electric potential effects within the pore. In principle, there should be a single model that describes the flow of solvent in this situation for the mixture of charged species, and we focus on this topic in this section.

We follow [2] in theme, but consider the case of charged species to find how the concentration gradients determine the fluid velocity in the pore. We begin by considering the the momentum and continuity equations for fluid flow in the pore, assuming fluid inertial effects are negligible (see [1])

$$\nabla \cdot \mathbf{u} = 0, \tag{2.36}$$

$$-\nabla p + \mu \nabla^2 \mathbf{u} + \rho_E \mathbf{E} = 0, \tag{2.37}$$

on $0 < r < r_p$, $0 < z < l_p$, where $\mathbf{u} = u\mathbf{r} + w\mathbf{z}$ is the velocity field in the pore, p is the fluid pressure, μ is the dynamic viscosity, $\rho_E = \sum_i z_i\,e\,F\,C_i$ is the charge density, and $\mathbf{E} = -\nabla\phi$ is the electric field.

We scale r on r_p, z on l_p, w on $w_o = \delta\,[C_oFk_BTr_p/\mu]$, p on $p_o = \mu w_o l_p/r_p^2$, and consider the same asymptotic series expansion as in Section 2.1. For each of the concentration fields, Nerst's relation (2.19) holds (written here in dimensional form for clarity)

$$C_i = C_o A_i(z,t) e^{-z_i\,F\,(\phi(r,z,t)-\Phi^+)/RT} \ .$$

Note that from this form, the osmotic pressures can be found formally as

$$\Pi_i = RT\,C_i = -z_i\,F \int C_i d\phi \ ,$$

which suggests that the $A_i(z,t)$ are effectively the nondimensional partial osmotic pressure of species i in the pore.

From the leading order r-momentum equation, we have

$$\frac{\partial p}{\partial r} + \sum_i z_i n_{oi} \frac{\partial \phi}{\partial r} = 0 \ , \tag{2.38}$$

which has a first integral that gives

$$p(r,z,t) = P_o(z,t) - \sum_i A_i(z,t) e^{-z_i \phi(r,z,t)} \ . \tag{2.39}$$

To consider the z-momentum equations, we note that

$$\frac{\partial p}{\partial z} = \frac{\partial P_o}{\partial z} - \sum_i \left(\frac{\partial A_i}{\partial z} - z_i A_i \frac{\partial \phi}{\partial z} \right) e^{-z_i \phi} \ ,$$

which results in the following problem for the axial fluid velocity w

$$\frac{1}{r} \frac{\partial}{\partial r} \left(r \frac{\partial w}{\partial r} \right) = \frac{\partial P_o}{\partial z} - \sum_i \frac{\partial A_i}{\partial z} e^{-z_i \phi(r,z,t)} \ , \tag{2.40}$$

with $\lim_{r \to 0} r \partial w / \partial r = 0$ and $w = 0$ along the pore wall $r = 1$. Formally, the solution can be written in terms of the following integral

$$w = \int_r^1 \frac{1}{r_2} \int_0^{r_2} r_1 \left(\frac{\partial P_o}{\partial z} - \sum_i \frac{\partial A_i}{\partial z} e^{-z_i \phi(r_1,z,t)} \right) dr_1 \, dr_2 \ .$$

To solve for u, we use the continuity equation (2.36) with the expression of w above. Requiring that both $u = 0$ along $r = 0$ and $r = 1$ gives a constraint for P_o in terms of the electric potential ϕ. However, in this general form, the transport equations for n_{0i} along with Gauss's equation for ϕ are highly coupled.

As a simple example, let us assume electro-neutrality in the pore, which gives $\phi = \phi(z,t)$. Note that the pressure $p = p(z,t)$ still has the osmotic terms in its expression, and the expression for w in this case becomes

$$w = \frac{r^2 - 1}{4} \left(\frac{\partial P_o}{\partial z} - \sum_i \frac{\partial A_i}{\partial z} e^{-z_i \phi(z,t)} \right) \ . \tag{2.41}$$

From (2.36), we find that u is given by

$$u = -\left(\frac{r^3}{16} - \frac{r}{8} \right) \frac{\partial}{\partial z} \left\{ \frac{\partial P_o}{\partial z} - \sum_i \frac{\partial A_i}{\partial z} e^{-z_i \phi} \right\} \ , \tag{2.42}$$

and the requirement that $u = 0$ along $r = 1$ gives the following Reynolds equation for P_o

$$\frac{\partial}{\partial z} \left(\frac{\partial P_o}{\partial z} - \sum_i \frac{\partial A_i}{\partial z} e^{-z_i \phi} \right) = 0 \ . \tag{2.43}$$

One integration gives that the flow rate through the pore is constant, or

$$Q_p = -\frac{1}{16} \left(\frac{\partial P_o}{\partial z} - \sum_i \frac{\partial A_i}{\partial z} e^{-z_i \phi} \right) \ . \tag{2.44}$$

A second integral, if possible, would give the leaky flux relation for solvent in terms of the bulk hydraulic pressure and the bulk concentrations of each species. Note, however, that the constant flow rate then gives a velocity profile of the form (2.4), which suggests that the results of Section 2.1 hold for this particular example.

3 Porous-Medium Membrane Model

In this section, the motion of the fluid through the cartridge is assumed to be pressure driven. Opposing pressure gradients are imposed at both ends of the device in order to force the blood and the dialysate to travel in opposite directions. Furthermore, the reference pressure of the blood exceeds the pressure of the dialysate, resulting in fluid from the blood flowing through the membrane and into the dialysate solution. The red blood cells are unable to penetrate the membrane and as a result, their concentration in the fibre increases. The goal of this section is to compute the large scale flow within a single fibre and the surrounding dialysate. Using this fluid velocity profile, the concentration of red blood cells in the fibre can be obtained. How the concentration of solute varies with the removal of the plasma is left for a later work.

3.1 A Simple Model. To describe the essential features of the large scale flow, we consider the two dimensional motion of fluid that is confined between two adjacent regions. These regions are separated by a permeable membrane (see Figure 3). One of these regions represents the interior of the fibre where the blood flows. The other represents the exterior region of dialysate solution. We apply symmetry conditions along $z = \pm r_t$. For simplicity, we assume that the "radius" of the dialysate region is equal to the radius of the fibre. Changing this value should not have a significant quantitative effect on the dynamics of the system. The length of the fibre, l_d, is much greater than the radius r_t in the cartridge, and this fact will be used to simplify the governing equations. Since the flow is pressure driven, we further assume that the pressure is prescribed at both ends of both regions.

The fluid in both regions is assumed to be modelled by the steady, incompressible, Navier-Stokes equations. In two spatial dimensions, these can be written as

$$\rho\left(\mathbf{u} \cdot \nabla\right)u = -\frac{\partial p}{\partial x} + \mu\nabla^2 u, \tag{3.1a}$$

$$\rho\left(\mathbf{u} \cdot \nabla\right)w = -\frac{\partial p}{\partial z} + \mu\nabla^2 w, \tag{3.1b}$$

$$\frac{\partial u}{\partial x} + \frac{\partial w}{\partial z} = 0 \; , \tag{3.1c}$$

where $\mathbf{u} = u(x,z)\mathbf{x} + w(x,z)\mathbf{z}$ is the fluid velocity vector written in terms of components along the standard Cartesian unit vectors, ρ is the fluid density, p is the hydrodynamic pressure, μ is the dynamic viscosity of the fluid, and ∇ is the gradient operator in Cartesian coordinates. The velocity of the blood and of the dialysate is denoted by $\mathbf{u}_1$ and $\mathbf{u}_2$, respectively. Similarly, the pressure in the blood and in the dialysate is labelled as p_1 and p_2. For simplicity, the density of the two fluids, as well as their viscosities, are assumed to be equal. The concentration of red blood cells, $b(x,z)$, is governed by a steady advection-diffusion equation

$$\nabla \cdot \mathbf{J} = 0, \quad \mathbf{J} = \mathbf{u}_1\, b - D\nabla b, \tag{3.2}$$

where $\mathbf{J} = \mathbf{J}(x,z)$ is the flux of red blood cells and D is the diffusion coefficient. This equation only holds in the interior of the fibre, since red blood cells cannot pass through the membrane.
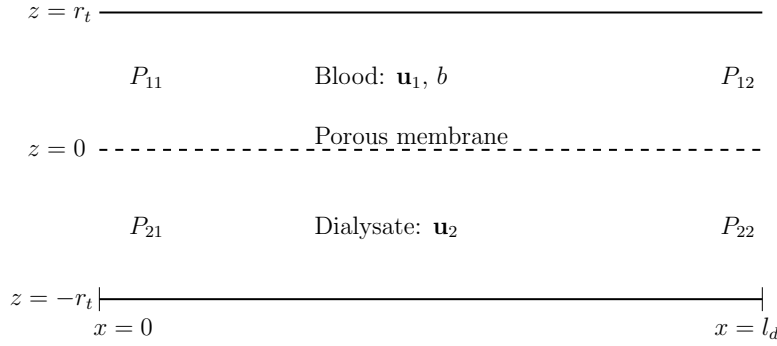
Figure 3 Model geometry. The top region corresponds to the interior of the fibre where the blood is flowing, whereas the bottom corresponds to the dialysate region exterior to the fibre. The length and the radius of the fibre are denoted by l_d and r_t, respectively. Governing equations will model fluid velocities $\mathbf{u}_1$ and $\mathbf{u}_2$ in the blood and dialysate regions, respectively, as well as the blood cell concentration b inside the fibre. The P_{ij} denote prescribed fluid pressures at the ends of the system.

The symmetry of the system implies that there is a stress-free condition and a no-flow condition on the fluid velocities at the center of the regions,

$$\frac{\partial u_1}{\partial z} = w_1 = 0, \quad z = r_t,$$
$$\frac{\partial u_2}{\partial z} = w_2 = 0, \quad z = -r_t.$$

Along the membrane, there is a no-slip condition on the horizontal fluid velocities , $u_1 = u_2 = 0$ along $z = 0$. Since fluid can pass through this membrane, the vertical velocity is governed by Darcy's law at $z = 0$, which states that the vertical fluid velocity at the membrane is proportional to the pressure difference across it

$$w_1 = w_2 = \frac{k}{\mu} \frac{p_2 - p_1}{l_p}, \quad z = 0, \tag{3.3}$$

where k and l_p are the permeability and the thickness of the membrane, respectively. The permeability is assumed to be constant, which implies that none of the pores in the membrane become blocked by red blood cells. It is further assumed that the pressure at the ends of each region is prescribed,

$$p_i = P_{i1}, \quad x = 0,$$
$$p_i = P_{i2}, \quad x = l_d, \tag{3.4}$$

for $i = 1, 2$. To obtain the correct flow, the following inequalities are assumed to be true

$$P_{21} < P_{22} < P_{12} < P_{11}.$$

These are needed to ensure that the blood and the dialysate flow in opposite directions and they allow the water from the blood to cross the membrane.

It is assumed that the concentration of red blood cells entering the device is a fixed constant b_0. Furthermore, there is zero flux of red blood cells at $z = 0$ and $z = r_t$. The condition at $z = 0$ arises because red blood cells cannot pass through the membrane and the condition at $z = l$ is from the symmetry. In summary, the boundary conditions for the

concentration are given by

$$b = b_0, \quad x = 0,$$
$$\mathbf{J} \cdot \mathbf{n} = 0, \quad z = 0, r_t,$$

where $\mathbf{n}$ is a unit vector normal to the boundary. Although the equation which governs the concentration (3.2) is second order in x, further analysis will show that only one boundary condition is required.

3.2 Scaling and Nondimensionalization. One of the characteristic properties of each fibre is its length. Typically, a fibre is approximately one hundred times longer than it is wide. Therefore, we define the small parameter $\varepsilon = r_t/l_d \ll 1$ and rescale the governing equations. In particular, we scale the physical dimensions by $x \to l_d x$, $z \to r_t z$, where the new, nondimensional, domain is from $0 \le x \le 1$, $-1 \le z \le 1$. The velocity components and the pressure are scaled according to

$$u \to U_b\, u, \quad w \to \varepsilon U_b\, w, \quad p \to \frac{\mu U_b}{r_t \varepsilon}\, p,$$

where U_b is the mean velocity of the blood through the device. With these new variables, the Navier-Stokes equations (3.1b) become

$$\varepsilon^2 \mathrm{Re}\,(\mathbf{u} \cdot \nabla)u \;=\; -\frac{\partial p}{\partial x} + \varepsilon^2 \frac{\partial^2 u}{\partial x^2} + \frac{\partial u}{\partial z}, \tag{3.5}$$

$$\varepsilon^4 \mathrm{Re}\,(\mathbf{u} \cdot \nabla)w \;=\; -\frac{\partial p}{\partial z} + \varepsilon^2 \left(\varepsilon^2 \frac{\partial^2 w}{\partial x^2} + \frac{\partial^2 w}{\partial z^2} \right), \tag{3.6}$$

$$\frac{\partial u}{\partial x} + \frac{\partial w}{\partial z} = 0, \tag{3.7}$$

where the Reynolds number is defined as

$$\mathrm{Re} = \frac{\rho U_b l_d}{\mu}.$$

From Table 1, $\mathrm{Re} \sim O(1)$. Therefore, to leading order, the pressure along the z direction is constant, and the pressure gradient in the x direction is balanced by viscous diffusion in the z direction. The boundary conditions essentially remain unchanged, except for scaling the constant values in (3.4) and scaling Darcy's law in (3.3) to become

$$w = K(p_2 - p_1),$$

where $K = k/r_t l_p \varepsilon^2 \sim O(1)$.

The concentration can be rescaled according to $b \to b_0\, b$, resulting in the nondimensional advection-diffusion equation

$$\varepsilon^2 \mathrm{Pe}\,(\mathbf{u}_1 \cdot \nabla)b = \varepsilon^2 \frac{\partial^2 b}{\partial x^2} + \frac{\partial^2 b}{\partial z^2}, \tag{3.8}$$

where the Péclet number for the blood cells is given by

$$\mathrm{Pe_b} = \frac{U_b l_d}{D} \sim O(\varepsilon^{-2}).$$

Thus, to leading order, the advection of red blood cells is balanced by their diffusion in the z direction. The boundary conditions simplify to become $b = 1$ at $x = 0$ and

$$\varepsilon^2 \mathrm{Pe}\, w\, b - b_z = 0, \quad z = 0, 1.$$

As can be seen from (3.8), the second order derivative in x drops out. Indeed, only a single boundary condition in x is needed to obtain a solution at leading order.

3.3 Solution. To leading order, (3.6) suggests that $p = p(x)$. In addition, (3.5) gives the following velocity profiles in the axial direction in each region

$$u_1 = \frac{dp_1}{dx}\left(\frac{z^2}{2} - z\right),$$

$$u_2 = \frac{dp_2}{\partial x}\left(\frac{z^2}{2} + z\right).$$

Conservation of mass (3.7), along with the no-flow conditions at $z = \pm 1$ gives the vertical velocity component in each domain

$$w_1 = \frac{d^2 p_1}{dx^2}\left(\frac{-z^3}{6} + \frac{z^2}{2} - \frac{1}{3}\right),$$

$$w_2 = \frac{d^2 p_2}{dx^2}\left(\frac{-z^3}{6} - \frac{z^2}{2} + \frac{1}{3}\right).$$

Applying the condition on w at $z = 0$ shows the pressure must satisfy the system of ordinary differential equations given by

$$\frac{d^2 p_1}{dx^2} = 3K(p_1 - p_2),$$

$$\frac{d^2 p_2}{dx^2} = 3K(p_2 - p_1).$$

Each solution takes the form $p_i(x) = a_{i,1}e^{\sqrt{6K}x} + a_{i,2}e^{-\sqrt{6K}x} + a_{i,3}x + a_{i,4}$. The coefficients are cumbersome functions of both K and the pressure's boundary conditions, and showing them here would provide no further insight.

Because the flow is assumed to be two dimensional and incompressible, stream functions ψ_i can be found. Solving $u = \psi_z$ and $w = -\psi_x$ in each region yields the two stream functions

$$\psi_1 = \frac{dp_1}{dx}\left(\frac{z^3}{6} - \frac{z^2}{2} + \frac{1}{3}\right),$$

$$\psi_2 = \frac{dp_2}{dx}\left(\frac{z^3}{6} + \frac{z^2}{2} - \frac{1}{3}\right).$$

Using the fluid velocity found above, the concentration of red blood cells in the upper region can be solved. Despite the governing equation being linear, the velocities are sufficiently complicated that it could not be solved analytically. Instead, a simple, upwinded, finite differencing scheme was used. In particular, central differencing was used in the z direction and backwards differencing was used in the x direction to account for the blood travelling in the positive x direction.

3.4 Results and Discussion. The scaled streamlines can be seen in Figure 4. Blood enters the top region from the left and has a small downward component, which is a result of the prescribed pressure differences on the left and right boundaries and the porous membrane. In the bottom region, dialysate enters from the right and also has a small downward component. The flow from the top to the bottom region is expected, as this corresponds
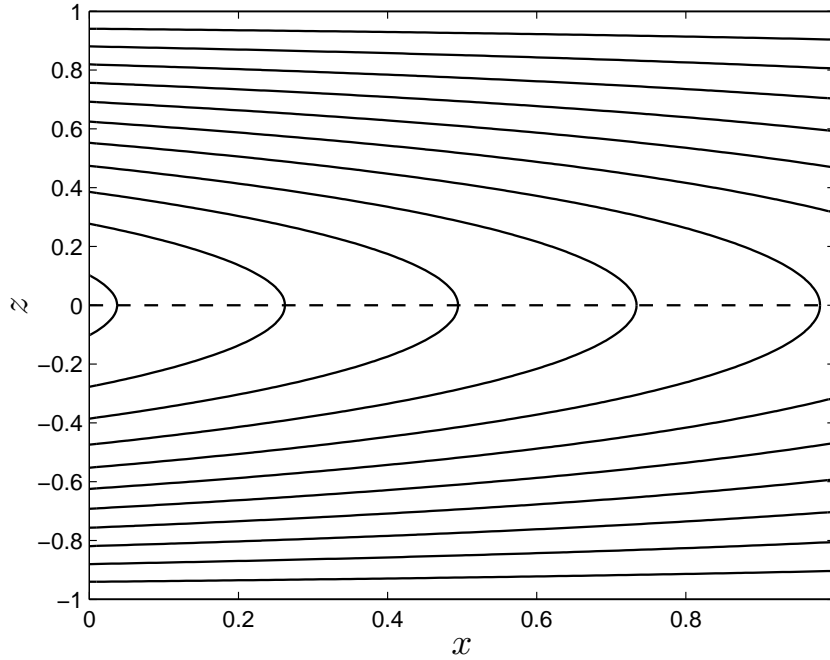
Figure 4 Scaled streamlines of the flow in two regions separated by a porous membrane (dashed line).

to plasma water leaving the inside of the hollow fibres and entering the dialysate fluid space, which is what happens during the dialysis process. This flow represents the underlying convectively dominated régime of solute transport, assuming that electrical effects are negligible.

The pressure found depends only on x, and although it is an exponential function, the value of K is small enough for the function to be approximately linear in both regions. If K is increased enough, there is a pressure drop in the center, and some of the fluid from the right of the top region will flow to the left and then down into the bottom. Since K is proportional to permeability, this intuitively means that increasing the permeability of the membrane makes it harder for the fluid in the top region to make it across. Furthermore, as the permeability tends to zero, the pressure becomes a linear function of x, and both velocity profiles reduce to Poiseuille flow in Cartesian coordinates.

In Figure 5, the concentration gradient of red blood cells in the upper region can be seen, along with the stream lines. The concentration increases toward the membrane and also increases downstream to the right. Interestingly, the concentration gradient appears everywhere to be almost parallel to the streamlines. This implies a large contribution to the movement of red blood cells from diffusion, otherwise we would expect to see concentrations that are constant along the streamlines. In fact, this solution is valid not only for red blood cells, but for any solute that cannot pass through the membrane, such as protein. This is provided the diffusion coefficient of the solute is on the same order as that for red blood cells and, if the solute is charged, electric effects can be ignored.
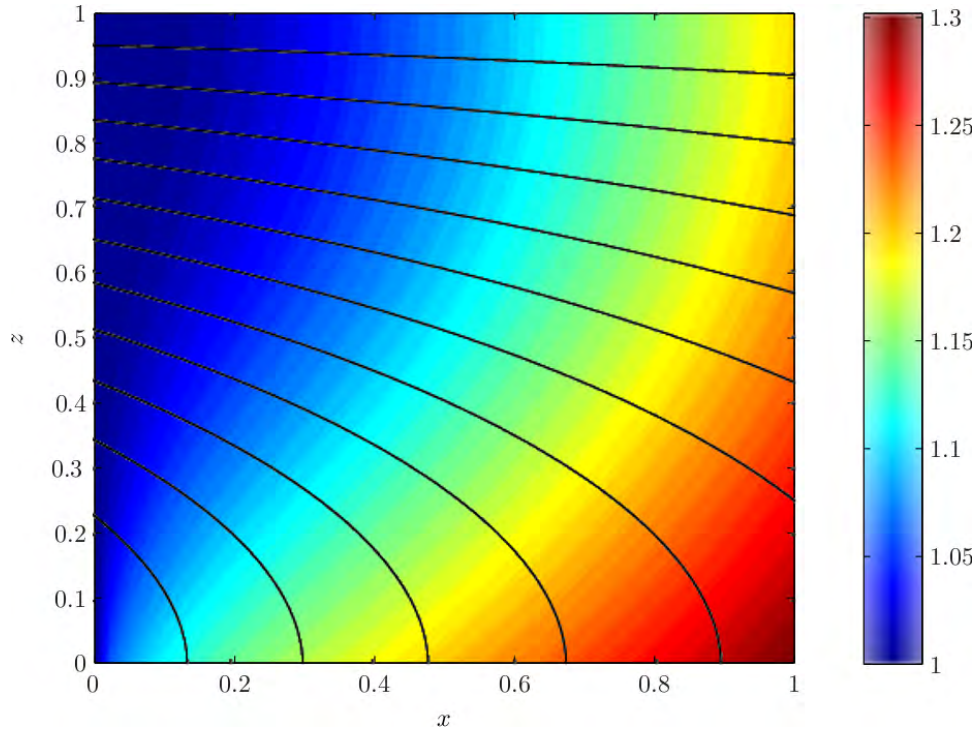
Figure 5 Scaled blood-cell concentration gradient and the streamlines in the fibre.

4 Bulk Solute Transport - Outer Solutions

In this section, we review the different models that try to estimate the solute distribution away from the membrane. In all of these models, since the advective transport to the membrane is much smaller than the advective transport along the filament axis, the effective equations of motion are quasi-steady. In future work, additional details on how advection of solute from the blood into the dialysate would need to be included in order to see changes on this longer time scale.

4.1 Toy model based on transport equilibrium.

4.1.1 *Assumptions.* Our simplest model of a dialyzer assumes that:

1. The transport of solutes between the blood and the dialysate involves the sum of a diffusive term (proportional to the concentration difference across the tube walls), and an electrical term (proportional to the product of the charge on the species, the electric field across the tube walls, and the average concentration).
2. Dialysis continues for sufficient time to allow the blood to come in to equilibrium with the dialysate.
3. Electro-neutrality is maintained in the blood and dialysate at leading order (though minute differences can lead to a significant potential difference, and hence an electric field, across the tube walls).

4.1.2 *Notation and equations.* Consider n diffusing species. Each species $i \in \{1, 2, \dots n\}$ has valencey z_i, and concentrations C_i in the blood and c_i in dialysate initially. Since the

Table 7 Initial concentrations C_i in the blood and c_i in the dialysate, used in the example in Section 4.1.3.

i	Species	z_i	$C_i(0)$	c_i
1	Na^+	$+1$	100	c
2	K^+	$+1$	1	0
3	Cl^-	-1	100	c
4	Pr^-	-1	1	0

dialysate is not recycled, the concentration there remains fixed at c_i, while the concentration in the blood can evolve to its equilibrium value $C_i^\infty = \lim_{t\to\infty} C_i(t)$.

The equations for our model, to determine the equilibrium concentrations C_i^∞ are then as follows. For species that can pass through the tube walls we must have no net transport at equilibrium. We assume that the advective, diffusive and electrical fluxes from the blood to the dialysate are given, respectively, by

$$Q_\text{a} = Q\left(\frac{C_i + c_i}{2}\right), \tag{4.1}$$

$$Q_\text{d} = D_i(C_i - c_i), \tag{4.2}$$

$$Q_\text{e} = \frac{qz_iD_i}{k_BT}\left(\frac{C_i + c_i}{2}\right)E, \tag{4.3}$$

where Q is the flux of fluid through the wall, E is the mean electric field strength, D_i is a species dependent mobility coefficient for passing through the tube walls. At equilibrium, the total flux of each species must be zero. We also have no flux of fluid, so $Q = 0$ and there is no advective transport to consider. Balancing the diffusive and electrical fluxes we find that

$$D_i\left[(C_i^\infty - c_i) + \frac{qz_i}{k_BT}\left(\frac{C_i^\infty + c_i}{2}\right)E\right] = 0. \tag{4.4}$$

For species that are unable to pass through the tube walls, the concentration in the blood cannot alter, so

$$C_i^\infty = C_i. \tag{4.5}$$

Finally the condition of electro-neutrality gives us

$$\sum_i C_i^\infty z_i = 0. \tag{4.6}$$

We now have $n + 1$ equations for the $n + 1$ unknowns $\{C_i^\infty\}$ and E.

4.1.3 *A simple example.* For simplicity we consider just four diffusing species: Na^+, K^+, Cl^-, and Pr^-(the latter representing a negatively charged protein ion). All the ions are monovalent ($z_i = \pm 1$), and the first three can pass through the tube walls, but the protein cannot. Initial concentrations in the blood and dialysate are shown in Table 4.1.3. The blood contains a mixture of all four, whereas the dialysate contains only a concentration c of NaCl.

We want to find appropriate concentration c of NaCl in dialysate to allow removal of K^+ without affecting Na^+ levels. But firstly we solve for the forward problem to determine $\{C_i^\infty\}$ for a given c.
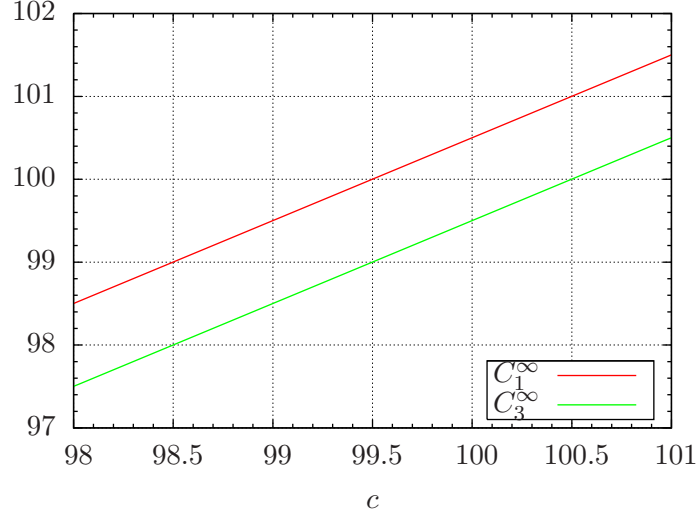
Figure 6 The equilibrium concentrations Na^+ (C_1^∞) and Cl^- (C_3^∞) in the blood as functions of NaCl concentration c in the dialysate for the simple example in Section 4.1.3.

The equations are as follows:

$$(C_1^\infty - c) + E'(C_1^\infty + c) = 0, \tag{4.7}$$

$$C_2^\infty(1 + E') = 0, \tag{4.8}$$

$$(C_3^\infty - c) - E'(C_3^\infty + c) = 0, \tag{4.9}$$

$$C_4^\infty - 1 = 0, \tag{4.10}$$

$$C_1^\infty + C_2^\infty - C_3^\infty - C_4^\infty = 0, \tag{4.11}$$

where $E' = qE/k_B T$.

From (4.8) either $E' = -1$ or $C_2^\infty = 0$. The former is ruled out by (4.7), since this equation could then only be satisfied if $c = 0$. Hence $C_2^\infty = 0$. We can then eliminate E' between (4.7) and (4.9) to obtain a pair of equations for C_1^∞ and C_3^∞:

$$\frac{C_1^\infty - c}{C_1^\infty + c} = -\frac{C_3^\infty - c}{C_3^\infty + c}, \tag{4.12}$$

$$C_1^\infty = 1 + C_3^\infty. \tag{4.13}$$

The solution for C_1^∞ and C_3^∞ in terms of c is now straightforward:

$$C_1^\infty = \frac{\sqrt{1 + 4c^2} + 1}{2}, \tag{4.14}$$

$$C_3^\infty = \frac{\sqrt{1 + 4c^2} - 1}{2}. \tag{4.15}$$

These results are plotted as functions of c in Figure 6.

However, we are more interested in choosing a dialysate concentration c in order to obtain optimal values for C_1^∞ and C_3^∞. If we choose values consistent with (4.13) – necessary to ensure electro-neutrality – the value of c can be computed by solving (4.12). This yields:

$$c = \sqrt{C_1^\infty C_3^\infty}. \tag{4.16}$$

So if we wish to obtain $C_1^\infty = 100$ (so Na$^+$levels are unaffected) and $C_3^\infty = 99$ (to maintain electro-neutrality after the loss of K$^+$), we should set the dialysate concentration of NaCl to be

$$c = 30\sqrt{11} \approx 99.50\,. \tag{4.17}$$

4.2 Argument for using a 1D model. Consider a small length δx of tube that has a concentration drop ΔC_1 from the centre to the boundary. The average radial concentration gradient is $\Delta C_1/r_t$. If we assume advection transport of solute is small compared to diffusion, then the mass flux of solute due to diffusion at the boundary approximately equals

$$D\frac{\Delta C_1}{r_t}(2\pi r_t \delta x) \quad \Rightarrow \quad Q = D\frac{\Delta C_1}{r_t}(2\pi r_t), \tag{4.18}$$

where Q is the mass flux per unit length of tube. The number of pores in that section of boundary is $\phi_p(2\pi r_t)\delta x/A_p$, and therefore the number of pores per unit length equals $\phi_p(2\pi r_t)/A_p$, meaning that we may obtain a second equation for Q

$$Q = D\frac{\Delta C_2}{l_p}A_p\frac{\phi_p(2\pi r_t)}{A_p} = D\frac{\Delta C_2}{l_p}\phi_p(2\pi r_t), \tag{4.19}$$

where ΔC_2 is the concentration drop along a pore. Relating the two expressions for Q,

$$\frac{\Delta C_1}{\Delta C_2} = \frac{\phi_p r_t}{l_p} \approx 0.02, \tag{4.20}$$

which would suggest that most of the concentration drop takes place across the membrane. Therefore we propose to use a 1D model when transport from advection is small compared to diffusive transport.

4.3 One-dimensional steady model. The above assumption motivates a model in one dimension, in which the concentration profile of a single charged species varies in the axial direction along the tubes and along the dialysate, but not significantly in the radial direction. We consider the model depicted in Figure 7. We use a one-dimensional model and assume the flow and the concentration profiles are steady. We also make the simplifying assumption that the velocities of blood and dialysate, U_b and U_d, respectively, are independent of x. This is reasonable since the filtration rate is small compared to the fluxes of blood and dialysate ($Q_p/Q_b \approx 1/24$ and $Q_p/Q_d = 1/48$). Table 2 suggests that the pressure drop, and hence the velocity of the blood in the pores, varies by around 20% along the length, but for simplicity we assume here that the average velocities are constant along the tubes.

In the blood we analyse a control volume consisting of a section of one tube of length δx, as shown in Figure 7. We balance the solute flux across each of the surfaces. The flux along the tube into the control volume is $A_{ti}U_b C_b(x)$, where A_{ti} is the internal area of the tube and C_b is the species concentration. The flux out of the control volume along the tube equals $A_{ti}U_b C_b(x+\delta x)$. To find the flux across the curved surface of the control volume, we find the number of pores, which equals the surface area, $2\pi r_t \delta x$, multiplied by the number of pores per unit area, $n_{ppua} = N_p/A_s$, and then multiply by the flux per pore. The dimensionless flux is given by the expression Q_σ appearing in (2.29), and the corresponding dimensional flux is given by $A_p U_p Q_\sigma/Pe_p$. Since we are interested in the concentration of a single charged species under electrically neutral conditions, the quantities σ_b and σ_d appearing in (2.29) are directly proportional to C_b and C_d in this section. Thus the flux through
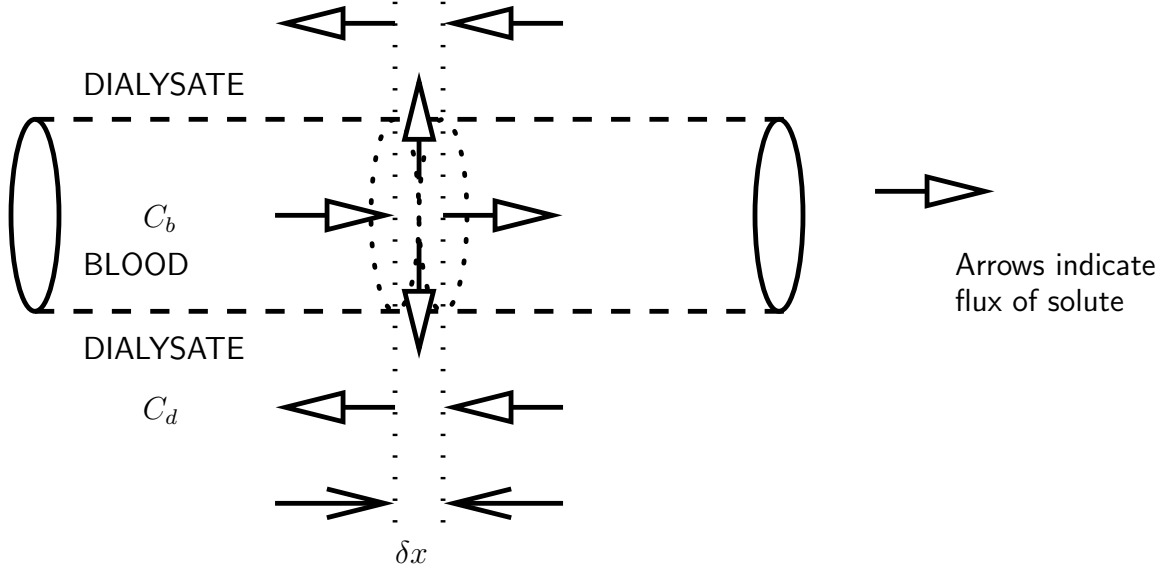
Figure 7 Schematic view of one-dimensional model, showing one tube of the dialyzer with porous walls. It is filled with blood and surrounded by dialysate.

the curved surface of the control volume equals $2\pi r_t N_p A_p U_p Q_\sigma \, \delta x /(Pe_p A_s)$. Balancing the fluxes into and out of the control volume and taking the limit as $\delta x \to 0$, we obtain

$$\frac{\partial C_b}{\partial x} = -\frac{2\pi r_t N_p A_p U_p Q_\sigma}{Pe_p A_s A_{ti} U_b}. \tag{4.21}$$

Unlike the blood, which is partitioned by the tubes, the region occupied by the dialysate is connected, so to analyse the concentration in the dialysate, we consider a control volume containing all of the dialysate between x and $x + \delta x$. This is a cylindrical region with N_t cylindrical holes in it. The flux into the control volume through the surface at x is $(1 - \phi_t)A_d U_d C_b(x)$, the flux through $x + \delta x$ equals $(1 - \phi_t)A_d U_d C_b(x + \delta x)$, and the flux from the tubes equals $2\pi r_t N_t N_p A_p U_p Q_\sigma \delta x /(Pe_p A_s)$, meaning we obtain:

$$\frac{\partial C_d}{\partial x} = -\frac{2\pi r_t N_t N_p A_p U_p Q_\sigma}{Pe_p A_s (1 - \phi_t) A_d U_d}. \tag{4.22}$$

Substituting the expression for Q_b from (2.29), (4.21) and (4.22) become

$$\frac{\partial C_b}{\partial x} = -\frac{\lambda}{(e^{Pe_p} - 1)} \left(e^{Pe_p} C_b - C_d \right), \tag{4.23}$$

$$\frac{\partial C_d}{\partial x} = -\frac{\lambda \kappa}{(e^{Pe_p} - 1)} \left(e^{Pe_p} C_b - C_d \right), \tag{4.24}$$

where

$$\lambda = \frac{2\pi r_t N_p A_p U_p}{A_s A_{ti} U_b} \approx 0.043 \, \mathrm{m}^{-1}, \quad \kappa = \frac{N_t A_{ti} U_b}{(1 - \phi_t) A_d U_d} \approx 0.50, \tag{4.25}$$

$$Pe_p \approx 1.8, \quad l_d \approx 0.2 \, \mathrm{m}. \tag{4.26}$$
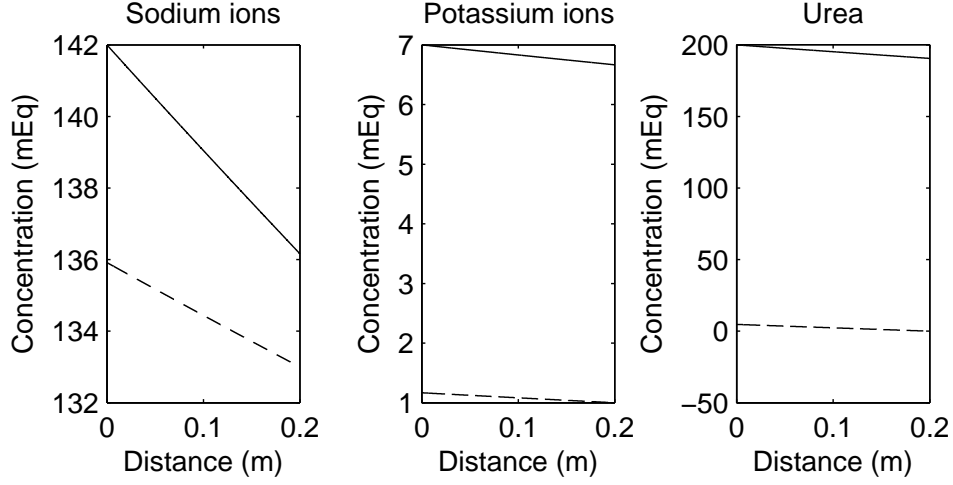
Figure 8 Concentration profiles in the blood (solid) and in the dialysate (dashed).

Table 8 Typical removal rates predicted by the model.

Solute	Normal conc.	Pre-dialysis conc.	Dialysate conc.	Diffusion coefficient	Removal rate	Mass removed (normal-ised)
	(mEq) [15]	(mEq) [15]	(mEq) [15]	(m²/s)	(mol/s)	
Sodium	142	142	133	2×10^{-9}	1.1×10^{-25}	0.78
Potassium	5	7	1	2×10^{-9}	6.2×10^{-27}	0.04
Urea	$21\,\mathrm{mg/ml}$	200	0	1.8×10^{-9}	1.4×10^{-25}	1

These have solution

$$C_b = \frac{\left(e^{Pe_p} C_{b0} - C_{d0}\right) e^{-\gamma x} - \kappa C_{b0} e^{-\gamma l_d} + C_{d0}}{e^{Pe_p} - \kappa e^{-\gamma l_d}}, \tag{4.27}$$

$$C_d = \frac{\kappa(e^{Pe_p} C_{b0} - C_{d0}) e^{-\gamma x} + e^{Pe_p} C_{d0} - \kappa C_{b0} e^{Pe_p - \gamma l_d}}{e^{Pe_p} - \kappa e^{-\gamma l_d}}, \tag{4.28}$$

where

$$\gamma = \frac{\lambda \left(e^{Pe_p} - \kappa\right)}{\left(e^{Pe_p} - 1\right)} \ .$$

This is plotted in Figure 8 for sodium, potassium and urea, assuming that each species appears individually in solution. As can be seen, the concentration profiles show a near linear variation over the lengthscale of the dialyzer.

The total flux of the solute out of the blood is

$$Q_s = \int_0^{l_d} \frac{A_p U_p Q_\sigma}{Pe_p} dx = \frac{A_p U_p \left[1 - e^{-\gamma l_d}\right] \left(e^{Pe_p} C_{b0} - C_{d0}\right)}{\lambda(e^{Pe_p} - 1) \left[e^{Pe_p} - \kappa \, e^{-\gamma l_d}\right]} \ . \tag{4.29}$$

Removal rates are listed in Table 4.3

We may also calculate the ratio of advective to diffusive effects on both sides of the membrane, which is shown in Figure 9. This shows that advection is much more important than diffusion, particularly for sodium.
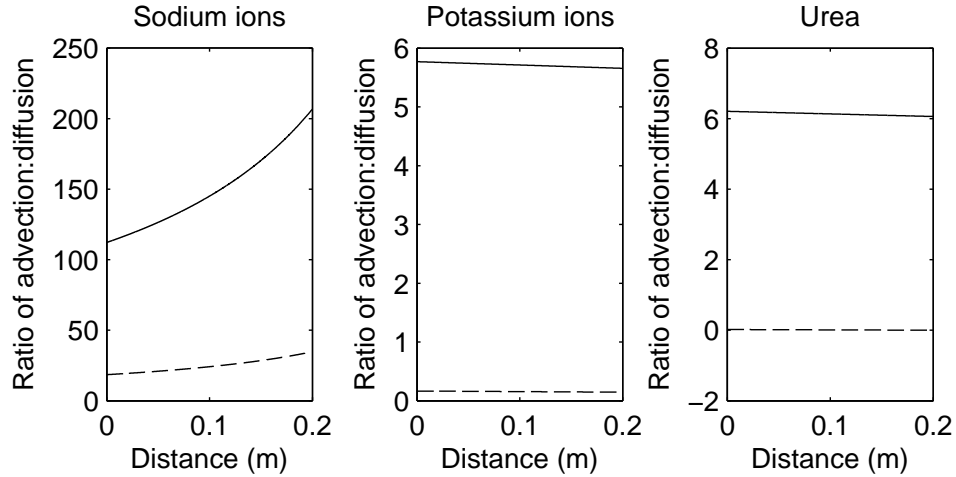
Figure 9 Ratio of advective to diffusive transport at either end (solid – blood, dashed – dialysate) of the pore for the concentration profiles displayed in Figure 8, see Section 2 for details of the calculation.

5 Conclusions

We have investigated the transport of charged species over a variety of length scales. Firstly, we considered the transport of species through a single pore in the membrane that separates the blood from the dialysate. In the case when electro-neutrality holds, the volumetric flow rate remains constant, but depends in general on the local hydraulic and osmotic pressures and on the local electric potential. The electric potential, a streaming potential, depends only on the local solution conductivity if the Péclet numbers are identical for all species. Formally, the classic membrane relations discussed in [2] are reproduced in our analysis in this limit, but the coefficients depend nonlinearly on the solute concentration and electric potenial. In the case when electro-neutrality is weakened, there are two approaches in modeling. The first, and classical, approach is to model the charge in the membrane as a ζ-potential, and prescribe this potential as a Dirichlet boundary condition along the pore wall. Our approach here considers the case of the membrane acting as a pure dielectric. In this case, we find a nonlinear eigenvalue problem for the potential, where the eigenvalue is the ratio of the pore radius to the Debye length scale.

Secondly, we considered the flow of plasma from the blood to the dialysate assuming that concentration effects were negligible. We found that the pressure difference across the dialysate decays exponentially over space, with the decay rate depending on the permeability of the membrane. Although limited to looking at the plasma effects, this model forms a foundation for developing the net charge transport across the membrane, since the solute available to cross into the dialysate is found in the plasma. Further, extensions to this model that include solute transport from the blood cells to the plasma could potentially be implemented with a local analysis of the osmotic transport across the cell wall. Although work for the future, one potential result from such a local analysis would be an effective diffusion coefficient which depends on the local blood cell concentration.

Finally, we investigated the case where the solute distribution was independent of the radial dimension. This case is appropriate if diffusive transport across the membrane is dominant over advective transport. We find that in this case, advective transport appears

to be dominant only for the case of sodium. Since advective transport is dominant for sodium, the concentration depends not only on the axial coordinate but also on the radial coordinate, suggesting that a boundary-layer approach is needed.

References

[1] R.F. Probstein, *Physicochemical Hydrodynamics: An Introduction, 2ⁿᵈ Edition*, Wiley Interscience, 2003.

[2] J.L. Anderson and D.M. Malone, *Mechanism of osmotic flow in porous membranes*, Biophys. J. **14** (1974), 957–982.

[3] J. Waniewski, *Mathematical modelling of fluid and solute transport in hemodialysis and peritoneal dialysis*, J. Memb. Sci. **274** (2006), 24–37.

[4] W. Ding, L. He, G. Zhao, H. Zhang, Z. Shu and D. Gao, *Double porous media model for mass transfer for hemodialyzers*, Int. J. Heat Mass Trans. **47** (2004), 4849–4855.

[5] S. Eloot, D. de Wachter, I van Tricht and P. Verdonck, *Computational flow modeling in hollow-fiber dialyzers*, Artif. Organs **26** (2002), 590–599.

[6] M. Galach, A. Ciechanowska, S. Sabalinska, J. Waniewski, J. Wojcicki and A. Wernynski, *Impact of convective transport on dialyzer clearance*, J. Artif. Organs **6** (2003), 42–48.

[7] R.E. Norden and K. Schindhelm, *Design of hollow fiber modules for uniform shear elution affinity cell separation*, Artif. Organs **21** (1997), 107–115.

[8] T. Osuga, T. Obata, H. Ikehira, S. Tanda, Y. Sasaki and H. Naito, *Dialysate pressure isobars in a hollow-fiber dialyzer determined from magnetic resonance imaging and numerical simulation of dialysate flow*, Artif. Organs **22** (1998), 907–909.

[9] S. Baigent, M. Williams, A. Marks, M. Penney, J. Wattis, P. Howell, J. King, and J. Chapman, *Mathematical modelling of profiled haeomodialysis*, 1st Mathematics in Medicine Study Group, Nottingham, 2000.

[10] M. M. Ursino, L. Coli, M. Grilli Ciciloni, V. Dalmastri, A. Guidicissi, P. Masotti, G. Avanzolini, S. Stefoni, and V. Bonomini, *A single mathematical model of intradialytic sodium kinetics:* ˆin vivo validation during hemodialysis with constant or variable sodium, Int. J. Artif. Organs **19** (1996), no. 6, 393–403.

[11] F. Yan, P. Dejardin, A. Schmitt and C. Pusineri, *Electrochemical characterization of a hemodialysis membrane*, J. Phys. Chem. **97** (1993), 3824–3828.

[12] L. Coli, M. Ursino, A. De Pascalis, C. Brighenti, V. Dalmastri, G. La Manna, E. Isola, G. Cianciolo, D. Patrono, P. Boni, and S. Stefoni, *Evaluation of Intradialytic Solute and Fluid Kinetics: Setting Up a Predictive Mathematical Model*, Blood Purif. **18** (2000), 37–49.

[13] W. Krebs and W. Pickl, *A Mathematical Model of Hemodialysis*, in Modelling, Analysis, and Optimization of Biosystems, Springer, Berlin, 2007, pp. 141–183.

[14] F. Locatelli, C. Manzoni, and S. Di Filippo, *Electrolyte Balancing: Modern Techniques and Outcome*, Blood Purif. **19** (2001), 195–199.

[15] Ronald L. Fournier. *Basic Transport Phenomena in Biomedical Engineering* (2nd Ed.), Taylor &Francis, 2007.

[16] D.A. Saville. *Electrohydrodynamics: The Taylor–Melcher Leaky Dielectric Model*, Ann. Rev. Fluid Mech. **29** (1997), 27–64.

[17] K. Yamamoto, M. Hayama, M. Matsuda, T. Yakushiji, M. Fukuda, T. Miyasaka, K. Sakai, *Evaluation of asymmetrical structure dialysis membrane by tortuous capillary pore diffusion model*, Journal of Membrane Science **287** (2007), 88–93.

Mathematical Models for Estimating the Risk of vCJD Transmission

Problem Presenters: Mustafa Al-Zoughool (University of Ottawa) and Susie El Saadany (Public Health Agency of Canada)

Contributors: Vahid Anvari (York University), Mahshid Atapour (York University), Lydia Bourouiba (York University), Luz Angélica Caudillo Mata (CIMAT—Center for the Mathematical Research), Shannon Collinson (York University), Venkate Duvvuri (York University), Hongbin Guo (York University), Angella Johnson (University of Southern California), Neal Madras (York University), Peter Miasnikof (University of Toronto), Lilia L. Ramírez Ramírez (University of Waterloo), and Ivete Sánchez-Bravo (CIMAT—Center for the Mathematical Research).

Report prepared by[1]**:** V. Anvari, M. Atapour, L. Bourouiba, L. A. Caudillo Mata, S. Collinson, A. Johnson, N. Madras, P. Miasnikof, L. L. Ramírez Ramírez, I. Sánchez-Bravo.

1 Introduction

Transmissible spongiform encephalopathies (TSE's), also known as prion (proteinaceous infectious particles) diseases, are a group of fatal brain diseases that affect both animals and humans. They are characterized by long incubation periods, spongiform changes, and astrogliosis.

Infective prions propagate by refolding into abnormal structures which cause the conversion of normal protein molecules into the abnormally structured forms. These prions (TSE agents) are resistant to inactivation by conventional decontamination methods. They also resist all routine sterilization procedures commonly used in health care facilities. Because of the unconventional transmissions of these agents, they are of particular concern for public health.

Variant Creutzfeldt Jakob Disease (vCJD) is a human form of Bovine (Transmissible) Spongiform Encephalopathy or mad cow disease. Variant CJD is an infectious disease

---

[1]`anvari@mathstat.yorku.ca, atapour@mathstat.yorku.ca, lydia.bourouiba@math.mit.edu,`
`langel@cimat.mx, mscolli@yorku.ca, angelajo@usc.edu, madras@mathstat.yorku.ca,`
`p.miasnikof@utoronto.ca, llramire@uwaterloo.ca, ivete@cimat.mx`

typified by long incubation periods and asymptomatic infections—two factors making epidemiological investigations particularly difficult. Two modes of infection of vCJD have been identified:

- Primary infections: associated with the ingestion of infectious materials (mainly BSE-contaminated beef),
- Secondary infections: associated with receiving blood from an infected blood pool (particularly through transfusions) and with the use of infected surgical instruments.

The number of cases of vCJD is relatively small, but its characteristic incubation period coupled with unconventional transmissibility has presented a challenge for parameter estimation and modeling dynamics. In spite of the fact that only one vCJD case has been detected in Canada (in 2002) it is important to study possible transmission scenarios. Indeed, outbreaks can potentially develop into epidemics, as the outbreak in UK (in the 1990's) has shown.

Since the epidemic course shows geographical differences, every country should assess its specific vCJD risk as a condition for developing a national blood supply strategy. A group was formed for this purpose in Germany in 2001, and its findings are available in [16].

To prevent secondary transmission through blood components, several countries have started to exclude recipients of blood transfusions from being donors. A recent study [7] investigated the effectiveness of this measure using a dynamic age-structured model based on German epidemiological data. An important question for us is whether Canada should ban recipients of blood transfusions from donating blood. On the one hand, this ban could prevent some new cases of the terrible disease vCJD; on the other hand, it would significantly decrease the number of blood units collected by Canadian Blood Services. To help us choose between these alternatives, we would like to predict the number of new vCJD cases that would be prevented if Canada were to enact this ban.

In this report, we use two models to describe the plausible evolutions of vCJD outbreaks in Canada. In the next two sections, these models and their underlying assumptions are thoroughly discussed. In Section 2 we use a classical compartmental model to describe the evolution of the infected population originated from primary infections and secondary infections. We examine possible parameter values and scenarios based on data. The roles of the two key transmission parameters are examined. Section 3 explores a stochastic model that could help predict the consequences of a vCJD-infected individual entering the Canadian blood-donor pool. Both simulation and analytical results are presented. Some brief concluding remarks appear in Section 4.

2 A Deterministic Model

The first basic deterministic time-continuous compartmental models to describe the transmission of communicable disease are contained in a sequence of three papers by Kermack and McKendrick in 1927, 1932 and 1933 [10]. These models have been generalized and a recommended introduction to the topic is provided in the first two chapters in [2].

The deterministic compartmental model can be directly translated into a Markovian stochastic version by reformulating the ordinary differential equations that describe the deterministic dynamics, as the transition probabilities $(+o(dt))$ of the process. In this underlying stochastic model the process has latent (if considering an SEIR model) and infectious periods that are exponentially distributed.

In this section we only explore the deterministic version of the vCJD infectious dynamics considering primary and secondary infections (via blood transfusion) and the sensitivity of outbreak to the change of some parameter values.

The analysis in this section aims to study the general characteristics and rough uncontrolled outbreak scenarios derived from infections by food intake and blood transfusion. The number of infected individuals is obtained in the long term with the purpose of exploring the evolutionary epidemic trends rather than forecasting outbreak outcomes.

2.1 Model. The population is subdivided into susceptible $S(t)$, primary infected (by beef consumption) $I_1(t)$, secondary infected (by blood transfusion) $I_2(t)$, and removed $R(t)$ individuals.

Compartmental models assume that individuals in the entire population mix homogenously, so the rate of interaction between two different subsets of the population is proportional to the product of the number in each subset.

Regarding the vCJD transmissibility in the infectious process, if we have an almost completely susceptible population we suppose that each infected beef cow infects β_1 individuals and that each infected individual annually transmits vCJD to β_2 individuals by blood transfusion.

We also assume that every individual becomes infectious immediately after being infected by either ingesting contaminated beef or receiving infected blood. This, added to the fact that individuals die just a few weeks or months after presenting vCJD symptoms, makes the infectious periods very similar to the illness's latent periods. Here we consider the two kinds of periods as equal.

We include two different incubation periods for primary and secondary cases. In both cases the periods are exponentially distributed but with means $1/\gamma_1$ and $1/\gamma_2$, respectively.

Due to the fact that the evolution of vCJD is long, it is important to introduce the demographical changes that occur in a population. The two demographical variables that we consider in this section are the births and deaths. We respectively denote as π and δ the crude annual birth and death rates in Canada.

Let $N(t)$ be the total population at time t. Since vCJD is a fatal disease, then $N(t) = S(t) + I_1(t) + I_2(t)$. Therefore the interactions of our compartmental model are depicted by Figure 1 and it is formalized by the following differential equations:

$$\frac{dS}{dt} = \pi N - \frac{\beta_1}{N}SC - \frac{\beta_2}{N}S(I_1 + I_2) - \delta S, \tag{2.1}$$

$$\frac{dI_1}{dt} = \frac{\beta_1}{N}SC - \gamma_1 I_1 - \delta I_1, \tag{2.2}$$

$$\frac{dI_2}{dt} = \frac{\beta_2}{N}S(I_1 + I_2) - \gamma_2 I_2 - \delta I_2, \tag{2.3}$$

$$\frac{dR}{dt} = \gamma_1 I_1 + \gamma_2 I_2, \tag{2.4}$$

where C is the number of BSE infected beef cases in Canada in a year. The term $\beta_1 SC/N$ in (2.1) and (2.2) describes the number of susceptible individuals who acquire vCJD by eating BSE infected meat. When $S \sim N$ then this number is equal to $\beta_1 C$ as described above. The expression $\beta_2 S(I_1 + I_2)/N$ in (2.1) and (2.3) describes the number of new infections by blood transfusion from infected individuals (either primary or secondary cases). Then if $S \sim N$ each infective originates β_2 new cases.
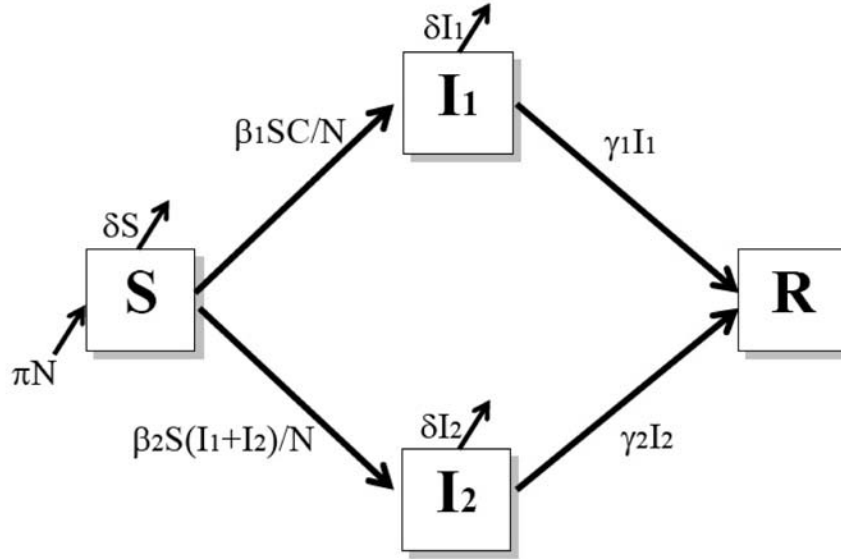
Figure 1 Interactions of the deterministic compartmental model.

2.2 Parameters. Now we discuss the parameter values used to describe the infectious dynamics. Some infectious scenarios are explored in Section 2.4 by varying some of the parametric values.

Since 1993, one percent of the cattle have been tested in Canada and only 18 have been found to be infected with BSE [4]. On the other hand, according to *Canada Livestock and Products Annual 2007* [17], approximately 3,825,000 heads are slaughtered in Canada every year. If we assume that the 18 infected animals were uniformly found during these 16 years and that beef consumption over this period has been approximately equal to the 2007 levels, then the number of BSE cases during a year is close to $\hat{C} = 3,825,000 \times \alpha = 112.5$, where α is the estimated fraction of infected heads ($\alpha = 2.94 \times 10^{-5}$).

As stated in [15], the annual Canadian beef consumption in recent years has been approximately 23.3 kg per person. We know that a single animal provides between 140 and 200 kg of edible meat. Consequently, we calculate that a single BSE infected bovine can contaminate between 700 (140 kg/200 grams per meal portion) and 6,667 (200 kg/30 grams per meal portion) individuals. If we assume that each bovine provides 170 kg of edible meat and the individual portions are 65 grams (64.7 grams per day = 23.3 kg /360 days), the number of individuals infected by one diseased bovine would be 2,615.

Because the most dangerous parts of the animal are now eliminated from human consumption (those that contain sections of the central nervous system), the probability that an individual acquires vCJD by consuming meat from an infected animal decreases by half. Hence $\hat{\beta}_1 = 1,307$. In the next section we will explore some other values for this parameter.

In order to estimate β_2, we use a case study from Britain where 4 out of a total of 66 individuals who had received blood from a blood pool contaminated by a single infected
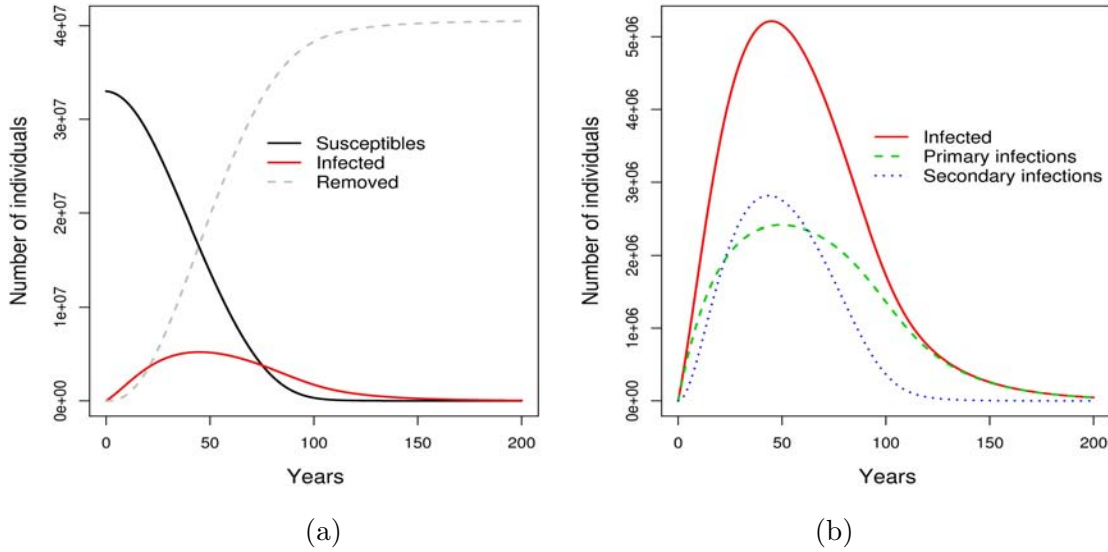
Figure 2 Epidemic curves, (a) evolution of outbreak in Canada, (b) as in (a) except individuals are separated into primary and secondary infections.

donor contracted vCJD after their transfusion. Even though the donor pool size can vary, the number of affected individuals may remain similar due to factors such as dilution of the particles that transmit the disease (see [6]). We consider that the number of infected individuals originated from a single infected person who donates blood is constant and equal to 4.

Now, we also have that the fraction of people that donated blood in Canada in 2007 was 1/60, [3], and from those individuals 335,000 donated once, 90,000 donated twice, 110,500 donated between 3 and 5 times, and 14,500 donated 6 or 7 times during the year. Thus the expected number of times that the same individual gives blood in a year, is approximately 1.91. Hence the estimated new cases an infected individual originates in one year is $\hat{\beta}_2 = 2/60 \times 4 = 0.1333$.

The estimated incubation periods in individuals that acquired vCJD by eating contaminated beef and blood transfusion has been estimated to be between 13 and 40 years and between 5 and 6 years, respectively. Using the midpoints of these intervals we have

$$\hat{\gamma}_1 = \frac{1}{26.5} = 0.03773 \qquad \text{and} \qquad \hat{\gamma}_2 = \frac{1}{5.5} = 0.181818.$$

From the demographical information in [14] we obtain the crude birth and death rate registered in 2007-2008:

$$\hat{\pi} = \frac{11.1}{1000} = 0.0111 \qquad \text{and} \qquad \hat{\delta} = \frac{7.2}{1000} = 0.0072.$$

2.3 Outbreak Evolution. Assuming that the parameters remain similar every year, the evolution of the outbreak in Canada (population with 33 million people) is as presented in Figure 2 (a). Here we assume that a single case by secondary infection is present at time 0.
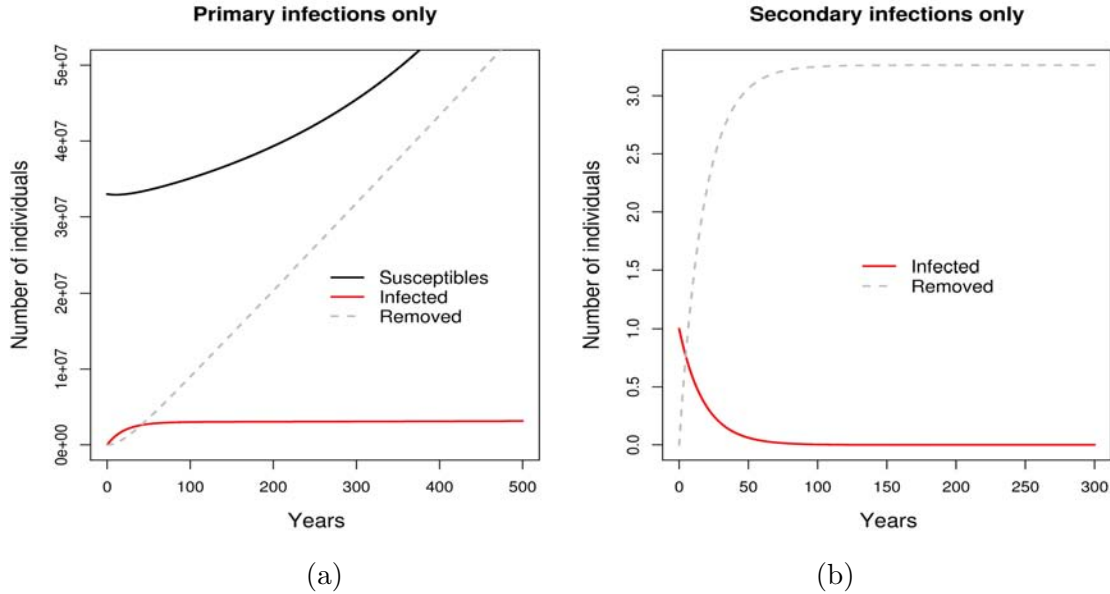
Figure 3 Epidemic curves for the cases of (a) primary and (b) secondary infections.

As shown in Figure 2(a), the epidemic curve reaches its peak at around year 50. While the number of infected individuals remains always less than 5,250,000, by year 200 the number of susceptible individuals decreases to the value of 162. Due to the natural population growth the total number of individuals that die with vCJD symptoms is 40 million.

Figure 2(b) decomposes the total number of infected according to primary and secondary infections. These two curves reach their peaks in the same year. As we will see, this is due to the fact that the incidence of secondary infections follows the incidence of primary infections, and both combined decrease the susceptible population to a level that causes the abrupt decrement in the number of infected cases after year 50.

To understand the interaction of the cases by primary and secondary infections in the outbreak we obtain the outbreak evolution considering that the vCJD can only be acquired by ingesting BSE infected meat (Figure 3(a)), and that infection can only be acquired by blood transfusion (Figure 3(b)).

In the first case we have a rapid increment in the vCJD incidence, and by year 100, 3.01 million people live with vCJD. After this date the increment is steady but slow. By year 500, the number of infected individuals is 3.148 million, and in spite of the fact that the susceptible population increases, a total of 55 million people would have died with vCJD symptoms.

Based on Figure 3(a) we can conclude that the infectious and removal rate (β_1 and γ_1), combined with the fixed birth and death rates would result in the event of vCJD becoming endemic in the population.

In contrast, under the second scenario (Figure 3(b)) we have that the outbreak dies out immediately after starting, affecting only 4 individuals. According to the model, an outbreak originated by secondary transmissions will remain small and this is explained by its basic reproductive number.
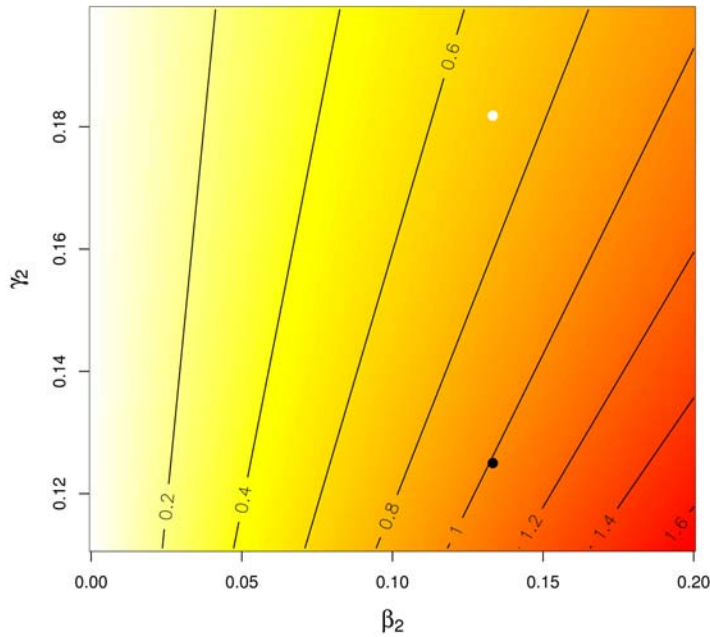
Figure 4 Basic Reproductive Number.

The basic reproductive number ($\mathcal{R}_0$) is defined as the (expected) number of secondary infections produced by an infective individual in a fully susceptible population [1]. This epidemic parameter is used to estimate the size of the population that is infected during an outbreak (final outbreak size). In a deterministic model, if $\mathcal{R}_0 < 1$ an outbreak affects only a reduced number of individuals but an epidemic will always develop if $\mathcal{R}_0 > 1$.

Based on this model, the basic reproductive number for secondary vCJD infections is

$$\mathcal{R}_0 = \frac{\beta_2}{\gamma_2 + \delta}.$$

For the values of $\beta_2 = 0.1333$, $\gamma_2 = 0.1818$ and $\delta = 0.0072$, the basic reproductive number is $0.7054 < 1$ (white dot in Figure 4). Consequently, in the absence of primary infections, all vCJD outbreaks would affect only a handful of individuals.

In order to better understand the sensitivity of this basic reproductive number in terms of β_2 and γ_2, we present the level curves of $\mathcal{R}_0$ in Figure 4. While the parameter β_2 can be modified with criteria that exclude vCJD exposed blood donors, the parameter γ_2 is directly linked to the evolution characteristics of infectious agents in the host. As depicted in Figure 4 the larger the value of β_2 the more sensitive $\mathcal{R}_0$ is to the changes in the incubation period. Considering incubations larger than 6 years, it is notable that for $\beta_2 = 0.1333$ (as before), the epidemic threshold $\mathcal{R}_0 = 1$ is reached for an incubation period of just 8 years ($\gamma_2 = 0.125$, black dot in Figure 4).

In 2002 one vCJD case was detected in Canada and no other case has been identified since then. The discrepancy between the observed and theoretical trends for outbreaks can be due to several reasons such as the effectiveness of the implemented control measures.

Table 1 Parameter values for the different scenarios.

values for β_1		values for β_2	
0.0000	697.0700	0.0000	0.4267
87.1330	784.2000	0.0533	0.4800
174.2700	871.3300	0.1067	0.5333
261.4000	958.4700	0.1600	0.5867
348.5300	1045.6000	0.2133	0.6400
435.6700	1132.7000	0.2667	0.6933
522.8000	1219.9000	0.3200	0.7467
609.9300	1307.0000	0.3733	0.8000

This male (under the age of 50), had multiple stays in the UK during the BSE outbreak and once classified as vCJD suspected, Health Canada immediately advised the hospital to remove from service the medical devices that were in contact with this person, until such time as a diagnosis be confirmed. Once the individual was confirmed with vCJD (through autopsy) the identified individuals who were exposed to the medical devices were advised not to donate blood, organs or tissue.

Another factor that can lead to an overestimation of the transmissibility by food intake is the actual existence of a non negligible latent period in beef cows, during which the animals are infected but not infectious.

2.4 Interaction of primary and secondary infections. With the aim to further study the impact of the interaction between β_1 and β_2 in the outbreaks, we construct a grid where we evaluate the function

$$f(\beta_1, \beta_2) = \sum_{t=0}^{m} \left(S_{(0,0)}(t) - S_{(\beta_1, \beta_2)}(t) \right),$$

where $S_{(0,0)}(t)$ and $S_{(\beta_1, \beta_2)}(t)$ are the number of susceptible individuals in the population at day $t = \{0, 3.6, 2(3.6), \ldots, n(3.6), \ldots, m = 50001(3.6) \sim 500 \text{ years}\}$, when no transmission can occur ($\beta_1 = \beta_2 = 0$) and when the vCJD outbreak has parameters (β_1, β_2), respectively. This function is a measure of the outbreak severity and when it is evaluated in the grid with parametric values in Table 1, it can be depicted as in Figure 5. Here $f(\cdot, \cdot)$ is divided by 1×10^{12}.

As we can observe in Figure 5, when outbreaks are only due to primary infections, they tend to become epidemics very slowly as β_1 increases (first line in Figure 5(b)); however, combined with secondary infections, even modest increments of β_2 produce large outbreaks even for relatively small β_1.

In contrast, outbreaks due solely to secondary infections tend to be small for values of $\beta_2 < 0.19$. This is in agreement with the threshold value for the basic reproductive number and Figure 4 (when drawing a horizontal line at level of white dot). From Figure 5(a) we see that adding primary infections affects the value of $f(\cdot, \cdot)$ for $\beta_2 < 0.19$ but does not significantly increases the final epidemic size when the outbreaks are already developing into epidemics.

2.5 Discussion and Future Work. The first and largest vCJD outbreak occurred in the UK between 1995 and 2008 (with death prevalence peak during 1998/2000 [11]), but since then the disease incidence is rare. This last fact is to be celebrated, but unfortunately

(a)   (b)
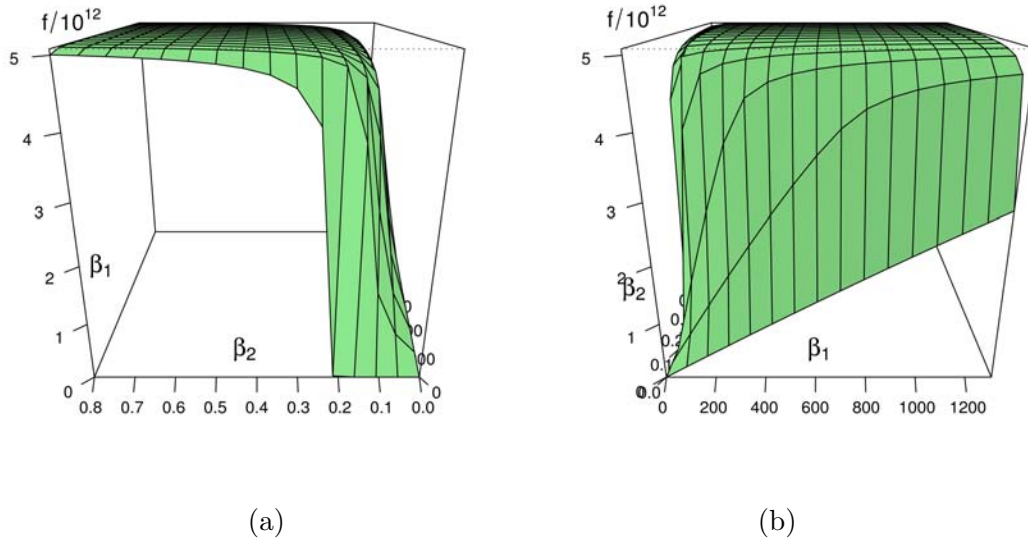
Figure 5 Two views of $f(\beta_1, \beta_2)/\left(1 \times 10^{12}\right)$

has led to the problem of not having enough information to fully understand and estimate the human transmission risks and the individual evolution of the illness. From the epidemiological point of view it is important to analyze the dynamics of vCJD to be able to rule in or out certain scenarios and evaluate the impact of control measures.

The first challenge that scientists have to face in order to refine their models is to improve the estimates of the parameters for the different transmission paths. The parameter estimation should also include the estimation for the exposed and infectious periods that animals and humans present when infected by each route.

The model presented here can also become more realistic by considering the specific rates that now are describing the population as one with homogeneous individuals. First, we can introduce the specific birth and death rates by sex and age (or age group, also called cohorts) to model the natural population growth over time. Second, since the probability of receiving/donating blood can significatively vary according to sex and age, it is desirable to incorporate the specific blood exchange for these groups.

The epidemic model in this section can also be generalized by introducing other secondary infections such as those derived from surgical cross contamination (as in [8]) and organ transplants. These two events can be closely related to blood transfusion but they may modify the probability of vCJD transmission.

In laboratory experiments, an epidemiologist may obtain more information about the impact of the pool blood size for the vCJD transmission and based on this new information update the blood transmission parameter that here we have considered fixed.

Since the outbreak size for the transmission via blood transfusion appears to be very sensitive to the incubation periods (Figure 4), the epidemic threshold ($\mathcal{R}_0 = 1$) may also be very sensitive to the asymmetry present in the incubation (and/or latent) period distribution. The authors of [8] estimated that the incubation-latent period for individuals that acquired vCJD via surgery is a random variable with gamma distribution. The model in [8]

is a compartmental model as the one presented here, and the authors introduce the gamma distribution for the incubation period adding as many stages in this period as the estimated gamma distribution.

Due to the fact that the vCJD latent period is long, it is important to incorporate the demographical changes over time. The model introduced here takes into account the crude birth and death rates, but it is important to incorporate as well the migration of susceptible and infected individuals.

The value of the model presented here lies in the ability of drawing general epidemic trend characteristics, but in order to predict the number of infected individuals (or susceptible or removed individuals) at a certain point in time it is not only necessary to obtain the forecasted specific rates (birth, death, migration, transfusion, beef consumption, etc.) but it is also important to incorporate the distribution of latent and incubation periods, and provide a measure of uncertainty to the predicted number (such as confidence intervals).

Finally, the stochastic model obtained after incorporating the illness stage distribution and infectious rates, can also become more realistic by relaxing the assumption that each individual in the same age-sex group is equally likely to be infected during an outbreak. The existence of "superspreaders" (such as individuals that donate blood significantly more times during a year) can importantly modify the outbreak evolution and the impact of control measures [12, 13, 5].

3 A Stochastic Model and Simulation

In this section we present a stochastic model, developed to help us better understand and forecast the dynamics of secondary vCJD infections through blood transfusions. The assumptions and computations that led to the numerical values for the model's parameters are discussed thoroughly in the following sections.

Our model provides a simple probabilistic representation of the blood-donor system, using conditional probabilities. It revolves around the following parameters:

- The probability of an individual donating blood
- The probability of contracting the disease after receiving a transfusion of contaminated blood
- The attrition (or mortality) rate of the infected population

It is possible to estimate the probability of an individual donating blood, from data collected by the Canadian Blood Services. In fact, the data allows us to estimate probabilities of an individual being a first-time and a repeat blood donor. Of particular relevance for our model is the fact that an individual who has donated in the past year has a higher probability of donating than an individual who has not. Past studies also provide clues on the rates of secondary transmission given an exposure to contaminated blood products.

We model the available parameters using conditional probabilities and build an iterative process to study the dynamics of the blood-donor system.

The parameters of our system include the probability of blood donation by an individual (see Table 2), the probability of contracting the disease upon receiving contaminated blood through a blood transfusion $P(c)$, and the attrition (or mortality) rate of an infected individual m. We define the attrition rate to include both the removal of an infected individual from the donor population due to the appearance of vCJD symptoms and the natural mortality. Using these parameters an iterative process was constructed to assess the effects of an infected individual on the Canadian blood-donor population.
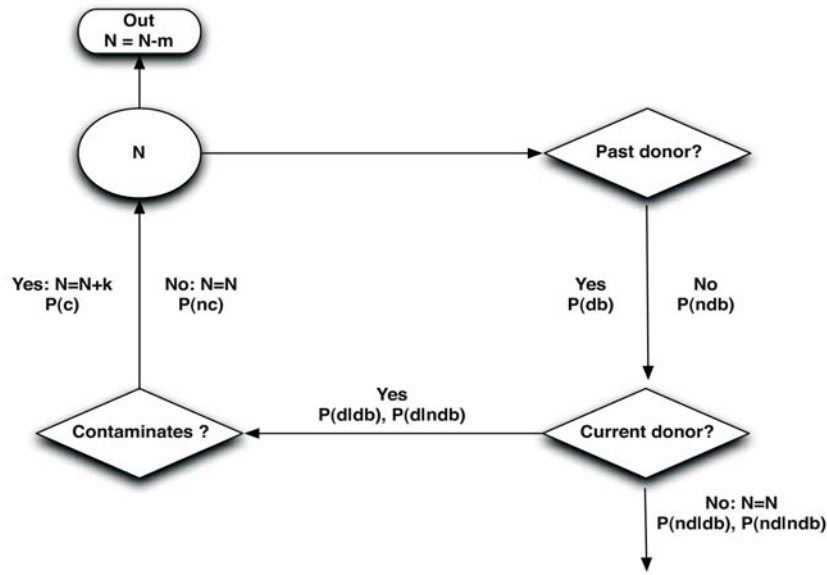
Figure 6 Flowchart of the algorithm with input and output variables given in Table 2.

The algorithm is explained in terms of the input and output parameters in Table 2, and its flowchart is displayed in Fig. 6.

The steps of the algorithm are as follows:

- **Step 0:** Introduce one infected individual into the blood-donor pool and set the number of infected individuals to be $N = 1$.

  As long as $t \leq T$ the following steps are performed in a loop as required to collect M samples of the count N.
- **Step 1:** Assess whether an individual was a past donor:
  - Assign the probability $P(db)$ for the individual of having donated in the past

Table 2 Input and output variables of the algorithm.

Input	
T	Duration of the simulation
$P(d\|db)$	Probability of an individual to donate blood
	given at least one previous donation
$P(nd\|db)$	Probability of an individual not donating blood
	given at least one previous donation
$P(d\|ndb)$	Probability of an individual donating blood
	given no previous donation
$P(nd\|ndb)$	Probability of an individual not donating blood
	given no previous donation
m	Mortality or attrition rate of infected individuals in the pool of donors
Output	
N	Number of infected individuals, in the pool of potential donors

  – Assign the probability $(1 - P(db))$ for the individual not having donated in the past
- **Step 2:** Determine if an individual donates at the current time

  If the individual has donated in the past:
  – Assign the probability $P(d|db)$ of donating
  – Assign the probability $P(nd|db) = 1 - P(d|db)$ of not donating

  If the individual is not a past donor:
  – Assign the probability $P(d|ndb)$ of donating
  – Assign the probability $P(nd|ndb) = 1 - P(d|ndb)$ of not donating
- **Step 3:** Determine if a donor contaminates one or more others
  – Assign the probability $P(c)$ of contaminating:
    * Compute the number of secondary contaminations C
    * Increment the number of infected individuals by $N = N + k$
  – Assign the probability $1 - P(c)$ of not contaminating:
  No further action
- **Step 4:** Compute the attrition in the pool of infected potential donors

$$N = N - mN$$

3.1 Numerical results and scenario analysis. Using the algorithm presented above, we ran our simulation over a (simulated) duration of 15 years, the approximate time over which individuals remain donors. Simulations were done using a 6-month time-step and iterated 30 times ($T = 30$). Finally, we repeated the whole process 10,000 times ($M = 10,000$).

The results are reported in Table 3.1 and in Figure 7. We see that the expected (mean) number of infected individuals in the pool of potential blood-donors begins with a value of 1 (by construction) and decreases to approximately zero, over the simulation period.

Table 3 Mean number of infected individuals in the potential donor pool and its standard deviation (Stdev.) with time.

Time	Mean	Stdev.	Time	Mean	Stdev.
1	1	0	16	0.1039	0.3051
2	0.8545	0.3526	17	0.0885	0.284
3	0.7373	0.4401	18	0.0763	0.2655
4	0.6354	0.4813	19	0.0664	0.249
5	0.5448	0.498	20	0.0586	0.2349
6	0.4654	0.4988	21	0.0493	0.2165
7	0.3992	0.4898	22	0.0425	0.2017
8	0.3393	0.4735	23	0.0363	0.187
9	0.2897	0.4536	24	0.0312	0.1739
10	0.2465	0.431	25	0.0266	0.1609
11	0.2102	0.4075	26	0.0231	0.1502
12	0.1813	0.3853	27	0.0197	0.139
13	0.1559	0.3628	28	0.0164	0.127
14	0.1311	0.3375	29	0.0139	0.1171
15	0.1191	0.3239	30	0.0161	0.1423
			31	0	0
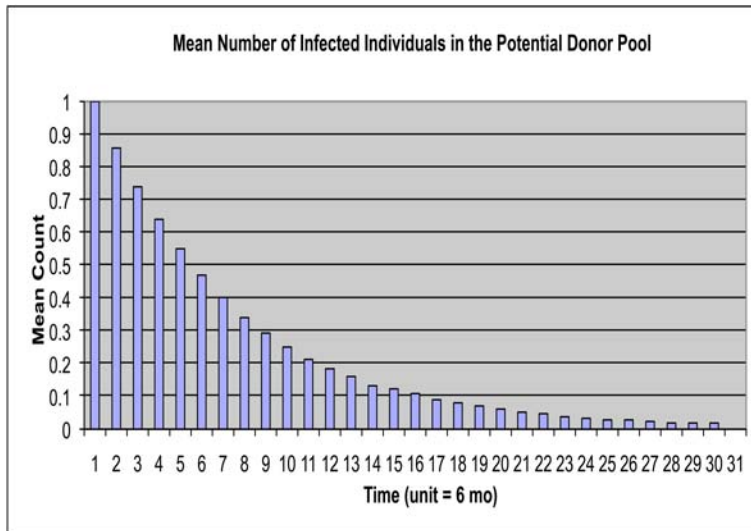
Figure 7 Number of infected individuals in the pool of potential donors
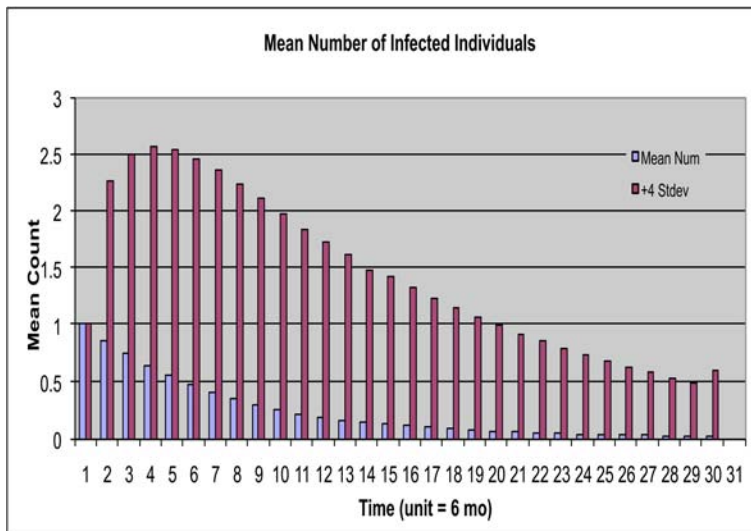
Figure 8 Number of infected individuals and results from the worst-case scenario

To better assess the potential effect of an infected donor entering the Canadian blood-donor pool we examined a "worst-case scenario", using the model presented above. The "worst-case" number of contaminated was defined as the mean number of infected individuals plus four standard deviations. This is a highly unlikely outcome, with a probability of occurring in the order of 10^{-5}, under the assumptions of our model. (Under the normal distribution, the probability of exceeding the mean by at least 4 standard deviations is of the order of 10^{-5}, i.e. 1-F(4) for the normal N(0,1).)

The results are shown in Figure 8. The *worst-case* estimate begins with $N = 1$ (by construction the standard deviation is 0) and attains a peak at approximately 2.5 individuals, after 2 years. The number of infected individuals then decreases over the remaining simulation period, except for a negligible increase in the 30th time-step.

The preliminary results for both the "mean" and "worst-case" scenarios suggest that the effect of an infected individual entering the blood-donor pool would be negligible on the total number of vCJD infections in the overall population. However, future work should focus on estimating the parameters and empirically validating the underlying assumptions of the model. Only then will we be able to rigorously evaluate the risk of vCJD transmissions and draw more complete conclusions.

3.2 Analysis of the Stochastic Model. In this section we present an analysis of the stochastic model described earlier in this section. The analysis will be based on a branching processes formulation.

Consider a single primary vCJD case (a person who acquired vCJD by eating meat infected with BSE). How many secondary cases of vCJD will occur as the result of blood transfusions from this primary case? (We shall count all secondary cases over all times after the primary infection occurs; we do not restrict the count to a single time period.) Some individuals may get vCJD by blood transfusion directly from the primary case; we shall say that such individuals comprise the "first generation" of secondary infections. Individuals in the first generation of secondary infections may donate blood to others, who may acquire vCJD as a result; we shall say that these people comprise the "second generation" of secondary infections. In general, for $k = 1, 2, \ldots$, individuals in the kth generation may donate blood to others, and those people who acquire vCJD by transfusions from people in the kth generation comprise the $(k + 1)^{th}$ generation of secondary infections. We wish to study the total number of all of the secondary infections.

To formalize our model, we now define some random variables. Let N_0 denote the number of people who receive blood transfusions from our single primary infected person during his/her lifetime (after he/she becomes infected). Let p be the probability that a single transfusion from an infected person to a second person causes the second individual to become infected. For each $k = 1, 2, \ldots$, let X_k denote the number of secondary infections in the kth generation. Then X_1 has the binomial distribution with parameters N_0 and p; we shall represent this by writing

$$X_1 \; = \; \mathrm{Bin}(N_0, p) \,. \tag{3.1}$$

(Note that this is a generalization of the usual definition of binomial distribution, since N_0 is a random variable instead of a constant. It is more correct to say that the conditional distribution of X_1 given the value of N_0 is binomial with parameters N_0 and p.)

Now consider people who receive transfusions from a given individual with secondary infection. The pattern of blood donation is different from that of our primary case, since people who receive transfusions are not a "typical" group within the population—e.g., they tend to be older and in poorer health. For a single person who has received a transfusion, the random variable N_T shall denote the number of people who receive blood transfusions from this person during his/her lifetime (subsequent to this person receiving the transfusion).

Formally, we can express the random variables X_k ($k > 1$) recursively as follows:

$$X_k \; = \; \mathrm{Bin}\left(\sum_{i=1}^{X_{k-1}} N_T^{(k-1,i)}, \, p\right) \tag{3.2}$$

(where $\{N_T^{(j,i)}\}$ are independent, identically distributed copies of N_T; $N_T^{(j,i)}$ represents the number of recipients of transfusions from the ith person in the jth generation of secondary cases). Finally, let Y be the total number of secondary cases that are ultimately due to our initial infected primary individual. Then

$$Y \; = \; X_1 \, + \, X_2 \, + \, X_3 \, + \, \cdots \tag{3.3}$$

It is routine to show that the expected values of the above random variables satisfy

$$E(X_1) \; = \; p\, E(N_0) \tag{3.4}$$

and that

$$E(X_k) \; = \; p\, E(X_{k-1})\, E(N_T) \quad \text{for } k > 1. \tag{3.5}$$

It follows that

$$E(X_k) \; = \; [p\, E(N_T)]^{k-1}\, E(X_1) \; = \; p^k\, [E(N_T)]^{k-1}\, E(N_0), \quad \text{for } k \geq 1, \tag{3.6}$$

and that the expected total number of secondary infections (recall (3.3)) is

$$E(Y) \; = \; \sum_{k=1}^{\infty} E(X_k) \; = \; \frac{p\, E(N_0)}{1 \, - \, p\, E(N_T)}. \tag{3.7}$$

Public health officials may consider the policy of preventing any recipient of a blood transfusion from themselves donating blood. To assess the possible impact of such a policy, we shall calculate the number of secondary infections that could have been prevented with such policy. The first generation of secondary infections are not preventable in this way, but all subsequent generations of secondary infections are. The total number of infections preventable in this way (per primary infected individual) is $Y - X_1$, and its expected value is

$$E(Y - X_1) \; = \; E\left(\sum_{k=2}^{\infty} X_k\right) \; = \; \sum_{k=2}^{\infty} [p\, E(N_T)]^{k-1} p\, E(N_0) \; = \; \frac{p^2\, E(N_0)\, E(N_T)}{1 \, - \, p\, E(N_T)}. \tag{3.8}$$

Now we consider estimates for the values of p, $E(N_0)$, and $E(N_T)$.

For p, we use British data, in which 4 out of 66 known individuals developed vCJD after having received transfusions from a vCJD-infected donor. (The data is not perfect, because some recipients may have developed vCJD after being surveyed, and some may have acquired vCJD by other means.) This gives us the simple point estimate $\hat{p} = 4/66 = 0.061$. Even assuming that the data is perfect, we can ask for a 95% confidence bound for p. In other words, for what values of p is it true that $\Pr\{\,\mathrm{Bin}(66, p) \leq 4\,\} \geq 0.05$? It turns out that the largest such p is about 0.133. Therefore a 95% confidence bound on p is "$p \leq 0.133$."

For $E(N_0)$, we use the following information from the web pages of Canadian Blood Services (http://www.blood.ca; > Media Room > Resource Center > Quick Facts):

(*i*) about 3.7% of Canadians donate blood at some point in their lives. This says that about 1.2 million Canadians ever donate blood.

(*ii*) There are about 450,000 active donors in Canada (about 1.4% of the population).

(*iii*) About 900,000 units of blood are donated annually in Canada.

(*iv*) A unit of blood can go to up to three recipients.

(*v*) Each active donor gives an average of 2.18 units per year.

We use the above information to obtain a rough estimate of $E(N_0)$ (a better estimate can be obtained by a more careful analysis of available data from Canada Blood Services and Héma-Québec), as follows. Of the 1.2 million Canadians who ever donate blood, some are currently active donors and some are not. If L is the lifetime average number of units given by one donor, then in a given year the average amount given by one donor is $L/80$, where we have used 80 years as the average lifetime of one donor. (Of course, active donors will tend to give more than this, and inactive donors will give nothing, but the average will be $L/80$.) Therefore Canadians give about $1,200,000 \times L/80$ units per year; by (*iii*), this number equals 900,000, so we deduce that $L \approx 60$. In view of item (*iv*) above, we shall assume that each unit goes to an average of two recipients. Therefore the expected number of recipients of transfusions from a single person is

$$
\begin{aligned}
E(N_0) &= \left(\begin{array}{c} \text{probability that} \\ \text{the person is} \\ \text{a blood donor} \end{array} \right) \times \left(\begin{array}{c} \text{number of} \\ \text{units} \\ \text{per donor} \end{array} \right) \times \left(\begin{array}{c} \text{number of} \\ \text{recipients} \\ \text{per unit} \end{array} \right) \quad (3.9) \\
&\approx 0.037 \times 60 \times 2 \\
&\approx 4.4.
\end{aligned}
$$
$$\quad (3.10)$$

Finally, for $E(N_T)$, we modify our calculations as follows.

- 53% of transfusion recipients die within 5 years of receiving the transfusion. It seems reasonable to assume that a negligible number of these 53% donate blood after receiving the transfusion (due to age and/or poor health). So among transfusion recipients, we expect that the fraction of future donors is at most 47% of the global proportion of 3.7%, which comes to 1.7%.

- For someone who acquires secondary vCJD by transfusion, the average incubation time (i.e. the time until symptoms appear) is 3 years. We assume that such a person would not donate blood after vCJD symptoms appear. Active blood donors among this group (which is precisely the group that concerns us when it comes to passing along the infection) would give an average of 2.18 units per year (by item (*v*) above) for an average of three years, for a total of about 6.5 units.

Therefore, the analogous calculation to (3.9) is

$$
E(N_T) \approx 0.017 \times 6.5 \times 2 \approx 0.22 \,.
$$

We can now insert the above estimates into (3.7) to give the number of infected secondary cases from one person:

$$
E(Y) = \frac{0.061 \times 4.4}{1 - 0.061 \times 0.22} = 0.27, \quad \text{using } p = 0.061, \quad\quad (3.11)
$$

$$
E(Y) = \frac{0.133 \times 4.4}{1 - 0.133 \times 0.22} = 0.60, \quad \text{using } p = 0.133. \quad\quad (3.12)
$$

Finally, from (3.8) we compute the expected number of cases that would be prevented if all recipients of blood transfusions could be prevented from themselves donating blood:

$$E(Y - X_1) \; = \; \frac{(0.061)^2 \times 4.4 \times 0.22}{1 - 0.061 \times 0.22} \; = \; 0.0037, \quad \text{using } p = 0.061, \qquad (3.13)$$

$$E(Y - X_1) \; = \; \frac{(0.133)^2 \times 4.4 \times 0.22}{1 - 0.133 \times 0.22} \; = \; 0.018, \quad \text{using } p = 0.133. \qquad (3.14)$$

These estimates are much smaller than those in (3.11) and (3.12).

3.3 Conclusions and Future Work. In this section, we created a probabilistic model of the blood-donor system. We then simulated the effect of an infected individual on the entire Canadian blood-donor pool, which we found to be quite small. Analytic results supported this conclusion.

Our preliminary simulation results suggest that an infected individual entering the blood-donor pool would only have negligible effects. As shown in Table 3.1, the expected number of infected individuals in our population never exceeds one. Even in our worst-case scenario, the total number of infected potential donors never exceeds 2.5 (see Figure 8).

The calculations of (3.11)–(3.14) show that each primary infected individual has a significant chance of infecting others by blood transfusion, but the chances are much smaller that a secondary infected individual will infect others. Because only transmissions from secondary individuals could be avoided under a policy that would ban recipients of blood transfusions from donating blood, only a minimal number of cases would be prevented. Indeed, given the small number of primary cases in Canada and the precautions now in place, such a policy may only prevent a few transmissions per century. The concern with implementing such a policy is that it would have a significant impact on the number of eligible donors, which in turn could have serious ramifications for people in need of blood donations.

We must emphasize that although our findings from the stochastic model may seem reassuring, even in the worst-case scenario, they are far from rigorous. Given the very strong assumptions that were required to build our model and the lack of data available to estimate model parameters, it is not possible to draw any definitive conclusions based on our numerical results.

4 Concluding Remarks

We have presented two different simple models for vCJD transmission by blood transfusion. Both models indicate that transfusions alone are unlikely to cause more than a few infections, unless the number of primary cases increases.

To improve our models, future work should pursue data collection, empirical estimation of the model parameters, and examination of the underlying assumptions of our frameworks.

Further improvements could also include examining susceptibility to vCJD infection by age group and iatrogenic infections introduced through surgical instruments. Regarding the latter, it may be worthwhile to conduct experiments to quantify the transmission of prions from an infected surgical instrument after repeated sterilization procedures.

References

[1] R.M. Anderson and R.M. May *Infectious Diseases of Humans*, Oxford University Press, Oxford, U.K., 1991.
[2] F. Brauer, P. van den Driessche and J. Wu (eds.) *Mathematical Epidemiology*, Springer, 2008.

[3] Canadian Blood Services. *http://www.blood.ca/centreapps/internet/*

[4] Center for Disease Control and Prevention *http://www.cdc.gov/ncidod/dvrd/bse/*

[5] R. Cohen, K. Erez, D. ben Avraham and S. Havlin, *Resilience of the internet to random breakdowns*, Phys. Rev. Let. **85** (2000), no. 21, 4626–4628.

[6] Department of Health and Human Services (Assistant Secretary for Legislation). *http://www.hhs.gov/asl/testify/t970731e.html*

[7] K. Dietz *et al.*, *Blood transfusion and spread of variant Creutzfeldt-Jakob Disease*, Emerg. Infect. Dis. **13** (2007), 89–96.

[8] T. Garske, H.J.T. Ward, P. Clarke1, R.G. Will and A.C. Ghani, *Factors determining the potential for onward transmission of variant Creutzfeldt Jakob disease via surgical instruments*, J. R. Soc. Interface **3** (2006), 757–766.

[9] Health Canada. *Classic Creutzfeldt-Jakob Disease in Canada. An infection control guidance.* CCRR 2002 **28S5** (2002), 1–84.

[10] W.O. Kermack and A.G. McKendrick, *Contributions to the mathematical theory of epidemics.* Proc. R. Soc. A **115, 138, 141**, (1927, 1932, 1933), part I, II and III. 700–721,55–83, 94–112.

[11] National Creutzfeldt-Jakob Disease Surveillance Unit *http://www.cjd.ed.ac.uk/.*

[12] M.E.J. Newman, *Spread of epidemic disease on networks*, Phys. Rev. E **66** (2002) 66:016128.

[13] L.L. Ramírez-Ramírez and M.E. Thompson, *The spread of diseases on networks*, (unpublished).

[14] Statistics Canada. *http://www.statcan.gc.ca/.*

[15] Statistics Canada. *http://www.statcan.gc.ca/ads-annonces/23f0001x/hl-fs-eng.htm*

[16] R. Seitz *et al.*, *Impact of vCJD on blood supply*, Biologicals **35** (2007), 79–97.

[17] United States Department of Agriculture, Foreign Agricultural Service http://www.fas.usda.gov/gainfiles/200710/146292635.pdf

List of Participants

Name	Affiliation
Al-Zoughool, Mustafa	University of Ottawa
Anvari, Vahid	York University
Arciero, Julia	University of Pittsburgh
Aruliah, Dhavide	University of Ontario Institute of Technology
Atapour, Mahshid	York University
Azari Rad, Solmaz	University of Toronto
Barralet, Jake	McGill University
Bassett, Dave	McGill University
Begg, Ronald	University of Waterloo
Bohun, Sean	University of Ontario Institute of Technology
Bourouiba, Lydia	York University
Breward, Chris	University of Oxford
Buono, Pietro-Luciano	University of Ontario Institute of Technology
Caudillo Mata, Luz Anglica	Center for the Mathematical Research (CIMAT)
Cerezo, Richard	University of Toronto
Collinson, Shannon	York University
Davoudi, Jahanshah	University of Toronto
Donaldson, Roger	Simon Fraser University
Drapaca, Corina	Pennsylvania State University
Droumeva, Radina	Simon Fraser University
Duvvuri, Venkata	York University
ElSaadany, Susie	Public Health Agency of Canada
Ferguson, Katie	University of Waterloo
Ghaffari, Hamid Reza	University of Toronto
Griffiths, Ian	University of Oxford
Guo, Hongbin	York University
Heffernan, Jane	York University
Hennessy, Matt	University of Ontario Institute of Technology
Huang, Huaxiong	York University
Jessop, Raluca	University of Waterloo
Johnson, Angella	University of Southern California
Johnston, Miles	Sunnybrook Health Sciences Centre
Kloostermann, Matt	University of Ontario Institute of Technology
Kohandel, Mohammad	University of Waterloo
Komarova, Svetlana	McGill University
Langford, William	University of Guelph
Lewis, Gregory	University of Ontario Institute of Technology
López, Monserratt	McGill University
Lynch, Michael	MITACS Inc.

Name	Affiliation
Madras, Neal	York University
Miasnikof, Peter	University of Toronto
Miura, Robert M.	New Jersey Institute of Technology
Morfin Ramrez, Mario	University of Toronto
Naire, Shailesh	Keele University
Nigam, Nilima	McGill University
Orser, Brenda	B.I.O. Letha Information Systems, Inc.
Pan, Adam	University of Toronto
Phillips, Joel	McGill University
Pourziaei, Bobby	York University
Pugh, Mary C.	University of Toronto
Qazi, Sanjive	Gustavus Adolphus College
Rababah, Abedallah	Jordan University of Science and Technology
Ramirez Ramirez, Lilia	University of Waterloo
Raymond, Christopher	University of Delaware
Rezvani, Nargol	University of Toronto
Sanchez, Antonio	University of Waterloo
Sanchez-Bravo, Ivete	Center for the Mathematical Research (CIMAT)
Schwendeman, Donald	Rensselaer Polytechnic Institute
Sherk, Trevor	UOIT
Siggers, Jennifer	Imperial College London
Sivaloganathan, Sivabal	University of Waterloo
Takeva-Velkova, Viliyana	University of Ontario Institute of Technology
Tan, Yongji	Fudan University
Tilley, Burt S.	Franklin W. Olin College of Engineering
Tindall, Marcus	University of Reading
Vrscay, Edward R.	University of Waterloo
Waikar, Sushrut	Brigham and Women's Hospital, Harvard Medical School
Wall, David	University of Canterbury
Wattis, Jonathan	University of Nottingham
Whiteley, Jonathan	University of Oxford
Whittaker, Robert J.	University of Oxford Mathematical Institute
Wilkie, Kathleen	University of Waterloo
Williams, JF	Simon Fraser University
Wright, Thomas	Hospital for Sick Children
Yao, Wei	York University